

Ionic Liquid (IL) Functionalized Biochar in Supercapacitor Applications and Unique Characterization Methods.

by © Sara Cheema

A thesis submitted to the School of Graduate Studies in partial fulfillment of the
requirements for the degree of

Master of Science

Department of Chemistry
Memorial University of Newfoundland

September 2023

St. John's, Newfoundland and Labrador, Canada

Abstract

Biochar is a carbon-based material derived from biomass with unique physical and functional properties that are useful in various applications such as electrical storage devices, adsorbents, and catalysis. Biochar is used in electrochemical devices due to its porosity, surface area, and functionality including N, P, or S heteroatoms covalently bound on the surface. Biochar as an electrode material improves power density and charge-discharge rates in supercapacitors. We have shown that a simple oxidation step on hardwood biochar allows for facile functionalization using a modified Hummer method; then functionalized with 3-chloropropyltrimethylsiloxane and converted trioctylphosphonium salt biochar using S_N2 chemistry with trioctylphosphine. These functionalized biochars are characterized using FT-IR; ^1H , $^{13}\text{C}\{^1\text{H}\}$, $^{19}\text{F}\{^1\text{H}\}$, $^{31}\text{P}\{^1\text{H}\}$ CPMAS solid-state NMR spectroscopy, surface contact measurements and electrochemical characterization, CV and GCD.

McKenna et al. of the National High Magnetic Field Laboratory (NHMFL) and Florida State University reported the complex mixtures of highly heterogeneous biochar using APPI-21T-FT-ICR and ESI-21T-FT-ICR MS to yield remarkable speciation of the compounds in biochar using solvent extrography. In this thesis, an investigation into the identification of polycyclic aromatic hydrocarbons (PAHs) in kelp, crab, and hardwood biochar will be reported using the specialized solvent method to yield a necessary processing step before the application of biochar to remove select PAHs.

General summary

A supercapacitor is an energy storage device with high energy and power density containing materials for electrodes, that are commonly made up of carbon-based electrodes in devices. Biochar can be an alternative material as an electrode in supercapacitor applications when modified. The use of biochar in various applications helps reduce environmental impact by mitigating climate change and can add to the circular economy of materials. This work summarizes a modification method to make a phosphonium salt modified-ionic liquid (IL)-biochar to check its suitability for supercapacitors. This work also reports experiments on biochar from three different sources, hardwood, crab shell and sugar kelp to identify condensed polycyclic aromatic hydrocarbon between the range of C13-C34 by using Atmospheric Pressure Photoionization (APPI)-21 Tesla-Fourier Transform-Ion Cyclotron Resonance (FT-ICR).

Acknowledgements

I would like to thank my primary supervisor, Dr. Stephanie MacQuarrie, for absolutely everything! Seriously the list is endless, and I could write another thesis just on how you have positively impacted my career, but here is a shorter ‘spark notes’/‘Wikipedia page’ version. To start, thank you for always making time to help me, guide me, check in on me and encourage me. You have shown me how to be a professional and what a happy and healthy supervisor-student relationship is! This includes watching out for me, giving me the best advice that was not limited to science, and treating me like your own. I feel that I can come to you with anything, and that is truly the best feeling to share with someone. You are a phenomenal educator, and learning from you these past two years has been so enjoyable and easy. You have taught me more than I even expected to learn, but the most impactful things are work-life balance and what I can achieve in such a short period of time! You truly inspire me as a chemist, a future mother and a future educator (if I’m lucky enough to be one), and I’m so fortunate to have a role model and mentor in you!

Another role model and mentor that has also largely influenced my career is Dr. Francesca Kerton, my co-supervisor, in absolutely everything you do, you add positivity and lightness to it. You inspire everyone around you with your knowledge, passion for science, kindness, and empathy. Speaking with you is always fun, refreshing, and exactly what I always needed to push forward, you have uplifted me, guided me and encouraged me more than you know. I’m so thankful to know you, be supervised by you, and have a

person like you to turn to. You have given me so many opportunities, and my gratitude toward you has no end!!

The next person I'd really like to acknowledge is Chris Kozak, he has shown me how fun science can be, how to inspire students to love science and most importantly, how to safely blow shit up. Your encouragement to put off coffee with chemists gave me another wonderful thing to work hard at, and it showed me how fun it is to educate the public on various topics. You have mentored me and supported me, thank you for all of the chats and the goss - it made work way more fun! Also, a big thank you to Dr. T. Jane Stockmann and her group members for making me find another passion in electrochemical characterization and making electrochemistry so easy to learn. I'd also like to thank the MacQuarrie Research Group for the shared enthusiasm from a distance, and the Green Chemistry & Catalysis group for the comradery. I'd also like to thank Dr. Amy McKenna for hosting me at Florida State University for the week I was there and for the help interpreting the complex data sets.

To each of my cheerleaders, including my wonderful parents, brothers, friends, extended family and previous supervisors - thank you so much for celebrating me and showing me how proud you are of me. That is truly what drives me day-to-day, and without that, I wouldn't be where I am today.

Table of Contents

Abstract.....	ii
General summary.....	iii
Acknowledgements	iv
List of figures.....	ix
List of schemes.....	xiii
List of tables.....	xiv
List of abbreviations and symbols.....	xvi
CHAPTER 1: Introduction	1
1.1 Green Chemistry	1
1.2 Biochar	2
1.3 Waste valorization for the production of biochar	3
1.3.1 Hardwood biochar	4
1.3.2 Crab biochar	6
1.3.3 Sugar kelp biochar	7
1.4 Post-pyrolysis modification on biochars.....	8
1.5 Characterization methods.....	10
1.6 Biochar in electrochemical applications	12
1.7 Specialized characterization by 21 tesla Fourier transform ion cyclotron resonance mass spectrometry.....	14
1.8 Objectives	16
CHAPTER 2: New characterization approach for simple identification of modified biochar using solid-state NMR spectroscopy	19
2.1 Introduction.....	20
2.1.2 Increasing the degree of functionalization by exfoliation	24
2.2 Results and discussion	26
2.2.1 Preparation and characterization of hydroxylated biochar	26
2.2.2 Preparation and characterization of CPTMS-biochar	27
2.2.3 Preparation and characterization of TOPPTMS Cl⁻	32
2.2.4 Preparation and characterization of phosphonium modified-biochar	34
2.2.5 Hydrophobicity of modified biochar	39
2.2.6 Alternative direct synthetic route to phosphonium-modified biochar	41

2.2.7 Phosphorus quantification using $^{31}\text{P}\{^1\text{H}\}$ CPMAS NMR spectroscopy on exfoliated and non-exfoliated $(\text{C}_8\text{H}_{17})_3\text{P}^+\text{Cl}^-$ biochar	42
2.3 Conclusion	44
2.4 Experimental	44
2.4.1 General materials	44
2.4.2 Characterization	44
2.4.3 Methods	46
2.4.4 Synthesis of hydroxylated biochar	46
2.4.5 Exfoliation of hydroxylated biochar	48
2.4.6 Synthesis of CPTMS biochar	48
2.4.7 Synthesis of 3-(trioctylphosphonium chloride)propyltrimethoxysilane (TOPPTMS Cl)	49
2.4.7 Synthesis of $(\text{C}_8\text{H}_{17})_3\text{P}^+\text{Cl}^-$ biochar	50
CHAPTER 3: Phosphonium-IL-modified biochar: electrochemical screening for suitability in supercapacitors	52
3.1 Introduction	53
3.1.1 Biochar in supercapacitors	53
3.1.2 Ionic liquids in supercapacitors	54
3.1.3 Electrochemical characterization	55
3.1.4 Synthesis of phosphonium salt-IL-modified biochar	56
3.2 Results and Discussion	60
3.2.1 Preparation and characterization of $(\text{C}_8\text{H}_{17})_3\text{P}^+\text{NTf}_2^-$ biochar	60
3.2.2 Surface morphology study of functionalized biochar	63
3.2.3 Electrochemical study of functionalized biochar, pristine biochar and activated carbon with ionic liquid surface coating	68
3.3 Conclusion	75
3.4 Experimental	75
3.4.1 General materials	75
3.4.2 Methods	76
3.4.3 Synthesis of $(\text{C}_8\text{H}_{17})_3\text{P}^+\text{Cl}^-$ biochar	76
3.4.4 Synthesis of $(\text{C}_8\text{H}_{17})_3\text{P}^+\text{NTf}_2^-$ biochar	76
3.4.5 Characterization	77
3.4.6 Experimental set-up	79

CHAPTER 4: Molecular speciation of hardwood, crab shell and sugar kelp biochar: solvent extrography using APPI-21T-FT-ICR mass spectrometry.....	82
4.1 Introduction.....	84
4.2 Discussion.....	88
4.2.1 Positive mode APPI identification of aromatic species by solvent extrography.....	88
4.2.2 DBE versus carbon number plots for the identification of core structures of hardwood, crab and sugar kelp biochar	91
4.3 Conclusion	100
4.4 Experimental.....	101
4.4.1 Materials	101
4.4.2 Characterization	102
4.4.3 Methods	102
CHAPTER 5: Conclusion and future work.....	104
5.1 Ideas for future work	104
5.2 Conclusions	108
References	110
Appendix I: Additional optimized reactions.....	120
Synthesis of TMS-biochar	120
Appendix II: Reaction optimization studies	123
SI 1. All biochar characterization: ¹ H NMR, ¹³ C NMR, IR, and ³¹ P data.	131
SI 2. Surface contact angle measurement	138
SI 3. Quantification of Phosphorus on biochar.....	139
SI 4. Capacitance and potential window calculations.....	140
SI 5. Data summaries of solvent extracts from hardwood biochar.	141
SI 6. Data summaries of solvent extracts from crab biochar.	148
SI 7. Data summaries of solvent extracts from kelp biochar.	155

List of figures

Figure 1.1 The 12 Principles of Green Chemistry.	1
Figure 1.2 Composition of monomers of the polysaccharides and biopolymers of hardwood biochar.....	5
Figure 1.3 The main components of crab shell before pyrolysis.	6
Figure 1.4 Oxidation of biochar using HNO ₃ and H ₂ SO ₄ . ^{31, 32}	9
Figure 1.5 Siloxane condensation of biochar using APTES.....	9
Figure 1.6 Surface contact angle measurement on hydrophobic biochar reported by Zhang et al. ³⁷	11
Figure 1.7 All experimental parameters for the experimental setup for both cells were investigated in this work.	17
Figure 2.1 Melamine-biochar reported by Mosaffa et al. ⁵⁰	20
Figure 2.2 A longer synthetic route to chloride functionalized group biochar.	22
Figure 2.3 Synthesis of PA-biochar.	23
Figure 2.4 FT-IR spectra of pristine hardwood biochar (pink, top) and hydroxylated biochar (purple, bottom).	26
Figure 2.5 FT-IR spectra of CPTMS-biochar optimization.	29
Figure 2.6 FT-IR spectra of biochar (pink, top), hydroxylated biochar (purple, middle 1), and 9 eq exfoliated CPTMS-biochar (blue, middle 2) and 9 eq of non-exfoliated CPTMS-biochar (green, bottom).....	30
Figure 2.7 ¹³ C{ ¹ H} CPMAS NMR spectra of biochar (top) and CPTMS-biochar (bottom).....	31
Figure 2.8 Stacked FT-IR spectra of CPTMS (blue, row 1), TOPPTMS Cl ⁻ (green, row 2) and TOP (yellow, row 3).	33
Figure 2.9 ³¹ P NMR spectra of TOPPTMS Cl ⁻ in CDCl ₃ (top) and indirect non-exfoliated (C ₈ H ₁₇) ₃ P ⁺ Cl ⁻ biochar ³¹ P{ ¹ H} CPMAS NMR spectra (bottom). Referenced to ammonium dihydrogenphosphate (ADP).	36
Figure 2.10 ¹³ C solution NMR spectrum of TOPPTMS Cl ⁻ in CDCl ₃ (top) and (C ₈ H ₁₇) ₃ P ⁺ Cl ⁻ biochar ¹³ C{ ¹ H} CPMAS NMR spectrum (bottom).	37
Figure 2.11 ¹ H NMR spectra of TOPPTMS Cl ⁻ in CDCl ₃ (top) and (C ₈ H ₁₇) ₃ P ⁺ Cl ⁻ biochar ¹ H solid-state NMR spectra (bottom).	37
Figure 2.12 Stacked FT-IR spectra of pristine biochar (pink, row 1), hydroxylated biochar (purple, row 2), CPTMS-biochar (blue, row 3), and (C ₈ H ₁₇) ₃ P ⁺ Cl ⁻ biochar (orange, row 4).....	39
Figure 2.13 Identification of hydrophobicity of (C ₈ H ₁₇) ₃ P ⁺ Cl ⁻ biochar.....	40

Figure 2.14 The FT-IR spectra of exfoliated $(C_8H_{17})_3P^+Cl^-$ biochar using direct synthesis (orange, top) and indirect synthesis (yellow, bottom) routes.....	41
Figure 2.15 $^{31}P\{^1H\}$ CPMAS NMR spectra of indirect synthesis on non-exfoliated $(C_8H_{17})_3P^+Cl^-$ biochar (top), indirect synthesis on exfoliated $(C_8H_{17})_3P^+Cl^-$ biochar (middle), and direct synthesis on exfoliated $(C_8H_{17})_3P^+Cl^-$ biochar (bottom).	43
Figure 3.1 Synthesis of phosphonium-IL-modified biochars under investigation. (3 and 4)	57
Figure 3.2 Surface coating preparation method and electrochemical cell using Teflon cup using Ag/AgCl reference electrode, Pt(s) counter electrode and functionalized biochar surface modified working electrode.....	58
Figure 3.3 FT-IR spectra stacked of pristine biochar (pink, row 1), hydroxylated biochar (purple, row 2), CPTMS-biochar (blue, row 3), $(C_8H_{17})_3P^+ Cl^-$ biochar (orange, row 4), and $(C_8H_{17})_3P^+ NTf_2^-$ biochar (green, row 5).....	61
Figure 3.4 $^{31}P\{^1H\}$ CPMAS NMR spectra of $(C_8H_{17})_3P^+Cl^-$ biochar (top) and $(C_8H_{17})_3P^+ NTf_2^-$ biochar (bottom).....	62
Figure 3.5 $^{19}F\{^1H\}$ CPMAS NMR spectra of $(C_8H_{17})_3P^+ NTf_2^-$ biochar.	62
Figure 3.6 SEM images of $(C_8H_{17})_3P^+Cl^-$ biochar showing rod-like formations. Scale bars: (a) 10 μm and (b) 1 μm . The Orange arrow is showing rough spherical surface of biochar.....	63
Figure 3.7 TEM images of $(C_8H_{17})_3P^+Cl^-$ biochar (left, A and C) and $(C_8H_{17})_3P^+NTf_2^-$ biochar (right, B and D). Scale bars: 500 nm (top) and 200 nm (bottom).....	65
Figure 3.8 TEM images of $(C_8H_{17})_3P^+ Cl^-$ biochar (left, A) and $(C_8H_{17})_3P^+ NTf_2^-$ biochar (middle, B) and activated carbon (right, C). Scale bars: 200 nm.....	66
Figure 3.9 pXRD diffractograms of activated carbon, pristine biochar and phosphonium salt-IL-modified biochar. Diffractograms off-set on the y-axis for clarity.....	67
Figure 3.10 A and B Cell I: Cyclic voltammograms of electrode A (green, top) and B (red, bottom) with a 50 mV/s scan rate. (first column). i. and ii. The GCD of electrodes A (green, top) and B (red, bottom) using an applied current of 150 μA and 0.6 μA , respectively. (second column) The electrolyte systems used for electrodes A and B are 100 mM Na_2SO_4 and 10 mM $LiNTf_2$ solutions, respectively.....	70
Figure 3.11 A Cell II: Cyclic voltammogram of electrode C prepared on carbon paper with a scan rate of 50 mV/s. (green, left) iii. The GCD measurements of electrodes C and D using an applied current of -132 μA and -4 μA , respectively. (right) The electrolyte systems used for electrodes C and D are 100 mM Na_2SO_4 and 10 mM $LiNTf_2$ solutions, respectively.	71
Figure 3.12 Cell I: E, F Cyclic voltammograms with a scan rate of 50 mV/s (left) and GCD measurements (iv) using an applied current of 150 μA (right) in 1.0 M $NaCl$ (iv) of E (pink) and F (purple) modified electrodes.	72

Figure 3.13 Cell I: F, G Cyclic voltammogram with a scan rate of 50 mV/s and GCD measurements (v) of electrode F and G electrodes under the applied current of 150 μ A for each electrode and with an electrolyte system is 1.0 M NaCl. Vi. is the voltammogram of electrode G and A with a scan rate of 50 mV/s in 100 mM Na ₂ SO ₄	74
Figure 4.1 Solvent extrography method by fractionation.	87
Figure 4.2 Heteroatom class distribution of bc _{hw} for each solvent extraction fraction from the whole extract, acetone, Hep/Tol, Tol/THF/MeOH. This plot and bc _{hw} data were obtained from NHMFL at FSU.	89
Figure 4.3 Heteroatom class distribution of bc _{cs} for each solvent extraction fraction from the whole extract, acetone, Hep/Tol, Tol/THF/MeOH. This plot and bc _{cs} data were obtained from NHMFL at FSU.	90
Figure 4.4 Heteroatom class distribution of bc _{sk} for each solvent extraction fraction from the whole extract, acetone, Hep/Tol, Tol/THF/MeOH. This plot and bc _{sk} data were obtained from NHMFL at FSU.	90
Figure 4.5 Isoabundant maps of DBE as a function of carbon number for HC class species of the whole extract, acetone, Hep/ Tol, Tol/THF/MeOH solvent fractions of bc _{hw} extractions. Plots and data provided by NHMFL at FSU.	92
Figure 4.6 Isoabundant maps of DBE as a function of carbon number for HC class species of the whole extract, acetone, Hep/ Tol, Tol/ THF/ MeOH solvent fractions of bc _{cs} extractions. Plots and data provided by NHMFL at FSU.	94
Figure 4.7 Isoabundant maps of DBE as a function of carbon number for HC class species of the whole extract, acetone, Hep/Tol, Tol/THF/MeOH solvent fractions of bc _{sk} extractions. Plots and data provided by NHMFL at FSU.	95
Figure 4.8 Isoabundant maps of DBE as a function of carbon number for O ₁ class species of the whole extract, acetone, Hep/Tol, Tol/THF/MeOH solvent fractions of each biochar species. Plots and data provided by NHMFL at FSU.	97
Figure 4.9 Isoabundant maps of DBE as a function of carbon number for N ₁ class species of the whole extract, acetone, Hep/ Tol, Tol/ THF/ MeOH solvent fractions of each biochar species. Plots and data provided by NHMFL at FSU.	99
Figure 5.1 The cyclic voltammogram of pristine biochar with P _{6,6,6,10} Br (IL) on a GCE in 100 mM Na ₂ SO ₄	106
Figure 5.2 Future device-making operation for phosphonium chloride-IL-modified biochar.....	107
Figure AI.1 Stacked FT-IR spectra of TMS biochar and hydroxylated biochar.	121
Figure AI.2 ¹³ C{ ¹ H} CPMAS NMR spectrum of TMS biochar.	122
Figure AII.1 Stacked FT-IR spectra of biochar, hydroxylated biochar, and 3 eq CPTMS functionalized biochars.	123

Figure AII.2 Stacked FT-IR spectra of biochar, hydroxylated biochar, and 7 eq CPTMS functionalized biochars	124
Figure AII.3 ^1H NMR spectrum of the CPTMS reaction filtrate in CDCl_3	126
Figure AII.4 Stacked FT-IR spectra of 48 h phosphonium modification reaction on non-exfoliated biochar.....	127
Figure AII.5 Stacked FT-IR spectra of 3, 6 and 9 eq of TOP (w/w) applied to CPTMS-biochar to synthesize $(\text{C}_8\text{H}_{17})_3\text{P}^+\text{Cl}^-$ biochar over 96 h.....	128
Figure AII.6 ^1H NMR spectrum of TOP by-product from filtrate quantification in CDCl_3	130
Figure SI 1.1 FT-IR spectra of hydroxylated biochar.....	131
Figure SI 1.2 FT-IR spectra of CPTMS-biochar.	132
Figure SI 1.3 ^1H NMR spectrum of TOPPTMS Cl^- in CDCl_3	133
Figure SI 1.4 ^{31}P decoupled NMR spectrum of TOPPTMS Cl^- in CDCl_3	134
Figure SI 1.5 FT-IR spectra of $(\text{C}_8\text{H}_{17})_3\text{P}^+ \text{Cl}^-$ biochar.	135
Figure SI 1.6 $^{13}\text{C}\{^1\text{H}\}$ CPMAS NMR spectrum of $(\text{C}_8\text{H}_{17})_3\text{P}^+\text{Cl}^-$ biochar.	136
Figure SI 1.7 $^{31}\text{P}\{^1\text{H}\}$ CPMAS NMR spectrum of non-exfoliated indirect synthesis of $(\text{C}_8\text{H}_{17})_3\text{P}^+\text{Cl}^-$ biochar using ADP as the internal standard.	137
Figure SI 2.1 Surface contact angle experimental setup.....	138
Figure SI 2.2 The contact surface angle measurements of exfoliated indirect synthesis of $(\text{C}_8\text{H}_{17})_3\text{P}^+ \text{Cl}^-$ biochar.	138

List of schemes

Scheme 2.1 Reaction scheme of hydroxylated biochar.....	26
Scheme 2.2 Reaction scheme of CPTMS-biochar.	28
Scheme 2.3 Reaction scheme of TOPPTMS Cl ⁻	32
Scheme 2.4 Reaction scheme of the indirect synthesis of (C ₈ H ₁₇) ₃ P ⁺ Cl ⁻ biochar.	34
Scheme AI.1 Reaction scheme for TMS biochar.	121

List of tables

Table 2.1 Surface contact angle measurements.	40
Table 2.2. The comparison of the synthesis conditions and % phosphorous added to the surface of biochar for phosphorus quantification—sample calculations are provided in Appendix 2.....	42
Table 3.1 Electrode composition summary.....	59
Table 3.2 BET measurements of exfoliated and non-exfoliated phosphonium chloride biochar.....	64
Table AII.1 The data summary of the 3, 7 and 9 eq of CPTMS optimization reactions for CPTMS Biochar.....	125
Table AII.2 The data summary of the 3, 6 and 9 eq of TOP optimization reactions for (C ₈ H ₁₇) ₃ P ⁺ Cl ⁻ biochar.....	129
Table SI 1.1 Characterization summary of FT-IR spectroscopy assignments.	132
Table SI 1.3 Comparison of functional group characterization by FT-IR spectroscopy of (C ₈ H ₁₇) ₃ P ⁺ Cl ⁻ biochar.	135
Table SI. 4.1 Electrochemical data summary	140
Table SI 5.1 The data summary of the whole fraction is based on the highest relative abundance of HC, O ₁ and N ₁ classes in hardwood biochar extracted by solvent extrography. Values shaded represent the protonated HC (blue), radical HC (blue), protonated O ₁ species (green) and radical O ₁ species (orange). No N ₁ species are detected.	141
Table SI 5.2 The data summary of the acetone fraction of the most abundant HC, O ₁ and N ₁ classes in hardwood biochar was extracted by solvent extrography. Values shaded represent the protonated HC (blue), radical HC (blue), protonated N ₁ species (pink), radical N ₁ species (purple), protonated O ₁ species (green), and radical O ₁ species (orange).	142
Table S I 5.3 The data summary of the heptane/toluene fraction of the most abundant HC, O ₁ and N ₁ classes in hardwood biochar extracted by solvent extrography. Values shaded represent the protonated HC (blue), radical HC (blue), protonated N ₁ species (pink), radical N ₁ species (purple), protonated O ₁ species (green), and radical O ₁ species (orange).	144
Table S I 5.4 The data summary of the Tol/THF/MeOH fractions of the most abundant HC, O ₁ and N ₁ classes in hardwood biochar extracted by solvent extrography. Values shaded represent the protonated HC (blue), radical HC (blue), protonated N ₁ species (pink), radical N ₁ species (purple), protonated O ₁ species (green), and radical O ₁ species (orange).	146
Table SI 6.1 The data summary of the whole fraction based on the highest relative abundant HC, O ₁ and N ₁ classes in crab biochar extracted by solvent extrography. Values	

shaded represent the protonated HC (blue), radical HC (blue), protonated N₁ species (pink), radical N₁ species (purple), protonated O₁ species (green), and radical O₁ species (orange). 148

Table SI 6.2 The data summary of the acetone fraction of the most abundant HC, O₁ and N₁ classes in crab biochar extracted by solvent extrography. Values shaded represent the protonated HC (blue), radical HC (blue), protonated N₁ species (pink), radical N₁ species (purple), protonated O₁ species (green), and radical O₁ species (orange). 150

Table SI 6.3 The data summary of the heptane/toluene fraction of the most abundant HC, O₁ and N₁ classes in crab biochar extracted by solvent extrography. Values shaded represent the protonated HC (blue), radical HC (blue), protonated N₁ species (pink), radical N₁ species (purple), protonated O₁ species (green), and radical O₁ species (orange). 152

Table SI 6.4 The data summary of the Tol/THF/MeOH fractions of the most abundant HC, O₁ and N₁ classes in crab biochar extracted by solvent extrography. Values shaded represent the protonated HC (blue), radical HC (blue), protonated N₁ species (pink), radical N₁ species (purple), protonated O₁ species (green), and radical O₁ species (orange). 154


Table SI 7.1 The data summary of the whole fraction based on the highest relative abundance of HC, O₁ and N₁ classes in kelp biochar extracted by solvent extrography. Values shaded represent the protonated HC (blue), radical HC (blue), protonated N₁ species (pink), radical N₁ species (purple), protonated O₁ species (green), and radical O₁ species (orange). 155

Table SI 7.2 The data summary of the acetone fraction of the most abundant HC, O₁ and N₁ classes in kelp biochar was extracted by solvent extrography. Values shaded represent the protonated HC (blue), radical HC (blue), protonated N₁ species (pink), radical N₁ species (purple), protonated O₁ species (green), and radical O₁ species (Orange). 157

Table SI 7.3 The data summary of the Hept/Tol fraction of the most abundant HC, O₁ and N₁ classes in kelp biochar was extracted by solvent extrography. Values shaded represent the protonated HC (blue), radical HC (blue), protonated N₁ species (pink), radical N₁ species (purple), protonated O₁ species (green), and radical O₁ species (orange). 159

Table SI 7.4 The data summary of the Tol/THF/MeOH fractions of the most abundant HC, O₁ and N₁ classes in kelp biochar extracted by solvent extrography. Values shaded represent the protonated HC (blue), radical HC (blue), protonated N₁ species (pink), radical N₁ species (purple), protonated O₁ species (green), and radical O₁ species (orange). 161

List of abbreviations and symbols

%:	percent
°C:	degrees celsius
°	degrees
β:	beta
–COOH:	carboxylic acid
–NO ₂ :	nitrite
	representative structure of biochar
APPI:	atmosphere pressure photoionization
APTES:	3-aminopropyltriethoxysilane
bc _{cs} :	crab shell biochar
bc _{hw} :	hardwood biochar
bc _{sk} :	sugar kelp biochar
BET:	Brunauer-Emmett-Teller
Ca:	Calcium
Cd:	Cadmium
CH ₄ :	methane
Cl:	chloride
cm ⁻¹ :	wavenumber
Co:	cobalt
CO ₂ :	carbon dioxide
CPMAS:	cross-polarization magic angle spinning
CPTMS:	3-chloropropyltrimethoxysilane
CV:	Cyclic voltammetry
DBE:	double bond equivalents
DOM:	dissolved organic matter
EA:	Elemental Analysis
EDL:	electrochemical double layer
EDX:	energy dispersive X-ray analysis

ESI:	electrospray ionization
EtOH:	ethanol
F:	Farad
FSU:	Florida State University
FT-ICR-MS:	fourier transform ion cyclotron resonance mass spectrometry
FT-IR:	fourier transform infrared spectroscopy
g:	grams
GC:	gas chromatography
GC-MS:	gas chromatography-mass spectrometry
GCD:	galvanostatic charge-discharge
H ₂ O:	water
H ₂ SO ₄ :	sulfuric acid
h:	hours
NHMFL:	National High Magnetic Field Laboratory
HNO ₃ :	nitric acid
IL:	Ionic liquid(s)
IMZC:	Imazapic
K:	Potassium
KCl:	potassium chloride
KH-570:	3-methacryloxypropyltrimethoxysilane
KOH:	potassium hydroxide
LC:	liquid chromatography
LDI:	laser desorption ionization
m/z:	mass-to-charge
mg:	milligrams
MHz:	megahertz
min:	minutes
mL:	millilitre
mmol:	millimoles
Mn:	Manganese

MS:	Mass spectrometry
mV	millivolts
N:	nitrogen
N ₂ :	molecular nitrogen
NaOH:	sodium hydroxide
NH ₃ :	ammonia
NL:	Newfoundland and Labrador
nm:	nanometer
NMR:	nuclear magnetic resonance spectroscopy
NS:	Nova Scotia
O:	Oxygen
P:	phosphorus
PAH:	polycyclic aromatic hydrocarbons
PFAS:	per- and poly fluoroalkyl substances
PTFE:	Polytetrafluoroethylene
pH:	measure of acidity
ppm:	parts per million
R.A.	relative abundance
r.t.:	room temperature
RH:	Relative humidity
s:	seconds
SEM:	Scanning electron microscopy
T:	Tesla
TEA:	triethylamine
TEM:	transmission electron microscopy
TiO ₂ :	titanium dioxide
TMS:	trimethylsilyl
TMSCl:	trimethylsilyl chloride
TOP:	trioctylphosphine
TOPO:	trioctylphosphine oxide

TOPPTMS Cl:	3-(trioctyl phosphonium chloride)propyltrimethoxysilane
TPP:	triphenylphosphine
V	volts
VOC:	volatile organic compounds
μL:	microliters

CHAPTER 1: Introduction

1.1 Green Chemistry

In the 21st century, there is a rush to alleviate the causes of climate change and global warming by implementing more environmentally aware processes. This can be achieved by following the 12 principles of green chemistry, defined by John C. Warner and Paul T. Anastas in 1998.¹ The principles are waste prevention; atom economy; less hazardous chemical synthesis; designing safer chemicals; safer solvents and auxiliaries; design for energy efficiency; use of renewable feedstock; reducing derivatives; catalysis; design for degradation; real-time pollution prevention and safer chemistry for accident prevention.¹



Figure 1.1 The 12 principles of Green Chemistry

Chemists can produce new chemicals while reducing environmental impact by assessing how each of the 12 principles in Figure 1.1 applies to their process development. This creates awareness of the environmental impact and encourages

chemists to explore more environmentally friendly alternatives. Biochar's application as functional materials can consistently follow 2 of the 12 principles of green chemistry; using renewable resources and waste prevention.

1.2 Biochar

Biochar is a carbon-based material obtained from the partial decomposition of biomass.² The production of biochar can be through pyrolysis, which is the thermal degradation of biomass in a low oxygen atmosphere,³ and the conditions of pyrolysis can yield different amounts of three products: biochar, bio-oil, and syngas.⁴ Surface properties of resulting biochar vary based on functional groups, porosity, and surface area. This depends on the temperature and residence time of pyrolysis, and the source of biomass.⁵

Biomass undergoing different types of pyrolysis can produce different biochar yields; slow or fast pyrolysis depends on slow or fast ramp rates and overall temperature maxima. Slow pyrolysis ranges between temperatures of 300–800 °C and lower ramp rates such as 1–100 °C/min.⁶ The slower ramp rate allows volatile organic compounds (VOC) to evaporate and allows the higher carbonized fraction of biochar. This allows biomass processed by slow pyrolysis to yield the highest amounts of biochar ($\geq 35\%$).⁷ Fast pyrolysis temperatures range from 300–700 °C, and ramp rates vary from 10–200 °C/s.⁸ During fast pyrolysis, the VOCs produced from the biomass are condensed to make significant amounts of bio-oil.

The benefit of pyrolysis is the flexibility to optimize the parameters to tailor the biochar to suit applications such as environmental remediation for heavy metal

treatment.⁹ This can be done by increasing or decreasing the temperature and ramp rates during pyrolysis. The higher pyrolysis temperature can result in a high surface area and pore size, increased carbonized fractions, and loss of organic moieties.⁷ Ding et al.⁹ noted that the temperature of slow pyrolysis could significantly affect the surface properties of bagasse biochar. The biochar that has been pyrolyzed at temperatures between 250–400 °C allows the retention of oxygen-containing functional groups but limits the char's pore size and surface area. Biochar produced at higher temperatures, 500 and 600 °C, have decreased functional groups on the surface, larger pore size, and surface area. Biochar pyrolyzed between 250–400 °C often contains a higher amount of oxygen-containing functional groups, which are more desirable for biochar with increased heavy metal sorption capacity.⁹

1.3 Waste valorization for the production of biochar

A renewable resource can be defined as a raw material feedstock that is regenerated or abundant to avoid depletion of the feedstock.¹⁰ Biochar is commonly obtained from the pyrolysis of waste streams from various industries, making it a renewable resource. This leads into the next principle of green chemistry: waste prevention. Waste prevention can be enforced by developing efficient processes that produce little to no waste or by finding new solutions to avoid waste from industrial operations by converting waste materials into biochar. This is also achieved by trying to make the process less energy intensive than traditional pyrolysis methods by limiting the time and temperature of pyrolysis.

The most environmentally-impactful way to produce biochar is through the valorization of industrial waste streams; this prevents greenhouse gas emissions produced through the natural decomposition of large-scale waste streams made up of biomass.¹¹ Upcycling this waste contributes to the mitigation of climate change, and biochar has been shown to positively impact the environment by its use as a soil amendment and its use in environmental remediation.^{12, 13}

Biochar produced from different sources can have other physical properties of interest, such as pH, hydrophobicity/hydrophilicity, and water retention.¹⁴ An interesting contributing factor to different physical properties in biochar is the composition of each biomass source, including different amounts of organic material and inorganic salts.

1.3.1 Hardwood biochar

Hardwood biochar is commonly obtained from waste produced by the forestry industry. One of the largest industries in Newfoundland and Labrador (NL) is paper and wood production, causing an abundance of unusable leftover biomass and a huge opportunity to produce advanced materials (otherwise known as value-added materials).¹⁵ Hardwood biochar comprises biopolymers known as hemicellulose, cellulose and lignin.¹⁶ The biopolymers comprise the following monomers in Figure 1.2: sinapyl alcohol, p-coumaryl alcohol, conifer alcohol, D-xylose, D-galactose and D-glucose.¹⁶ A biopolymer means the material is derived from biological sources (bio) and comprises many of the same repeating units (poly-). The biomass made up of these biopolymers is pyrolyzed to produce oxygen-rich biochar. Depending on the biopolymers' degradation

mechanism, the functional groups that are retained on the biochar surface could be ketones, carboxylic acids, and alcohols.⁵

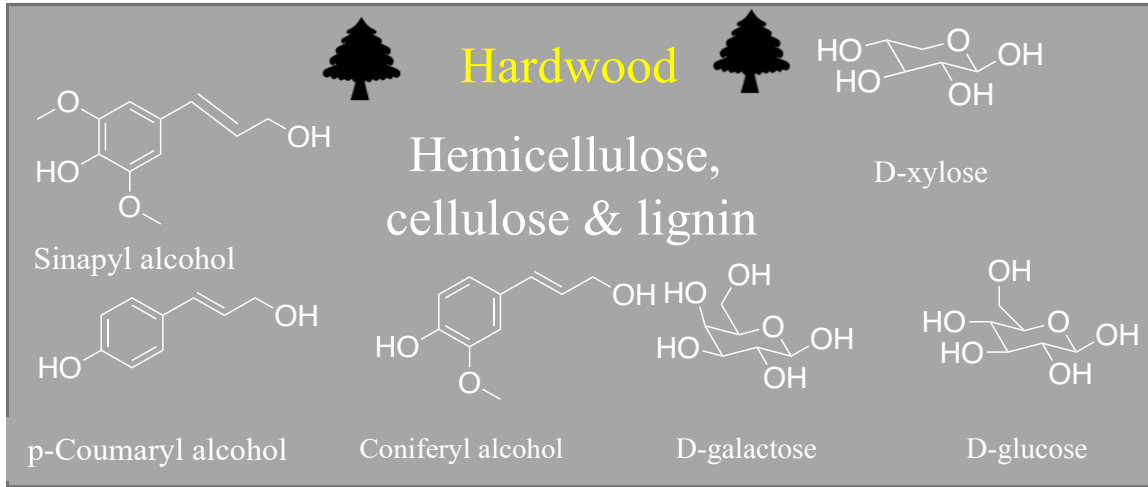


Figure 1.2 Composition of monomers of the polysaccharides and biopolymers of hardwood biochar

For centuries, hardwood biochar has been used by farmers to increase the quality of soil by adding nutrients to the soil, increasing the pH and enhancing cation exchange capacity.¹⁷ In recent years, hardwood biochar has found value as a replacement for carbon black to increase the sustainability aspect of styrene-butadiene rubber composites reported by Peterson et al.¹⁸ This group prepared birchwood biochar by pyrolysis at 550 °C for 2 h and prepared composites using 50/50 carbon black/biochar. When applied in the styrene-butadiene rubber composites expressed the same tensile strength, elongation and toughness properties as the regular carbon black rubber composite filler.¹⁸ This could have been due to the high carbon content, low ash content and particle size of the birchwood biochar studied.¹⁸

1.3.2 Crab biochar Crab biochar is obtained and processed from crab shells produced by the fishing industry and is also a waste produced by the food industry to isolate crab meat. These are some of the top sectors in NFLD and Nova Scotia (NS) and the waste being produced is significant. Burke et al noted that in Canada, the annual catch of crustaceans is 330000 Mt, with 46% of the shells being wasted.^{27, 28, 21} The major crab shell components include protein, chitin, calcium carbonate, and hydroxyapatite, denoted in figure 1.3.²² The biochar produced from crab shells tends to have oxygen-containing as well as nitrogen-containing functional groups on the surface compared to hardwood biochar.²³ This can be accredited to the pre-existing amide functionality on the surface of chitin and nitrogen within the backbone and functional groups on the protein.²⁴ This added functionality of increased N-content offers interesting applications for crab biochar.

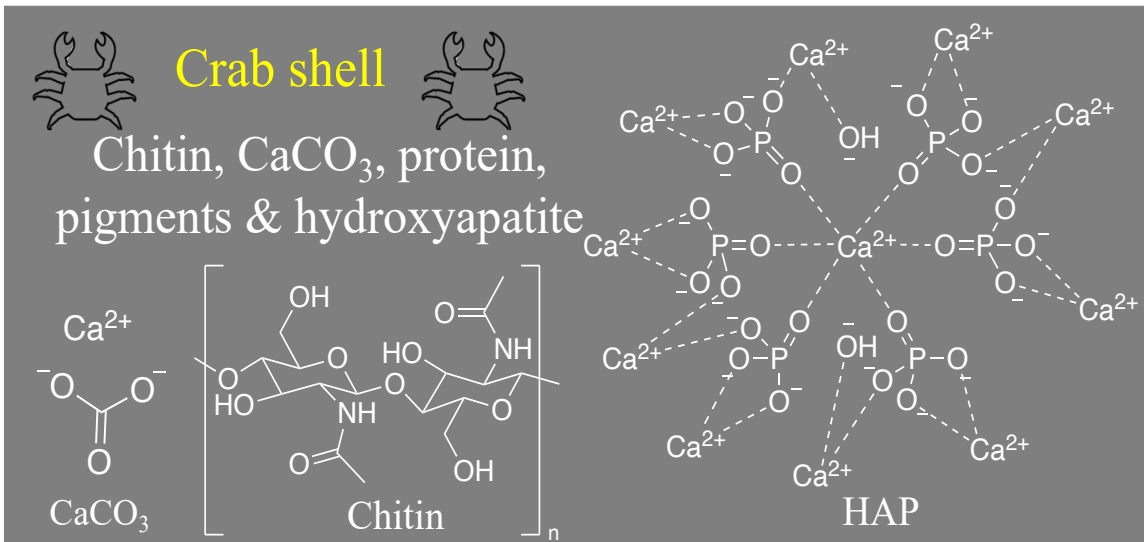


Figure 1.3 The main components of crab shell before pyrolysis

Crab biochar has been applied in environmental remediation by acting as superior adsorption towards dye removal, as reported by Dai et al.²⁵ This group prepared crab shell biochar by pyrolysis at 800 °C for 2 h to treat dye-contaminated wastewater. It was noted that the high adsorption capacity was due to the pore-filling of the biochar. They defined potential sorption mechanisms through electrostatic attraction, hydrogen-bonding, and π - π interactions.²⁵ Crab biochar is highly efficient for cationic and anionic dye adsorption, which can be achieved in just 2 min.

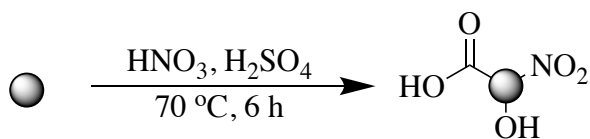
1.3.3 Sugar kelp biochar

Sugar kelp is obtained by the fishing industry or from seaweed farms, and used in the food and cosmetic industries as a thickener. Like crab biochar, kelp biochar also tends to have both oxygen- and nitrogen-containing functional groups on the surface due to the intrinsic biopolymers such as proteins, carbohydrates and polysaccharides.²⁶ Currently, kelp biochar is used for environmental remediation as a heterogeneous catalyst with oxygen-, nitrogen-, and sulphur-containing functional groups on the surface.²⁷ Wang et al. prepared kelp biochar by pyrolysis at 600 °C for 3 h under N₂. A base and acid-activated biochar is synthesized using KOH: biochar (2:1) and annealed at 600 °C for 1 h or 1.0 M H₂SO₄ at 80 °C for 1 h.²⁸ The kelp biochar was investigated for the catalytic ozonation processes for Imazapic (IMZC) degradation, an environmentally persistent organic herbicide. Sugar kelp biochar is a promising photocatalyst that achieved 97% IMZC degradation in 30 min; the enhancement is due to active sites of graphitic N- and thiophene S-added functionality.²⁸

1.4 Post-pyrolysis modification on biochars

Modification of biochar allows for varying reactivity by taking advantage of electrostatic interactions, surface complexation, Van der Waal forces, hydrophobicity and hydrogen bonding for functional materials.²⁹ Most modified biochars from the literature are generated from woody biomass and found applications in a variety of sectors. For example, as a photocatalyst, where TiO₂-doped hardwood biochar, was recently investigated by Kowalczyk et al.³⁰ Photocatalysis is an emerging field for wastewater treatment, using TiO₂-doped biochar is a sustainable way to treat water pollutants such as β -blockers.³⁰ Hardwood biochar was prepared through pyrolysis at 600 °C in an N₂ atmosphere, and hydrolysis occurred when biochar was mixed with titanium(IV) butanoate and tetraethoxysilane at 60 °C for 24 h, and yielded a TiO₂-doped biochar.³⁰ The biochar modification introduced enhanced charge storage and charge separations for photocatalysis.³⁰

Another common modification is oxidation using HNO₃-H₂SO₄ (figure 1.4). This was demonstrated using wheat straw biochar that was pyrolyzed at 450 °C by Iqbal et al.³¹ The reaction generated biochar with oxygen-rich functional groups such as -COOH and -NO₂ groups that showed interesting application for Cd Adsorption.³¹ Naderi et al. reported this same oxidation method on microalgae biochar mixed with KOH and pyrolyzed at 700 °C for 2 h. After oxidation, biochar is enhanced with iron oxides to demonstrate excellent capacity and high energy density in supercapacitors.³²



biochar

oxidized biochar

Figure 1.4 Oxidation of biochar using HNO₃ and H₂SO₄.^{31, 32}

Primary amines were introduced on the surface of oxidized softwood biochar, pyrolyzed at 500 °C, via the condensation of siloxanes by Bamdad et al. using 3-aminopropyltriethoxysilane (APTES) (figure 1.5).³³ They noted that the functionalized APTES-biochar (1) has superior adsorbent properties for CO₂.³³ Oxidized hardwood biochar was explored as a catalyst for producing cyclic carbonates using CO₂ on propylene oxides by Vidal, Kerton & MacQuarrie et al.³⁴ This hardwood biochar is prepared by aerobic digestion of birchwood and pyrolysis at 400 °C for 30 min. Hardwood biochar was oxidized using the oxidation route (1) in figure 1.5.

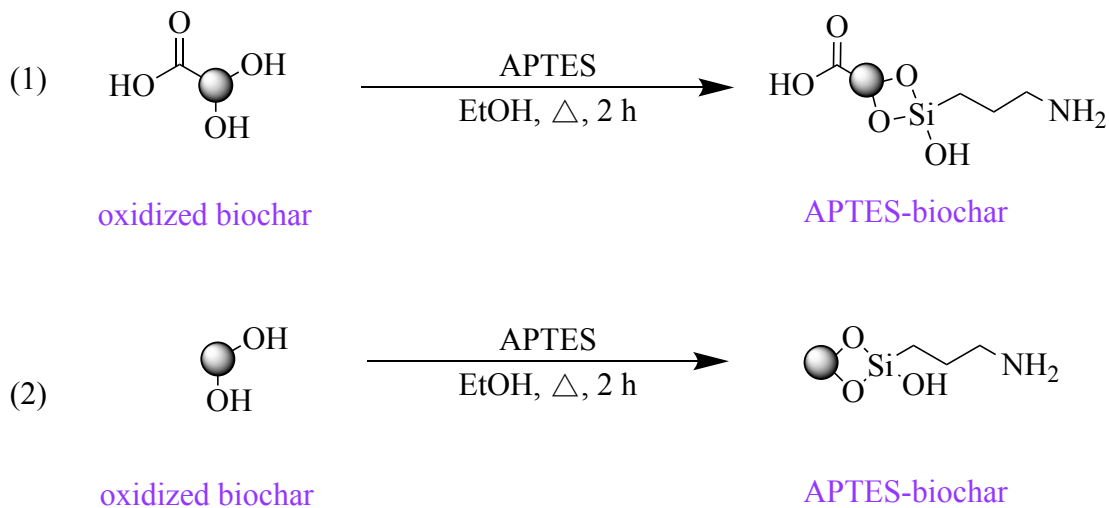


Figure 1.5 Siloxane condensation of biochar using APTES.

Hummer's oxidation method is commonly applied to biochar because of the generation of diols on the surface that occurs. Recently, MacQuarrie et al. reported using

softwood biochar pyrolyzed at 500 °C for 2 h and applied a Hummer oxidation to the biochar to install diols (2).³⁵ The added APTES group to the surface was utilized as a green alternative for heparin recovery using this different oxidation method.³⁵

1.5 Characterization methods

Biochar is challenging to characterize due to its extreme heterogeneity, large polydispersity, and insolubility. Characterization of the functional groups on the surface of biochar is not as streamlined as small molecule synthesis; it is commonly completed using Fourier transform infrared spectroscopy (FT-IR). FT-IR spectroscopy can be difficult to interpret if there are overlapping bands in regions of aromatic, aliphatic, or oxygen-containing functional groups. Thus, using various heteroatom selective solid-state nuclear magnetic resonance spectroscopy (NMR) (i.e. ^1H , ^{13}C , ^{31}P , and ^{19}F nuclei), much more descriptive characterization is possible. Solution-state NMR spectroscopy cannot be applied to characterize biochar due to its insolubility. In practice, solid-state NMR spectroscopy is usually used to characterize biochar by comparing the functional groups present in two different biomass sources of biochar. This is demonstrated by Brewer et al. using ^{13}C solid-state NMR spectroscopy to identify the functional groups of switchgrass and wood biochar.³⁶ This group investigated which biochar is more applicable to its use as a soil amendment. They compared aliphatic carbons between 0-50 ppm, ethers between 50-100 ppm, a broad peak around 125 ppm for the aromatic carbons, and –COOH groups at 176 ppm.³⁶ However, these ^{13}C peaks are so broad that small changes to the surface are not easy to note, but the successful modification of biochar can be observed and confirmed.

Identifying changes in biochar's physical properties can be as simple as testing its surface contact angle to determine its hydrophobicity. Where the surface contact angle is measured at the edge of a droplet on a flat pressed sample surface. This has been demonstrated by Zhang et al. in figure 1.6, with rice straw biochar that is pyrolyzed at 500 °C.³⁷ The biochar was suspended in EtOH and H₂O, pH was adjusted to 4, and the silane reagent, 3-methacryloxypropyltrimethoxysilane (KH-570), was added and stirred for 2 h. The successful modification to produce hydrophobic biochar was identified with a surface contact angle of 131° and 141°.³⁷

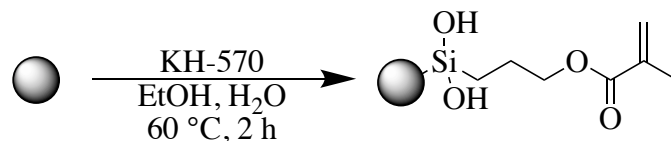


Figure 1.6 Surface contact angle measurement on hydrophobic biochar reported by Zhang et al.³⁷

Scanning electron microscopy (SEM) and transmission electron microscopy (TEM) are used to analyze biochar to determine its surface morphology and characteristics. SEM creates an image by the deflection of electrons on the surface of a material, while TEM creates an image by electrons passing through a material. Some characteristics of biochar that can be identified using these methods are pore sizes only above certain sizes and distribution; and the determination of the presence of multilayered structures.

The electrochemical properties of biochar can be identified using galvanostatic charge-discharge curves (GCD) and cyclic voltammetry (CV). GCD allows for determining capacitance for the material, and CV provides information on the electrochemical stability, redox chemistry and electrochemical window of the material.

1.6 Biochar in electrochemical applications

The application of biochar in electrochemical devices has been heavily reported in the past ten years, emphasizing its exploration in energy storage devices.³⁸ The intrinsic properties of biochar that make it suitable to be used as an electrode material include its conductivity and high thermal stability.³⁹ Supercapacitors have an electric double layer (EDL) that stores electric charge that is formed at the electrode/electrolyte interface; charge storage is influenced by surface area and pore size distribution.⁴⁰ The EDL comprises two electrodes, the cathode, and the anode, which are negatively and positively charged. The charge on the electrode governs the attraction of cations and anions from the electrolyte system to the surface of the electrode. Biochar's high surface area plays an essential role in charging the electrical double layer and determines the capacitance. The mesopores on the biochar surface can allow good electrolyte penetration, providing high power density.⁴⁰ Su et al. stated that biochar containing or functionalized with functional groups N, P, and O heteroatoms on the surface could improve the wettability and improve capacitance of the electrode material.³⁹

Reports of biochar without physical or chemical modification before, during or after pyrolysis are limited because biochar's resistive qualities cause it to be undesirable for electrochemical devices.⁴¹ Some modification methods can improve these biochar properties like electrochemical stability, conductivity, and ability to store charge. Li et al. reported N-doping of bamboo biochar chips pyrolyzed at 700 °C for 2 h under an NH₃ atmosphere.⁴² This modification is called ammonization, this occurs during pyrolysis to

produce an N-rich biochar with higher capacitance from increased material conductivity.⁴²

Ding et al.⁴³ reported an apricot shell biochar pyrolyzed at 600 °C for 2 h. It is activated with KOH to be very porous and increases its surface area, making it suitable for supercapacitor applications.⁴³ Ionic salts are commonly added to biomass pre-pyrolysis to activate biochar. Gao et al.⁴⁴ reported highly porous biochar pyrolyzed at 800 °C for 2 h, stating how higher surface area produced by slow pyrolysis improved energy storage performances. This was completed using a mixture of marine biomass to impose self-activation methods by not removing the mineral salts from the starting biomass.⁴⁴

Another way biochar can be prepared for supercapacitors is by integrating transition metal oxides throughout their porous surface. This is reported by Norouzi et al.⁴⁵ with Co-modified biochar producing increased capacitance, energy and power density from a green macroalgae source. The biochar is prepared through an activation step with NaOH, pyrolysis at 700 °C for 2 h, and oxidization using HNO₃ and H₂SO₄. Co(NO₃)₂•6H₂O is suspended with the oxidized biochar and heated at 150 °C for 15 h.⁴⁵ The cobalt hydroxides are desirable to be integrated into the biochar due to their low cost, reversibility, high conductivity, multiple oxidation states and high specific capacitance.⁴⁵ However, the incorporation of metals onto the surface of biochar diminishes the sustainability aspect of biochar for supercapacitor applications.

1.7 Specialized characterization by 21 tesla Fourier transform ion cyclotron resonance mass spectrometry

Characterizing biochar is very difficult due to the polydispersity and polyfunctionality in composition that challenges all other mass spectral interpretations due to the ultrahigh resolving power requirement inherent in biochar. Mass spectrometry studies molecular compounds by measuring the mass-to-charge (m/z) ratio of tens of thousands of compounds in a sample that can be used as qualitative and quantitative data. An ion source typically ionizes analytes, that are mass selected prior to being detected by a mass analyzer for interpretation.

All mass spectrometers (MS) can consists of an inlet, ion source, mass analyzer(s), and detector. The inlet is where the sample is inserted into the MS, which can be direct or indirect. Direct injection is where a sample is placed directly into the instrument, while indirect injection is where the instrument uses another separation technique before each component enters the MS, such as liquid chromatography (LC) or gas chromatography (GC). In LC, the molecules are separated based on affinity to other molecules in the sample and stationary phase (column), while a mobile phase elutes separated compounds based on polarizability. Biochar cannot be separated using LC due to its insolubility. In GC samples are heated and converted to a vapor and passed through a chromatography column to separate them into their components so that the mass spectrometer can analyze them. Biochar is difficult to analyze using GC-MS due to its non-volatility. Therefore, solvent extrography can be applied to separate dissolved organic matter (DOM) and select ionization methods can be used to identify different components.

FT-ICR is a mass analyzer and detector that provides ultra-high resolution, ultra-high mass accuracy, and a very efficient ion-trapping form of mass spectrometry.⁴⁶ For this instrument, mass analysis and detection occur in the same place; the ions are contained in the trap by using strong magnetic and electric fields. When the ion is placed in a uniform magnetic field, it oscillates at the same frequency characteristic to its m/z . An excitation pulse induces this; the frequency produced from the ions depends on the size of the ions and the vibrational frequencies produced to create a spectrum. This method has been predominantly used to analyze bio-oil produced from pyrolysis; the investigations for biochar characterization utilizing this type of mass spectroscopy have been an exciting and emerging field.

An advance in characterizing biochar with mass spectrometry was explored by Aubriet et al. using laser desorption ionization (LDI) on wood surfaces.⁴⁷ The laser (266 and 355 nm) mimicked pyrolysis to help identify woody biochar components. This was achieved through mass analysis by 9.4 Tesla (T)-FT-ICR, and this group reported that hydrocarbon ions were produced using a 355 nm laser.⁴⁷ This can demonstrate the unwanted reactions during ionization leading to more thermal decomposition occurring when biochar is analyzed by this method.

Lee et al.⁴⁸ characterized peanut shell, chicken litter and pine wood biochar pyrolyzed at 411, 424, and 450 °C, respectively, using ESI-12 T-FT-ICR. Each biochar was water extracted and separated using electrodialysis, the three fractions produced included anode isolated, center chamber retained, and cathode isolated substances.⁴⁸ The substances isolated were identified to inhibit aquatic photosynthetic microorganisms' growth when released into the environment.⁴⁸

Most recently, Kentucky bluegrass biochar pyrolyzed at 500 °C for 2 h and analyzed by 21T FT-ICR McKenna et al.⁴⁹ This was the first ever reported biochar extraction using ESI-FT-ICR and APPI-FT-ICR using a solvent extrography method using acetone/cyclohexanone and toluene/tetrahydrofuran/methanol.⁴⁹ These solvents allowed selectivity of different polarity, ionizability, and stability through intermolecular interactions. McKenna first coupled 21-tesla FT-ICR MS to biochar with the first direct identification of biochar species with the same composition as coal and heavy oil asphaltene corresponding to condensed peri-fused PAHs.⁴⁹

1.8 Objectives

The objectives of this thesis are to modify and characterize biochar for application in a supercapacitor and to analyze data from FT-ICR MS experiments to evaluate its potential for characterizing biochar. The FT-ICR MS experiments use different biomass types and the potential of having different functional groups incorporated.

In Chapter 2, the novel phosphonium-IL-modified hardwood biochar is reported. The quantification of phosphonium-added groups to exfoliated and non-exfoliated biochar is completed using ³¹P cross-polarization magic angle spinning (CPMAS) NMR spectroscopy. Here, the phosphonium-modified biochar is confirmed using ¹H, ³¹P{¹H} and ¹³C{¹H} CPMAS NMR spectroscopy; and FT-IR spectroscopy methods. The indirect and direct modification methods were attempted on hydroxylated biochar: (1) siloxane condensations using 3-chloropropyltrimethoxysilane (CPTMS); and the S_N2 reaction to form (C₈H₁₇)₃P⁺ Cl⁻ biochar and (2) the siloxane condensation using 3-(trioctyl phosphonium chloride) trimethoxysilane (TOPPTMS Cl). To highlight a significant

change in the physical properties, the phosphonium-modified biochar was characterized by surface contact angle to demonstrate hydrophobicity.

In Chapter 3, unmodified and modified-IL-hardwood biochars were investigated and compared to activated carbon to assess the potential for use in supercapacitors. Figure 1.7 highlights the experimental parameters varied for cell setups, including surface coating mixtures of IL inks made up of activated carbon, phosphonium-IL-modified biochar and pristine biochar characterized using CV and GCD.

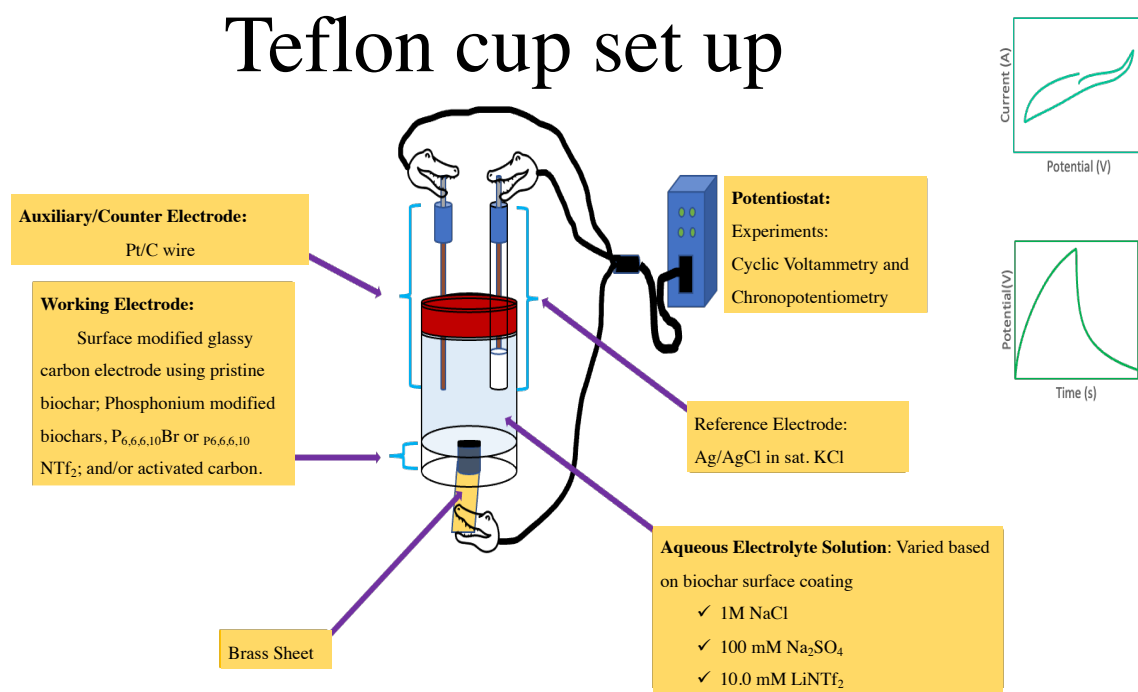


Figure 1.7 All experimental parameters for the experimental setup for both cells were investigated in this work.

The phosphonium-IL-modified biochar prepared in Chapter 2 also underwent a salt metathesis from Cl^- to $^-NTf_2$. The synthesis and characterization using $^{31}P\{^1H\}$ and $^{19}F\{^1H\}$ CPMAS NMR spectroscopy and the significantly different electrochemical

results are discussed. The surface-modified electrodes are prepared using a glassy carbon electrode and carbon paper in a Teflon cup cell and H-cell.

In Chapter 4, the molecular speciation of condensed PAHs for sugar kelp, crab shell and hardwood biochar is reported—the first application of solvent extrography on marine-sourced biochar. Comparing the hydrocarbon fraction obtained from each solvent fraction and source using APPI–21 T–FT–ICR is reported.

Co-Authorship Statement:

CHAPTER 2: New characterization approach for simple identification of modified biochar using solid-state NMR spectroscopy

Sara M. K. Cheema, Celine M. Schneider, Francesca M. Kerton, and Stephanie L. MacQuarrie.

Article in preparation to be submitted to *Chemical Communications*.

The first author (Sara M. K. Cheema) contributed 85% of the content of this article as the primary researcher, including performing experiments, collecting data reported and writing the manuscript.

The co-author (Celine M. Schneider) obtained the solid-state NMR data for each modified biochar.

The co-author (Francesca M. Kerton), my co-supervisor, was responsible for the original concept, suggested characterization experiments, and revised and submitted the manuscript.

The corresponding author (Stephanie L. MacQuarrie), my primary supervisor, was the principal investigator of this work and was responsible for the original concept, suggesting experiments, assisting with data interpretation and revising the manuscript.

CHAPTER 2: New characterization approach for simple identification of modified biochar using solid-state NMR spectroscopy

2.1 Introduction

Biochar is a heterogeneous carbon-rich organic material that is obtained through the pyrolysis of biomass. By applying modifications on the surface of biochar, it can produce modified biochar with superior properties. This has been demonstrated with the sulfonated biochar's enhanced use in catalysis due to increased acidity and hydrophobicity.⁵⁰ Some routes to modified biochar rely on siloxane condensation reactions to achieve functionalization. One example of this reported by Mosaffa et al. is presented in **Figure 2.1**. This group demonstrated the reaction of oxidized biochar with 3-chloropropyltrimethoxysilane (CPTMS) to install a primary chloride functional group and applied S_N2 chemistry to install the amine-rich melamine functionalized biochar.⁵¹

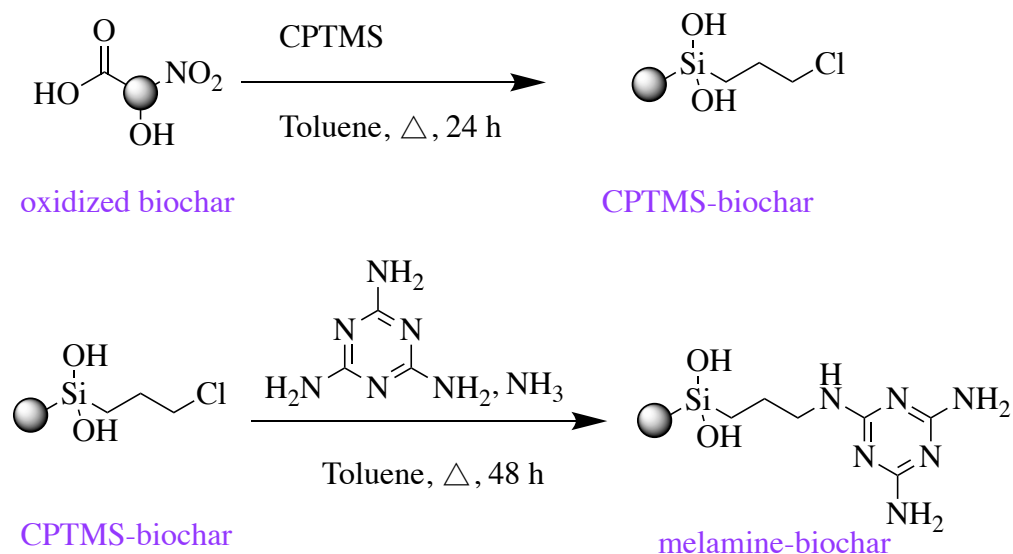


Figure 2.1 Melamine-biochar reported by Mosaffa et al.⁵¹

The functional groups of melamine-modified biochar were characterized with Fourier Transform Infrared (FT-IR) spectroscopy. This group reported that additional Si--O and Si-C stretching bands were observed at 1155 and 1086 cm^{-1} , respectively. They also identified the stretching vibrations for C-Cl bonds responsible for peaks in the 850–695 cm^{-1} range.⁵¹ Biochar functional groups are known to be very difficult to characterize, and limited characterization methods can be used to prove the successful modification of biochar. Therefore, Mosaffa et al. confirmed this functionalization by identifying the mass degradation of the amine-rich melamine biochar between 520–700 °C from thermal gravimetric analysis (TGA).⁵¹ TGA identifies the mass loss of organic moieties by the decomposition of material; thus, this range corresponds to the deamination process and decomposition of the remaining material.⁵¹ The challenge with conventional TGA is that alone it cannot identify the components based on the degradation of the material. However, it is a simple method to prove that functional groups are added to the material's surface by the change in mass lost.

Another way to characterize biochar surface morphology is scanning electron microscopy (SEM) images. Images obtained from SEM analysis for biochar are commonly used to describe the appearance of the surface of unmodified or modified biochar material. An example of this is dye absorption; SEM observes this as the a porous surface of Melamine-biochar showed the pores filled post-adsorption. The melamine biochar adsorbed dyes due to the enhanced hydrogen bonding, electrostatic, and π - π interactions through functionalization.⁵¹

The limitations of characterization by FT-IR spectroscopy, TGA and SEM are discussed by Zhou et al. reporting an iminodiacetic acid-biochar using a 4-step synthesis. The synthesis in Figure 2.2 involved a siloxane condensation by reacting oxidized biochar with 3-aminopropyltriethoxysilane (APTES). Next, the new primary amine was reacted with epichlorohydrin to introduce primary alkyl chloride functionality.⁵² Then, the S_N2 reaction generates functional iminodiacetic acid-biochar by displacing the primary chloride. Each synthetic step was characterized by FT-IR spectroscopy, however, the interpretation is difficult due to the pre-existing $-\text{COOH}$ functionality on the material. The one diagnostic band that verified successful functionalization was Si-O stretching vibration at 1098 cm^{-1} .⁵² TGA was again used to confirm functionalization, however, Zhou et al. just noted that the functionalized iminodiacetic acid-biochar had higher thermal stability.⁵²

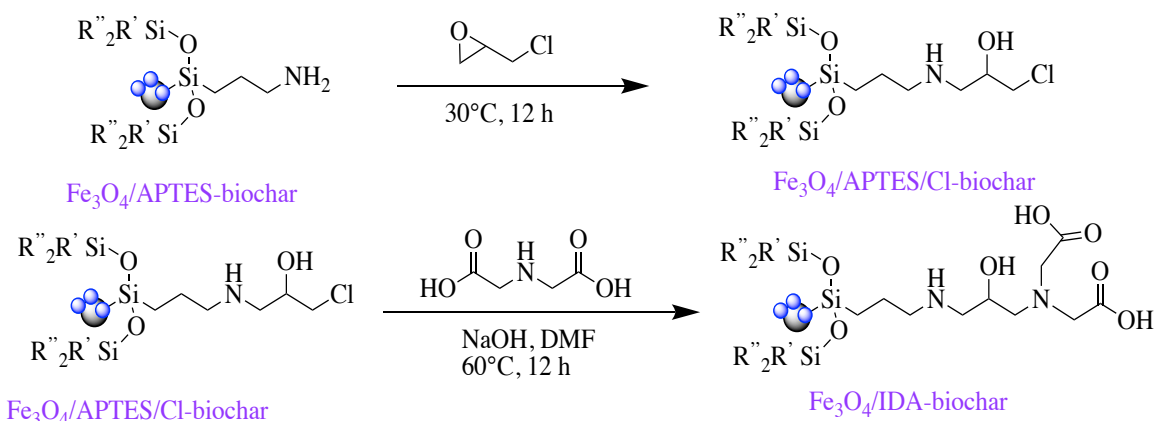


Figure 2.2 A longer synthetic route to chloride functionalized group biochar.

Zhou et al. also noted that SEM imaging could be reliable in proving the modification of biochar by showing the change in surface roughness due to oxidation of the surface.⁵² However, the biochar surface showed no difference after condensation

reactions, especially when converting the Cl-biochar into iminodiacetic acid-biochar.⁵² This contradicts the successful functionalization reaction results.

Many examples of unmodified and modified biochar are characterized using FT-IR spectroscopy, however, many researchers face challenges identifying new peaks from functionalization due to overlapping broad bands from the biochar surface. This was again demonstrated by another group. Tian et al.⁵³ modified the surface of pristine biochar with phytic acid (PA). It was difficult to characterize the added P–O groups using FT-IR spectroscopy due to vibration bands at 1080 cm^{-1} at the same wavenumber of C–O bond stretches.⁵³

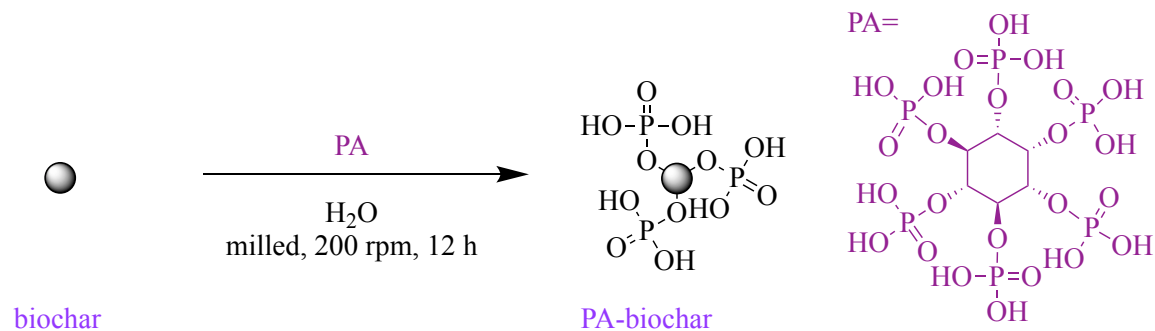


Figure 2.3 Synthesis of PA-biochar.

These unreliable results limit the characterization of PA-biochar in (**Figure 2.3.**) Tian et al. tried to compensate with the confirmation of $-\text{PO}_4$ functional groups using X-ray photoelectron spectroscopy (XPS).⁵³ XPS is a type of electron spectroscopy where X-ray photons are irradiated on the surface of a sample, and an electron beam is produced that is analyzed. This method provides information on the elements present on the surface of a material and what other elements it is bounded to.⁵⁴ PA-biochar was analyzed by XPS, Tian et al. identified the P 2p are represented by two peaks at 133.1 and 134.6 eV could prove the P functional group that is pentavalently coordinated to biochar.⁵³

However, this method is challenging to interpret, and instruments are costly, so many chemists do not have access to them.

More recently, Xie et al. reported phosphorus-modified biochar when reacting biochar with phosphoric acid. This group could still not confirm by FT-IR spectroscopy phosphorus-added functional groups biochar and relied on XPS with a peak at 134.20 eV to prove the incorporation of P atoms in the carbon network. Xie et al.⁵⁵ also reported the total phosphorus content of phosphoric acid–modified biochar with an inductively coupled plasma optical emission spectrometer (ICP-OES). They noted no significant difference in total P amount when varying the amount of phosphorous acid in the reaction.⁵⁵ A more straightforward, descriptive phosphorus detection method is needed to provide qualitative and quantitative data to prove phosphorous modification.

2.1.2 Increasing the degree of functionalization by exfoliation

Biochar is composed of peri-fused carbon-based materials that are known to naturally aggregate due to the π - π stacking interactions between biochar molecules, causing biochar to be a layered material. Exfoliation using sonication is when ultrasonic waves are treating a system in which it destabilizes the Van der Waals interactions between layered biochar. Sonication is widely used to exfoliate biochar to improve its dispersity in solution and, in turn, produces mono-layered biochar.⁵⁶ The monolayers produced from exfoliation should provide more accessible sites for modification and increase the surface area making it of interest to compare functionalization routes with different substituents.⁵⁶ Exfoliation has been applied on oxidized biochar using polar

solvents such as ethyl acetate (EtOAc) with stabilizing hydrogen–bond accepting interactions producing monolayers of oxidized biochar.⁵⁶

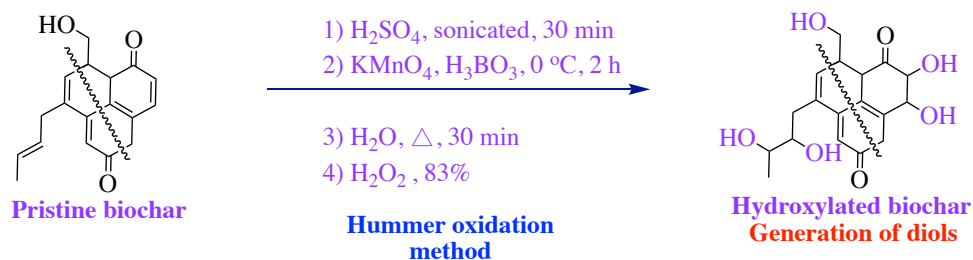
This work reports the synthesis of phosphonium chloride-modified biochar is characterized via heteroatom-specific solid-state NMR spectroscopy to quantify phosphonium modification reactions. This is completed on exfoliated and non-exfoliated hydroxylated biochar to determine the %P added to the surface. Hydroxylated biochar is an excellent candidate for liquid phase exfoliation (LPE) due to the increased polarizability introduced through functionalization that is exfoliated by sonicating with EtOAc.

The phosphonium-modified biochar is synthesized directly and indirectly using 2 grafting methods. The direct phosphonium-modification biochar is synthesized by grafting 3-(trioctylphosphonium chloride)propyltrimethoxysilane (TOPPTMS Cl⁻) to the surface of exfoliated hydroxylated biochar. The indirect phosphonium-modified biochar is completed by a condensation reaction of CPTMS with exfoliated and non-exfoliated hydroxylated biochar, then is reacted with trioctylphosphine (TOP). Phosphonium-modified biochar was characterized using ¹H, ³¹P{¹H} and ¹³C{¹H} CPMAS NMR spectroscopy, surface contact measurements and FT-IR spectroscopy. TOPPTMS Cl⁻ monomer was characterized using FT-IR spectroscopy, ¹H, ¹³C and ³¹P decoupled solution-state NMR spectroscopy.

2.2 Results and discussion

2.2.1 Preparation and characterization of hydroxylated biochar

To prepare the phosphonium-modified biochar, pristine biochar is first treated using a modified Hummer's method shown in Scheme 2.1.^{57,58} In this reaction, biochar is first dehydrated using H₂SO₄. The dehydrated biochar was treated with several oxidizing steps, including KMnO₄ and H₂O₂, to introduce diols onto the surface of the biochar and produced an 83% recovery of hydroxylated biochar.



Scheme 2.1 Reaction scheme of hydroxylated biochar.

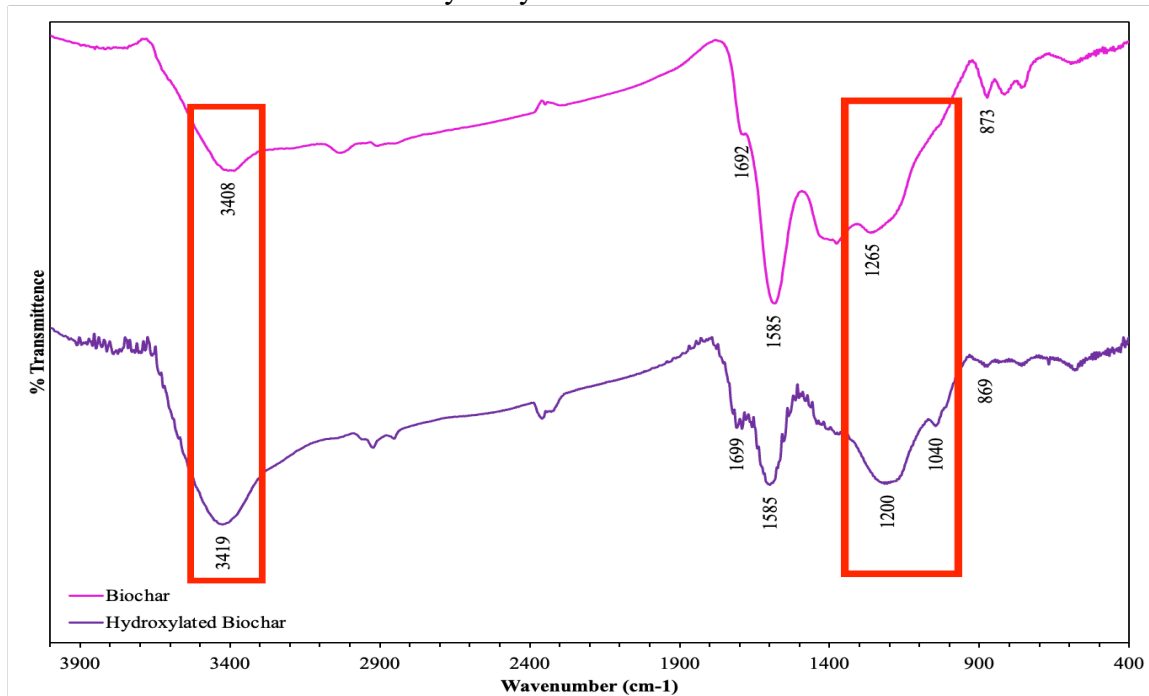


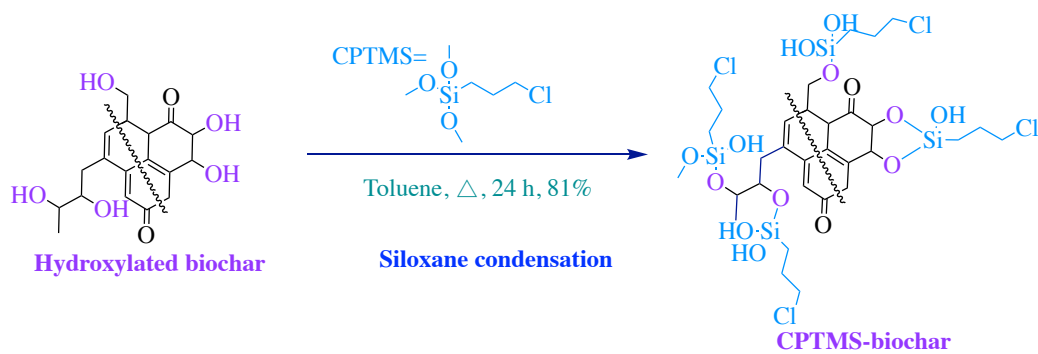
Figure 2.4 FT-IR spectra of pristine hardwood biochar (pink, top) and hydroxylated biochar (purple, bottom).

The successful hydroxylation of biochar was confirmed using FT-IR analysis (figure SI. 1). The presence of alkene stretching and bending bands at 1585 and 873 cm^{-1} , respectively, is characteristic of biochar. The other characteristic bands of biochar are the C–O stretching band at 1265 cm^{-1} and –OH stretching and bending bands around 3408 and 1692 cm^{-1} , respectively. In figure 2.4, the increased amount of –OH functional groups incorporated onto the biochar surface is confirmed by the drastic increase of the C–O stretching vibrational bands at 1200 and 1040 cm^{-1} . This also included increased –OH stretching and bending bands at 1699 and 3419 cm^{-1} , respectively, however this is not quantified.

EtOAc was chosen to exfoliate hydroxylated biochar due to its hydrogen bond acceptor stabilizing effects.⁵⁶ The –OH groups on the surface of the hydroxylated biochar are stabilized by EtOAc, producing stacked monolayers instead of highly aggregated hydroxylated biochar. This should increase the number of accessible sites for modification, improve biochar dispersity in solution and decrease overall surface area.

2.2.2 Preparation and characterization of CPTMS-biochar

Without knowing the degree of hydroxylation of the surface of biochar, the optimizations of the CPTMS condensation were attempted by differing the amounts of CPTMS reagent added to the reactions to 3 eq, 7 eq and 9 eq (w/w) (scheme 2.2).



Scheme 2.2 Reaction scheme of CPTMS-biochar.

To determine the amount of CPTMS reagent needed for the siloxane condensation onto the biochar surface, the reaction filtrate is isolated, and the solvent is removed by reduced pressure. The quantification of the dried reaction filtrate is to determine the amount of the unreacted starting material. The reaction filtrate was analyzed using ^1H NMR spectroscopy in CDCl_3 to ensure no residual solvents remained.

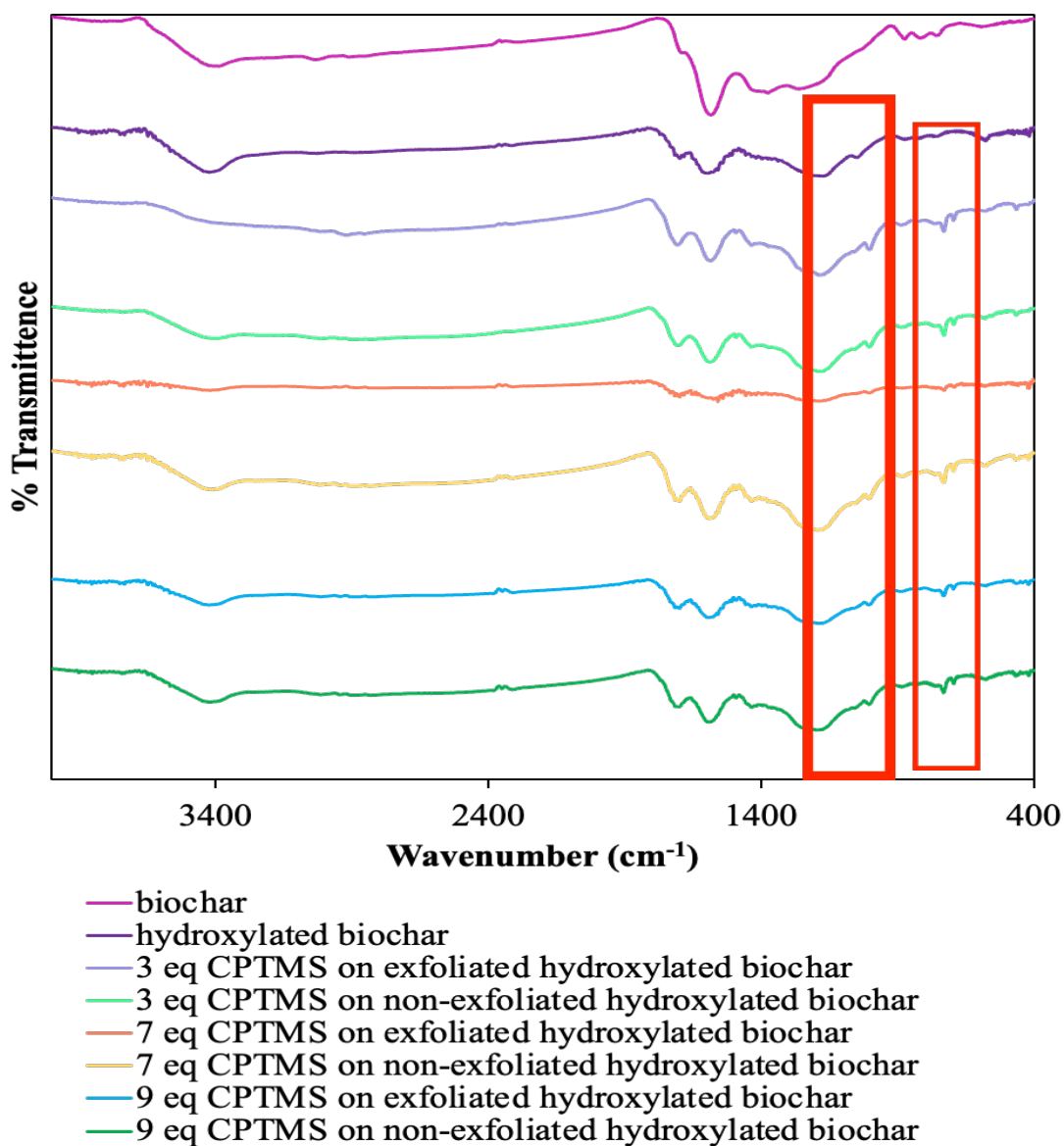


Figure 2.5 FT-IR spectra of CPTMS-biochar optimization.

There was no significant difference in exfoliated and non-exfoliated biochar with each equivalence of CPTMS. Therefore, 9 eq of CPTMS was selected so that an excess could be used in the reaction (figure 2.5). The most significant change in the FT-IR spectrum is the added peaks at 696 cm^{-1} and 733 cm^{-1} , representing the C–Cl and Si–C stretches, respectively (figure 2.6). The following siloxane bands are 1165 and 1011 cm^{-1}

to confirm the successful condensation for CPTMS-biochar. The –OH functional groups were created during the condensation reaction of the CPTMS on the biochar. The hydrolysis of methoxyl groups resulted in residual –OH stretching at 3419 cm^{-1} and produced 3-mole equivalences of methanol per hydrolysis.

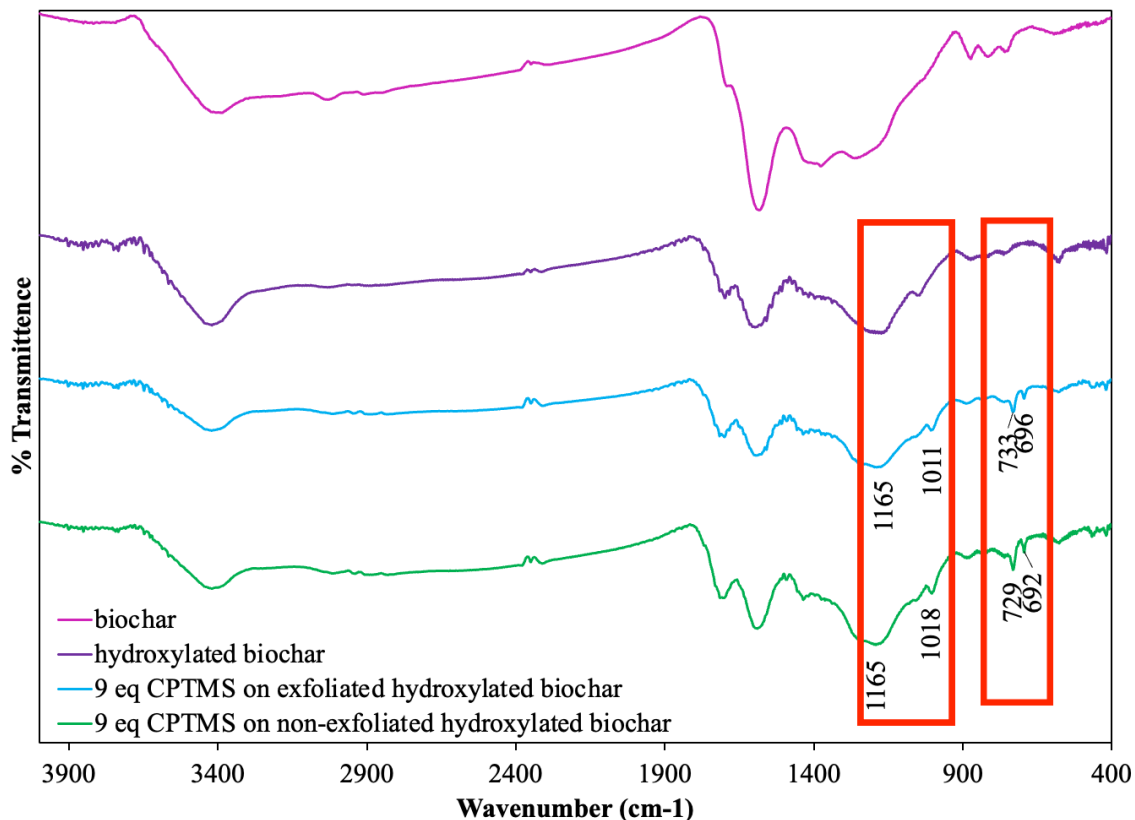


Figure 2.6 FT-IR spectra of biochar (pink, top), hydroxylated biochar (purple, middle 1), and 9 eq exfoliated CPTMS-biochar (blue, middle 2) and 9 eq of non-exfoliated CPTMS-biochar (green, bottom).

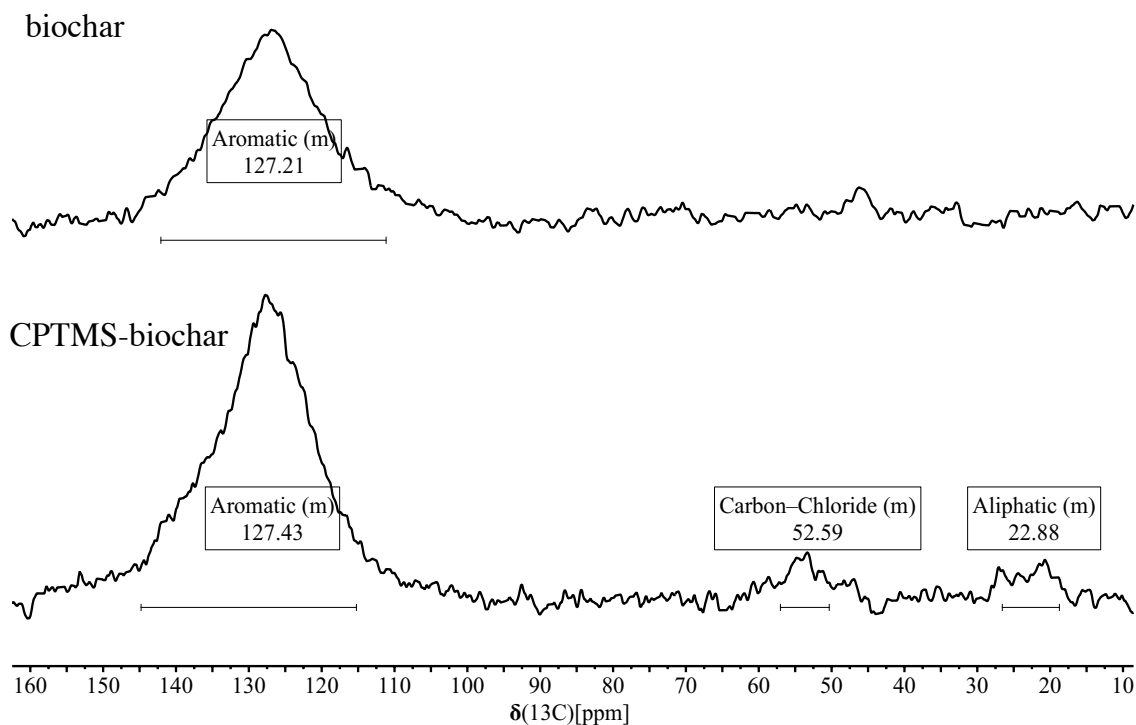


Figure 2.7 $^{13}\text{C}\{^1\text{H}\}$ CPMAS NMR spectra of biochar (top) and CPTMS-biochar (bottom).

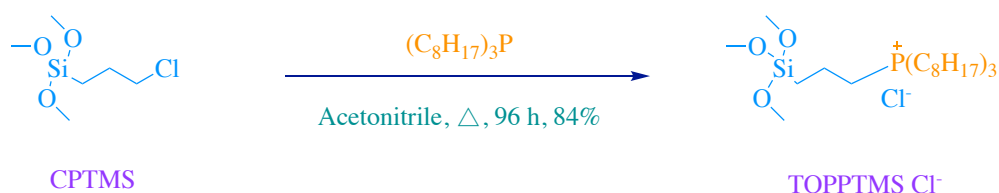
The biochar with added CPTMS functional groups was further characterized by $^{13}\text{C}\{^1\text{H}\}$ CPMAS NMR spectroscopy, with the spectrum shown in figure 2.7. The peak centred at 127 ppm represents the aromatic regions for pristine biochar (figure 2.7, top) and CPTMS-biochar (figure 2.7, bottom). The aromatic sp^2 carbons show a broad peak that ranges from 110–145 ppm, figure 2.7, Bonanomi et al. describes the ^{13}C peaks from 111-140 and 141-160 ppm of biochar to be aromatic and phenol sp^2 regions.⁵⁹ The lacking aliphatic carbon peaks at the present signal-to-noise (S/N) ratio for biochar (figure 2.7, top) is beneficial for confirming modification.

Using $^{13}\text{C}\{^1\text{H}\}$ CPMAS NMR spectroscopy to confirm modification allows for direct identification of added $-\text{CH}_2-\text{Cl}$ and $-\text{CH}_2-$ sp^3 carbons that are present at 52 and

22 ppm, respectively. These sp^3 carbon peaks were also seen by Wiench et al. when CPTMS condensed on the surface of MEM-41 and characterized using NMR spectroscopy.⁶⁰ MEM-41 is another mesoporous material, and Wiench et al. reported $--CH_2-Cl$, $-CH_2-$, and $Si-CH_2-$ peaks at 46.2, 26.7 and 9.6 ppm, which confirms successful grafting of CPTMS to the surface of their material.⁶⁰ The $Si-CH_2-$ peak at 9.6 ppm was not observed in the current example. This is likely due to the poor S/N ratio. The broadness of each peak is due to the biochar's heterogeneity and varying regions for functionalization on the surface of the biochar.

2.2.3 Preparation and characterization of TOPPTMS Cl⁻

The CPTMS reagent was converted into the TOPPTMS Cl⁻ to be grafted on hydroxylated biochar. The synthesis of TOPPTMS Cl⁻ was conducted using acetonitrile as the solvent to stabilize the polarity of TOPPTMS Cl⁻ to drive the successful functionalization using TOP.



Scheme 2.3 Reaction scheme of TOPPTMS Cl⁻.

The phosphonium modification (scheme 2.3) was successful, with a reaction yield of 84%. The modification was confirmed with FT-IR spectroscopy by bands of $--CH_2-$

and $-\text{CH}_3$ present at at 2924 and 2852 cm^{-1} ; $\text{Si}-\text{C}$ bands at 1088 cm^{-1} ; and $\text{C}-\text{O}$ bands at 1035 cm^{-1} . The $\text{P}-\text{CH}_2$ stretching band is present at 722 cm^{-1} .

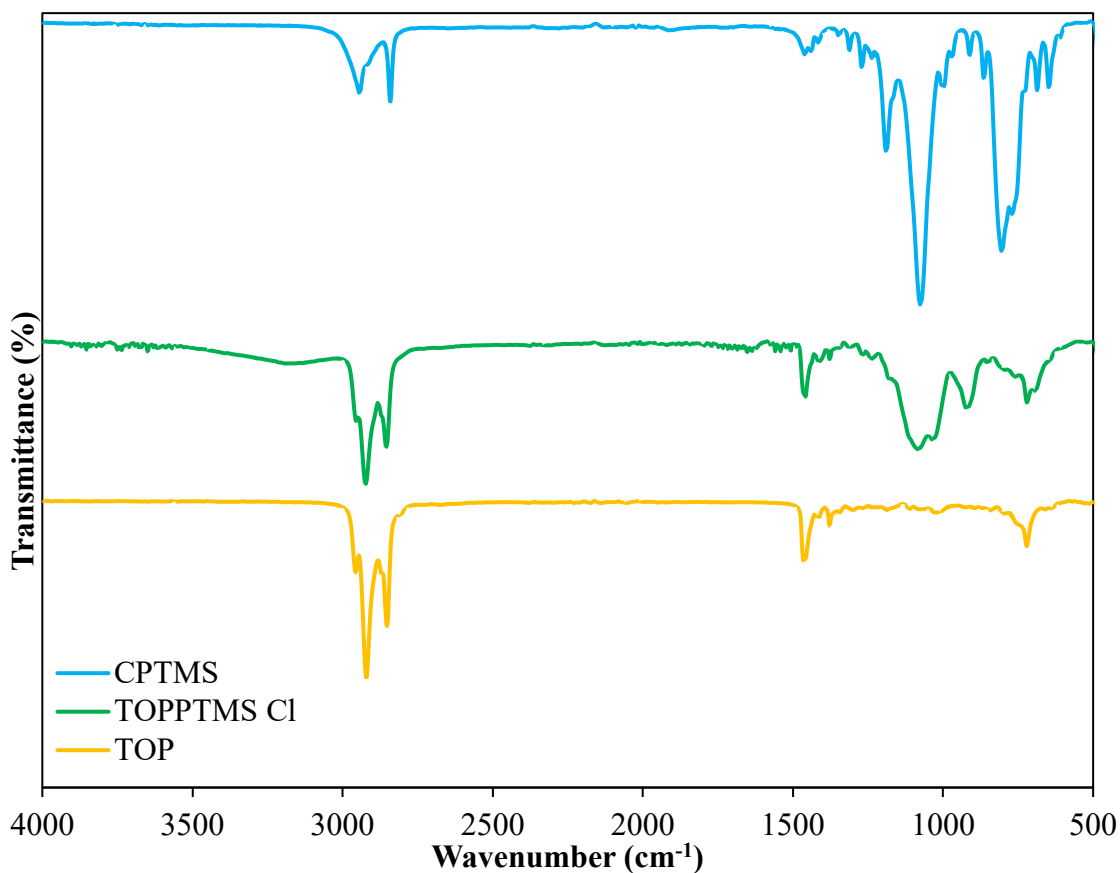


Figure 2.8 Stacked FT-IR spectra of CPTMS (blue, row 1), TOPPTMS Cl⁻ (green, row 2) and TOP (yellow, row 3).

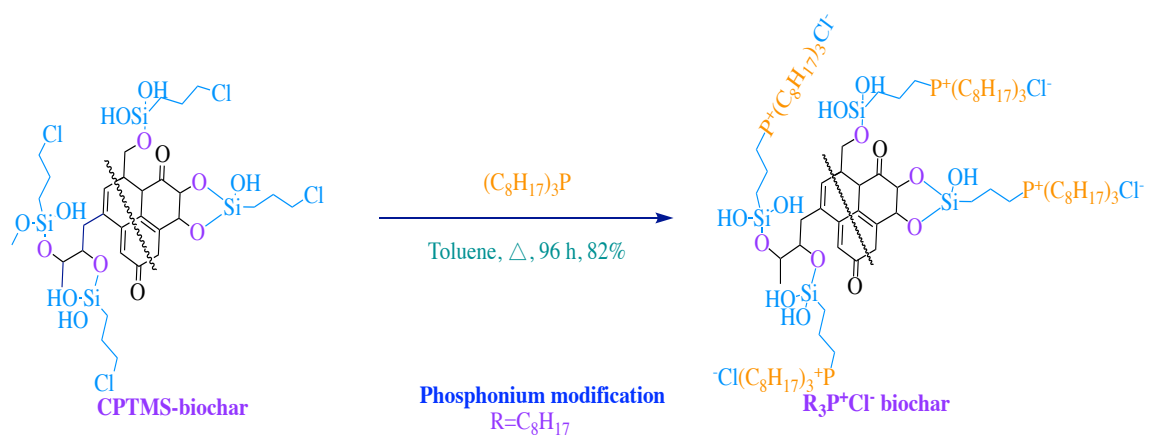
The ^1H NMR spectrum of TOPPTMS Cl⁻ in CDCl_3 (figure SI. 1.3) was performed and first, the proton signals on the propyl chain were identified as $\text{Si}-\text{CH}_2$ protons having a shift of 0.70 ppm , $-\text{CH}_2-$ at 1.90 ppm and CH_2-P at 3.56 ppm . The trioctyl groups have shifts of alkyl groups of $\text{P}-\text{CH}_2$ at 2.38 ppm , and remaining alkyl protons at $1.71-1.62$, $1.58-1.48$, 1.26 and 0.86 ppm . The broadness of the peaks is likely due to the impurities of the final product. The purification of quaternary salts is challenging due to the polarity

of the phosphonium salt products. The TOP reagent has shifts of alkyl groups: P-CH₂ at 2.38 ppm and, remaining alkyl protons at 1.71–1.62, 1.58–1.48, 1.26 and 0.86 ppm.

The ³¹P NMR spectrum of TOPPTMS Cl⁻ in CDCl₃ (figure SI. 1.4) identified a downfield phosphonium peak at 32.13 ppm. During the preparation for analysis, the sample was exposed to the air leading to the oxidation of the remaining starting material TOP into TOPO around 48 ppm.¹¹ The TOPPTMS Cl⁻ substituent was applied onto the biochar surface for the direct synthesis of phosphonium-modified biochar.

2.2.4 Preparation and characterization of phosphonium modified-biochar

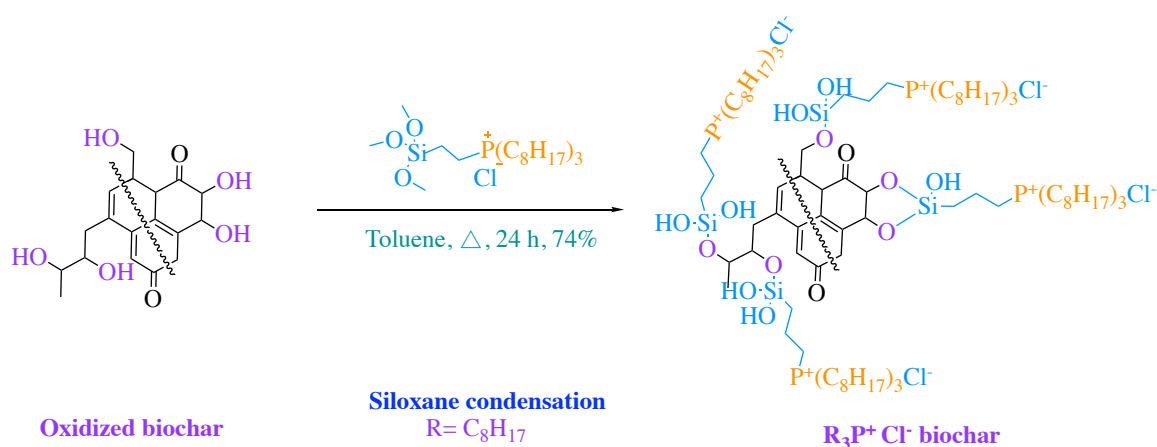
The first attempt to functionalize (C₈H₁₇)₃P⁺Cl⁻ biochar was performed using an indirect pathway on non-exfoliated CPTMS-biochar in scheme 2.4. The (C₈H₁₇)₃P⁺Cl⁻ biochar reaction conditions were optimized by applying 3, 6 and 9 eq (w/w) TOP reacted with exfoliated and non-exfoliated CPTMS-biochar. This is also directly compared to differing the reaction time from attempting a shorter 48 h to 96 h.



Scheme 2.4 Reaction scheme of the indirect synthesis of (C₈H₁₇)₃P⁺Cl⁻ biochar.

In the first set of optimization reactions using 3 eq TOP in scheme 2.4 for 48 h, no reaction occurred, and increasing to 6–9 equivalents again produced no reaction. This can

be expected as functional group conversions into salts tend to require longer reaction times; therefore, reaction run-time was doubled to ensure functionalization was achieved. The optimized reaction is a 1:3 ratio (CPTMS-biochar: TOP) to obtain $(C_8H_{17})_3P^+ Cl^-$ biochar after a 96 h reaction run-time. The second attempted procedure was by a direct synthesis that condensed the TOPPTMS Cl^- monomer to the surface of hydroxylated biochar shown in scheme 2.5 with a 74% recovery for the product $(C_8H_{17})_3P^+ Cl^-$ biochar.



Scheme 2.5 Reaction scheme of the direct synthesis of $(C_8H_{17})_3P^+ Cl^-$ biochar.

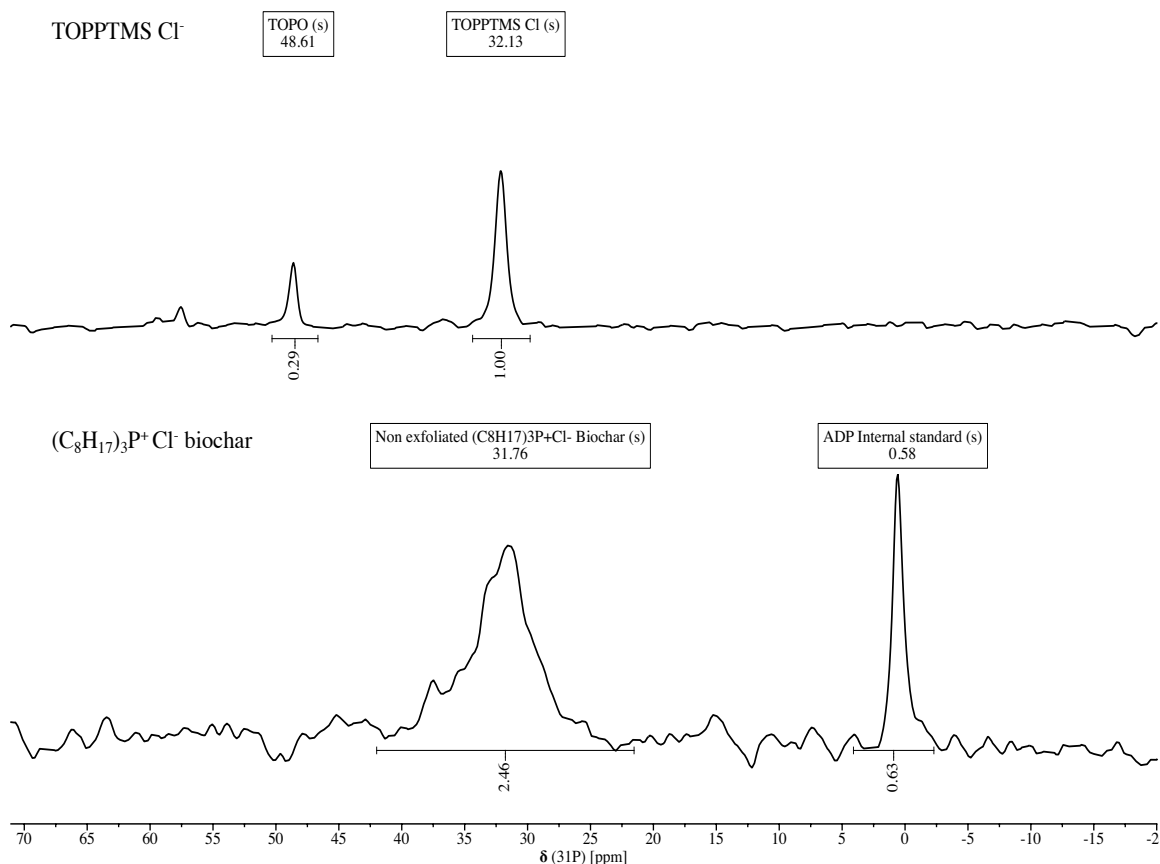


Figure 2.9 ^{31}P NMR spectra of TOPPTMS Cl^- in CDCl_3 (top) and indirect non-exfoliated $(\text{C}_8\text{H}_{17})_3\text{P}^+ \text{Cl}^-$ biochar $^{31}\text{P}\{^1\text{H}\}$ CPMAS NMR spectra (bottom). Referenced to ammonium dihydrogenphosphate (ADP).

To confirm functionalization, $(\text{C}_8\text{H}_{17})_3\text{P}^+ \text{Cl}^-$ biochar was characterized using ^1H , $^{31}\text{P}\{^1\text{H}\}$ and $^{13}\text{C}\{^1\text{H}\}$ CPMAS NMR spectroscopy and FT-IR spectroscopy. These NMR spectroscopy investigations were completed to aid in identifying the specific functional groups of the newly synthesized $(\text{C}_8\text{H}_{17})_3\text{P}^+ \text{Cl}^-$ biochar. This was conducted by comparing these signals to the NMR spectra of TOPPTMS Cl^- in CDCl_3 to identify similarities. In figure 2.9, the $^{31}\text{P}\{^1\text{H}\}$ CPMAS NMR spectrum contains a phosphonium salt peak at 31.8 ppm. This peak confirms functionalization and is a similar position ^{31}P peak 32.1 ppm compared with TOPPTMS Cl^- .

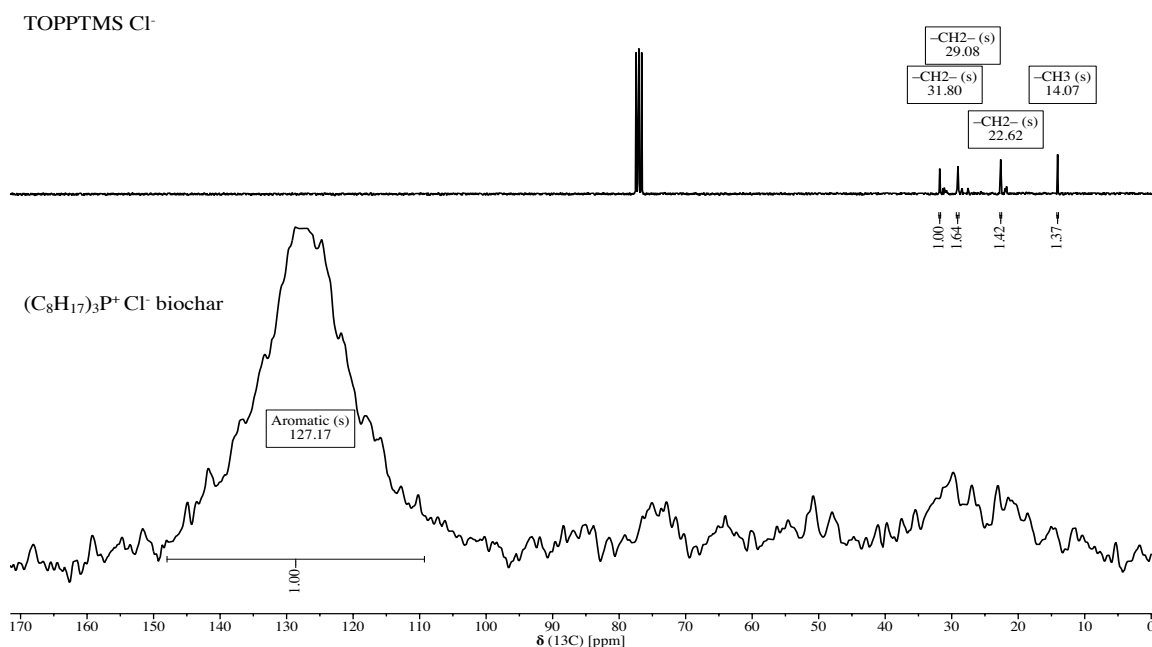


Figure 2.10 ¹³C solution NMR spectrum of TOPPTMS Cl⁻ in CDCl₃ (top) and (C₈H₁₇)₃P⁺Cl⁻ biochar ¹³C{¹H} CPMAS NMR spectrum (bottom).

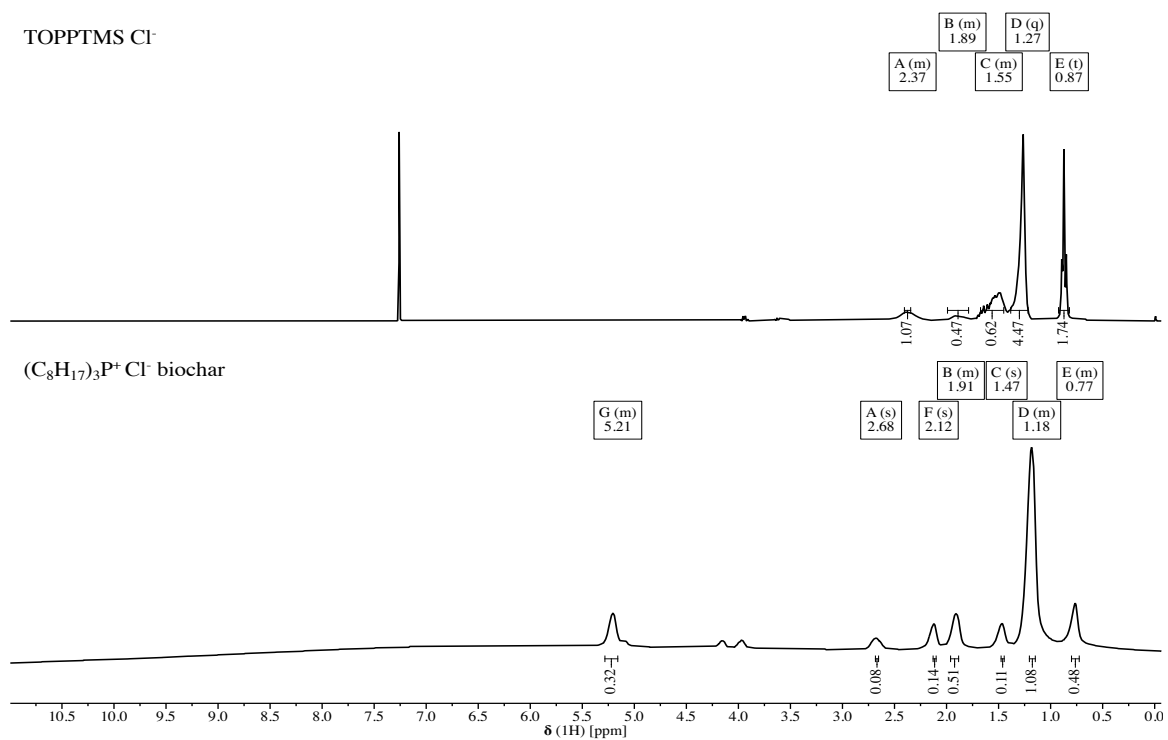


Figure 2.11 ¹H NMR spectra of TOPPTMS Cl⁻ in CDCl₃ (top) and (C₈H₁₇)₃P⁺Cl⁻ biochar ¹H solid-state NMR spectra (bottom).

In figure 2.10, the $^{13}\text{C}\{^1\text{H}\}$ CPMAS NMR spectrum confirmed the synthesis of $(\text{C}_8\text{H}_{17})_3\text{P}^+ \text{Cl}^-$ biochar with new signals attributed to the aliphatic carbons appearing between 31.8 ppm and 14.07 ppm. These peaks have a low S/N, so identifying each peak is challenging. The ^1H NMR spectrum of TOPPTMS Cl^- in CDCl_3 and $^1(\text{C}_8\text{H}_{17})_3\text{P}^+\text{Cl}^-$ biochar (shown in figure 2.11) reports the expected aliphatic proton signal positions. The signals attributed to the propyl chain, including $\text{Si}-\text{CH}_2$, $-\text{CH}_2-$ and $-\text{CH}_2-\text{P}$ appear at 0.70, 1.90, and 3.56 ppm, respectively. The 0.70 ppm signal is absent in $(\text{C}_8\text{H}_{17})_3\text{P}^+\text{Cl}^-$ biochar. The $-\text{CH}_2-$ signal at 1.90 ppm shifts to 2.12 ppm for $(\text{C}_8\text{H}_{17})_3\text{P}^+\text{Cl}^-$ biochar. The $-\text{CH}_2-\text{P}$ signal is at 3.56 ppm and also shifts to 3.97 ppm for CH_2-P for $(\text{C}_8\text{H}_{17})_3\text{P}^+\text{Cl}^-$ biochar. The shifted peaks are also distinguishable for the $-\text{CH}_2-$ in TOPPTMS Cl^- at 1.26 ppm, which is present at 1.18 ppm for $(\text{C}_8\text{H}_{17})_3\text{P}^+\text{Cl}^-$ biochar and 0.86 ppm for the methyl groups have a similar shift for $(\text{C}_8\text{H}_{17})_3\text{P}^+\text{Cl}^-$ biochar at 0.77 ppm. The alkyl chains on the TOP reagent have similar shifts, but the broadness is likely due to the heterogeneity of biochar as a material and is also typical in a solid-state NMR spectra. The $\text{P}-\text{CH}_2$ groups in the starting material are at 2.38 ppm but in $(\text{C}_8\text{H}_{17})_3\text{P}^+\text{Cl}^-$ biochar, they appear at 2.68 ppm. Other alkyl protons appear at 1.71–1.62 ppm, and 1.58–1.48 ppm in TOPPTMS Cl^- are in similar positions in the $(\text{C}_8\text{H}_{17})_3\text{P}^+\text{Cl}^-$ biochar.

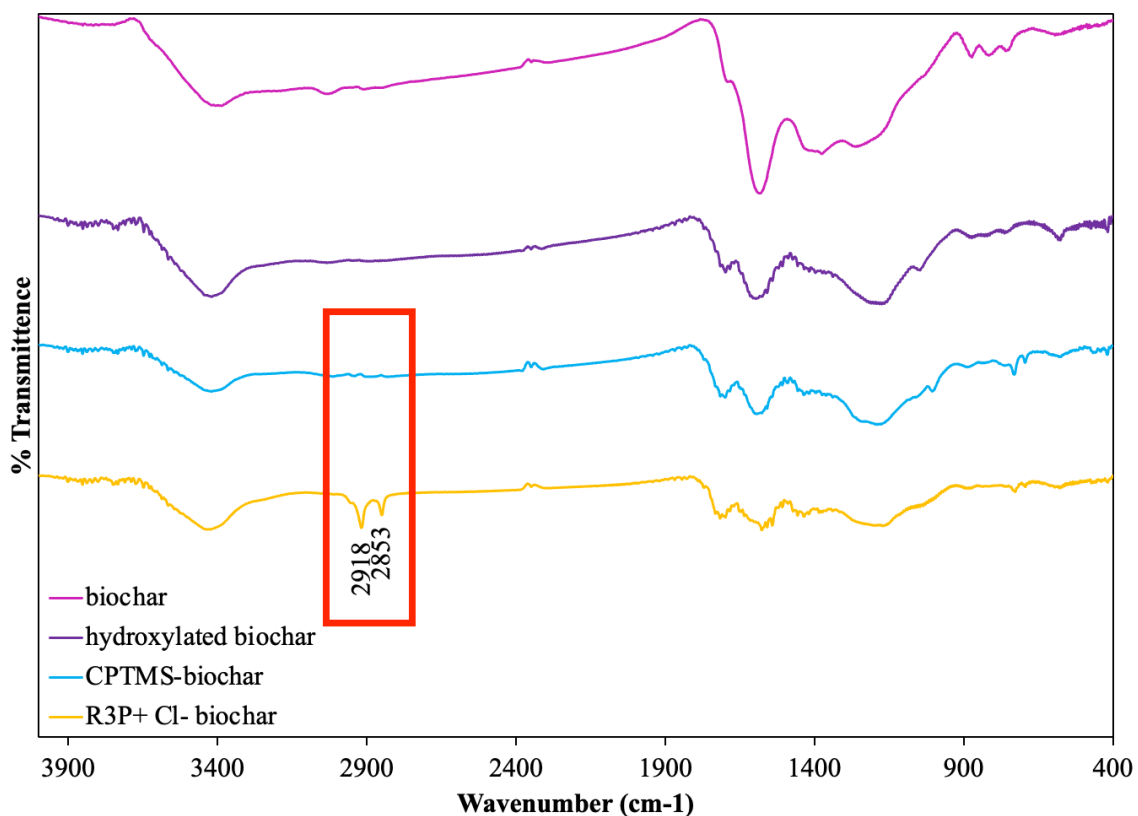


Figure 2.12 Stacked FT-IR spectra of pristine biochar (pink, row 1), hydroxylated biochar (purple, row 2), CPTMS-biochar (blue, row 3), and $(C_8H_{17})_3P^+ Cl^-$ biochar (orange, row 4).

In figure 2.12, the FT-IR spectra for each reaction step and functionalization demonstrate that reactions were successful by showing more noticeable $-CH_2$ and CH_3 bands at 2918 and 2853 cm^{-1} , respectively. Interestingly, the C-Cl band at 694 cm^{-1} was still present after quaternization regardless of the number of equivalences of TOP used in the reaction. These methyl and methylene bands could result from biochar being a heterogeneous material and could have been obscured in that region of the spectra previously by more intense $-OH$ bands. Therefore, surface contact angle measurements were conducted to further prove differences in the biochars.

2.2.5 Hydrophobicity of modified biochar

Surface contact angle measurements were performed on exfoliated $(C_8H_{17})_3P^+Cl^-$ biochar to compare with hydroxylated biochar's hydrophilic character. With the expectation that $(C_8H_{17})_3P^+Cl^-$ biochar would be a hydrophobic material due to the non-polar character of the long alkyl chains. The surface contact angle for $(C_8H_{17})_3P^+Cl^-$ biochar was determined using a homemade setup consisting of a pressed pellet of biochar, adding a 10 μ L drop to the modified biochar and measuring the angle of the water droplet on the surface depicted in figure 2.13.

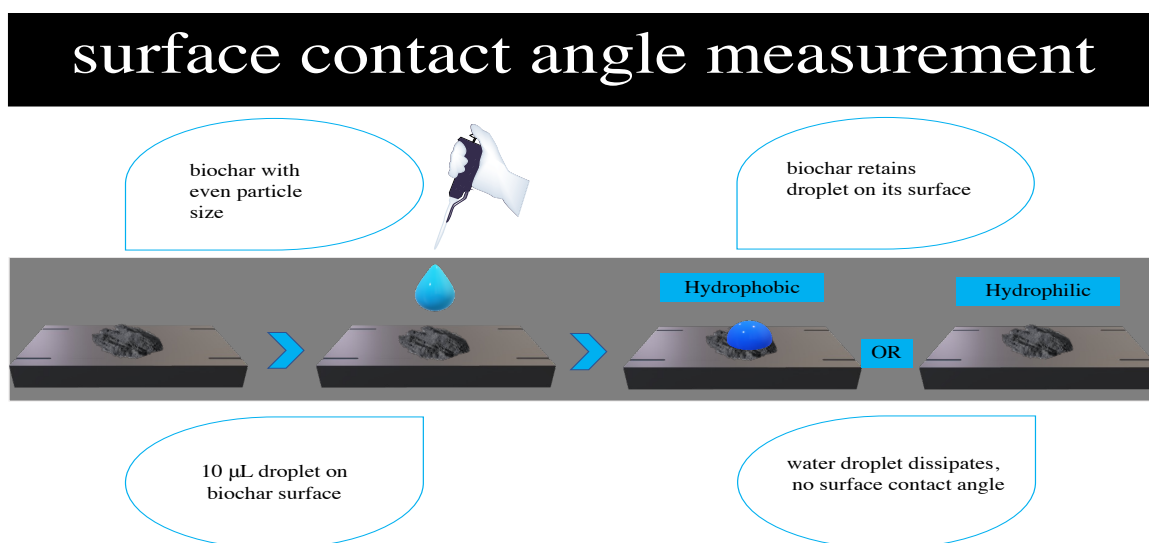


Figure 2.13 Identification of hydrophobicity of $(C_8H_{17})_3P^+Cl^-$ biochar.

Table 2.1 Surface contact angle measurements.

Biochar	θ	Relative Humidity	
	114°	39.2%	
	115°	39.4%	
	119°	39.8%	

In Table 2.1 the surface contact angle of exfoliated $(C_8H_{17})_3P^+Cl^-$ biochar ranged from 114° to 119° . The variance in angle can be attributed to changes in relative humidity. The hydroxylated biochar had a 0° measurement due to the droplet of water evenly dispersing onto the surface of the biochar.

2.2.6 Alternative direct synthetic route to phosphonium-modified biochar

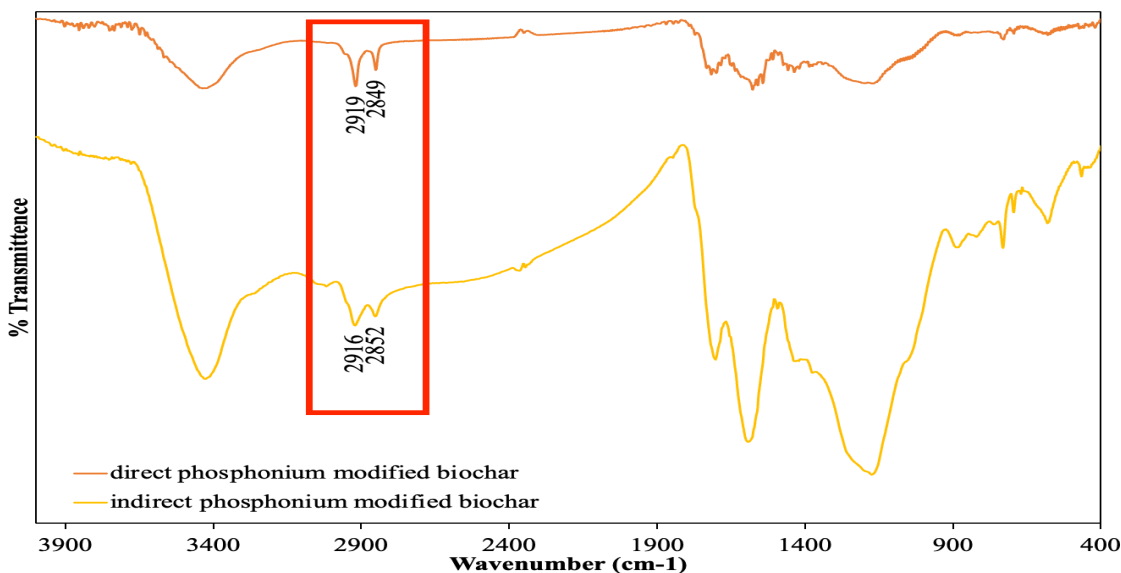


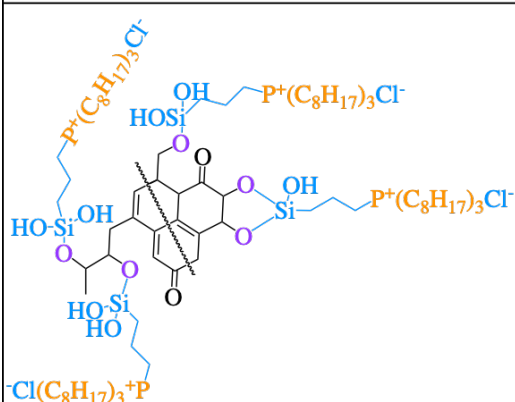
Figure 2.14 The FT-IR spectra of exfoliated $(C_8H_{17})_3P^+Cl^-$ biochar using direct synthesis (orange, top) and indirect synthesis (yellow, bottom) routes.

The products prepared by direct and indirect grafting methods are compared by FT-IR spectroscopy, **Figure 2.14**. Bands representing $-CH_2-$ and $-CH_3-$ surface groups at 2919 and 2849 cm^{-1} for the indirect synthesis and 2916 and 2852 cm^{-1} for the direct synthesis, respectively were observed. FT-IR spectroscopy cannot provide accurate quantitative data for identifying the degree of functionalization of the biochar in the solid-state.

2.2.7 Phosphorus quantification using $^{31}\text{P}\{^1\text{H}\}$ CPMAS NMR spectroscopy on exfoliated and non-exfoliated $(\text{C}_8\text{H}_{17})_3\text{P}^+\text{Cl}^-$ biochar

To determine the number of phosphonium groups on the surface of biochar, a known amount of $(\text{C}_8\text{H}_{17})_3\text{P}^+\text{Cl}^-$ biochar and triphenylphosphine (TPP) as an internal standard were analyzed by $^{31}\text{P}\{^1\text{H}\}$ CPMAS NMR spectroscopy. This allows measurement of the amount of phosphorus on the surface of the modified biochar shown in **Table 2.2**.

Table 2.2. The comparison of the synthesis conditions and % phosphorous added to the surface of biochar for phosphorus quantification—sample calculations are provided in Appendix 2.

Biochar	Synthesis	Hydroxylated biochar	% P added
	Indirect	Non-Exfoliated	1.3 %
	Indirect	Exfoliated	11.6%
	Direct	Exfoliated	18.0%

The results obtained from the quantification of phosphorus (**Table 2.2**) determined that the exfoliation of the hydroxylated biochar allowed for the degree of functionalization to be increased on the biochar surface. When comparing the two indirect synthetic pathways, a ten-fold increase was observed in the %P that was added to the surface after exfoliation. This is the first report of a significant rise in

functionalization through exfoliation.

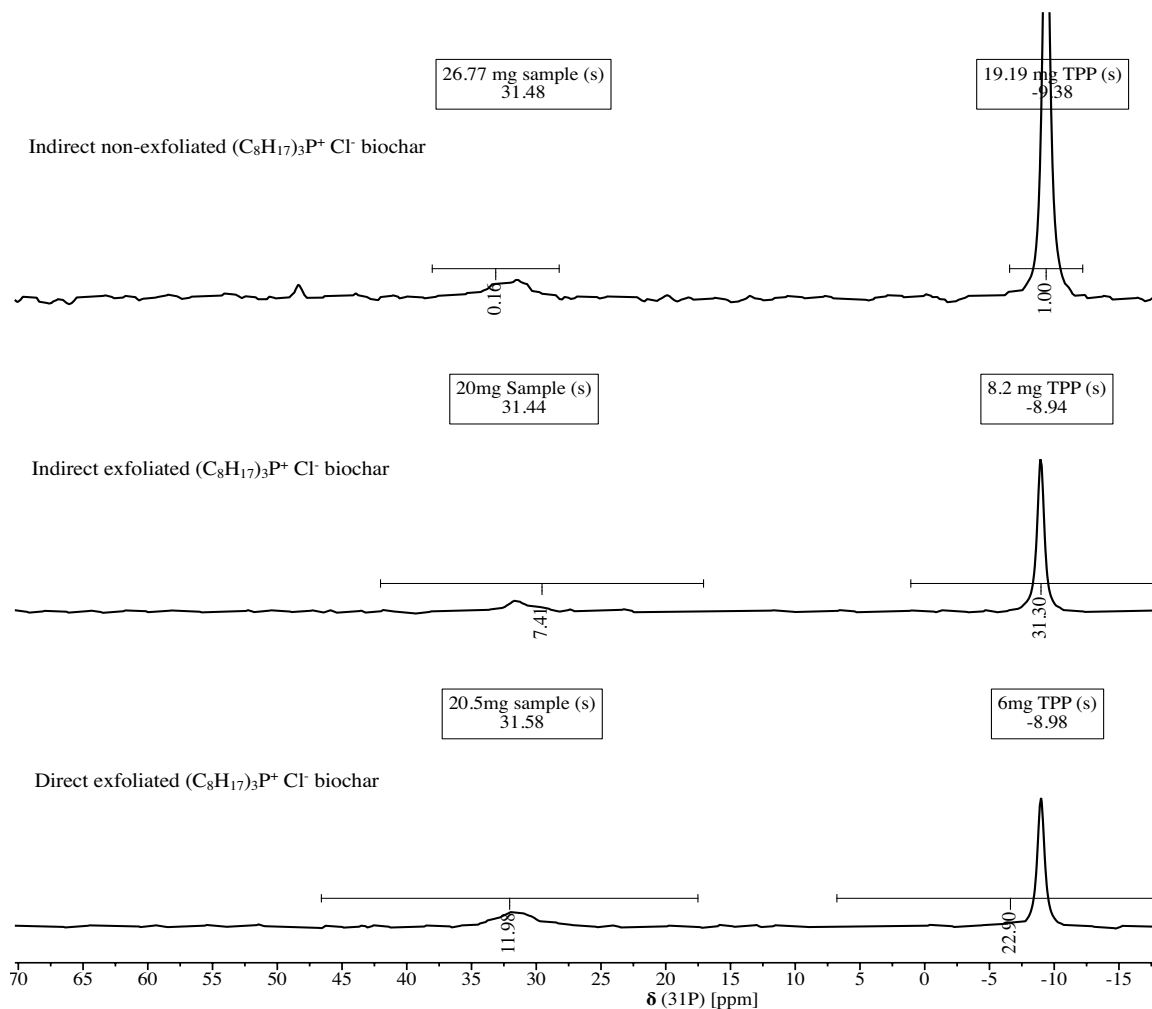


Figure 2.15 $^{31}\text{P}\{^1\text{H}\}$ CPMAS NMR spectra of indirect synthesis on non-exfoliated $(\text{C}_8\text{H}_{17})_3\text{P}^+\text{Cl}^-$ biochar (top), indirect synthesis on exfoliated $(\text{C}_8\text{H}_{17})_3\text{P}^+\text{Cl}^-$ biochar (middle), and direct synthesis on exfoliated $(\text{C}_8\text{H}_{17})_3\text{P}^+\text{Cl}^-$ biochar (bottom).

A 1.3–18% mass of phosphorus was seen across the phosphonium-added functionalized biochars, **Table 2.2**. The indirect synthesis applied on exfoliated hydroxylated biochar caused a 10.3% increase in mass of phosphorus atoms to the surface when compared with non-exfoliated hydroxylated biochar. The highest amount of phosphorus added to the surface of the exfoliated hydroxylated biochar was the

functionalization reaction via direct synthesis. The direct synthesis yielded a 6.4% increase in %P mass added to the surface compared to the indirect grafting route performed on exfoliated biochar.

2.3 Conclusion

Using a simple two-step synthesis, the first ever phosphonium-modified biochar is reported and characterized using FT-IR spectroscopy; $^{31}\text{P}\{^1\text{H}\}$, $^{13}\text{C}\{^1\text{H}\}$, ^1H CPMAS NMR spectroscopy and surface contact angle measurements. Quantification of %P added to the surface was completed with $^{31}\text{P}\{^1\text{H}\}$ CPMAS NMR spectroscopy; this is the first report of a specific heteroatom elemental analysis result by solid-state NMR spectroscopy, while elemental analysis (combustion, ICP-MS) is commonly used in the literature. This methodology can be applied to other functionalized biochar's that contain other heteroatom-specific functional groups that are continuously challenging to characterize using traditional methods.

2.4 Experimental

2.4.1 *General materials*

Unless stated otherwise, chemicals purchased for experimentation were obtained from Sigma Aldrich, Fisher Scientific and TGI Chemicals were used as received. Pristine biochar was obtained from Cape Breton University (MacQuarrie research group, Sydney, Nova Scotia), and commercially available solvents were used without purification, excluding deuterated chloroform (CDCl_3) that was distilled to remove the TMS standard.

2.4.2 *Characterization*

FT-IR spectroscopy

FT-IR spectra are obtained using a Bruker Alpha FTIR spectrometer. The samples were prepared in KBr with a ratio of 0.2:200 (Biochar: KBr by mass) and pressed into pellets. In transmission mode, the spectra were collected from 4000 to 400 cm^{-1} , with 4 cm^{-1} resolution and 24 scans for each collection. The spectra were corrected against a pure KBr pellet, and data were processed using OPUS data software.

Solid-state NMR spectroscopy

All ^1H , $^{13}\text{C}\{^1\text{H}\}$ and $^{31}\text{P}\{^1\text{H}\}$ CPMAS SSNMR spectra were observed at 298 K using a Bruker Avance II 600 MHz NMR spectrometer, equipped with a SB Bruker 3.2 mm magic angle spinning (MAS) triple-tuned probe operating at 600.29 MHz for ^1H , 150.93 MHz for ^{13}C and 243.00 MHz for ^{31}P nuclei. The samples were spun at 20 kHz for ^{13}C , and 10 kHz for ^{31}P . Cross-polarization (CPMAS) spectra were collected with a Hartmann-Hahn match at 62.5 kHz and 100 kHz ^1H -decoupling, a contact time of 2 ms and a recycling time of 5s. 8k scans (7 h) were collected for ^{13}C and 1k scans (1.5 h) for ^{31}P . Spectra were referenced externally to adamantane for ^{13}C and ADP for ^{31}P . A known mass of triphenylphosphine (TPP) was also added to the samples to estimate the %P on the surface of biochar.

Solution-state NMR spectroscopy

^1H , ^{13}C and ^{31}P NMR spectra were obtained on a Bruker Avance 300 MHz spectrometer at 298 K, with samples prepared in distilled CDCl_3 . Chemical shifts are

reported as ppm values and referenced to the residual protons and ^{13}C in CDCl_3 , and referenced to residual ^{31}P from trioctylphosphine in CDCl_3 .

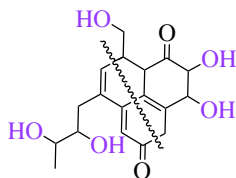
Surface contact angle measurement

The surface contact angle measurements were completed using a homemade setup following the same method reproduced by Zhang et al. with a hydrophobic biochar.³⁷ Samples were ground up to make a uniform particle size and pressed into a pellet using a pellet press with a 39.2–39.8 % RH. The relative humidity ranged from 39.2–39.8 %, and a 10 μL drop of deionized water was added to the smoothed surface; a picture was taken where the camera was level to the flat surface, and the contact angle was measured using J.js image processing software.⁶¹

2.4.3 Methods

Each of the following reactions was completed in a Radley carousel 12 Plus reaction station unless otherwise specified.

2.4.4 Synthesis of hydroxylated biochar



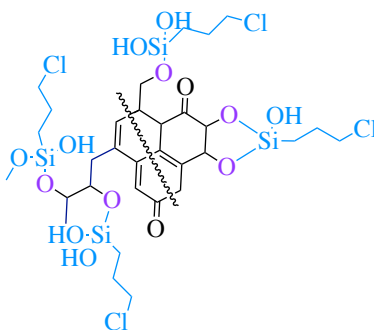
Procedure: Hydroxylated biochar was prepared by a modified Hummer's method^{57,58} In a three-neck round bottom flask, pristine hardwood biochar (1.01 g) is suspended in H_2SO_4 (10.0 mL) and is sonicated for 30 min. Next, the mixture is cooled in an ice bath until the temperature of the flask is below 10 °C, and KMnO_4 (1.00 g, 6.33 mmol) is added slowly.

Upon complete transfer, boric acid (1.6 mg, 0.03 mmol) is added, and suspension is stirred for 2 h. Deionized H₂O (25.0 mL) is added dropwise, the ice bath is switched with a silicon oil bath, and the reaction mixture is refluxed for 30 min. The suspension is cooled to room temperature, and H₂O₂ (1.2 mL) is added dropwise to the mixture. The resulting mixture is suction filtered, and the black solid is washed with HCl (1M, 6 mL), H₂O (5 mL) and EtOH (6 mL). The hydroxylated biochar (0.86 g, 85% mass recovered) is dried overnight in a vacuum oven at 50 °C to recover a black powdery solid. $\nu_{\max}/\text{cm}^{-1}$: 3419br and 1699w (OH), 1597vs and 869w (C=C), 1200vs and 1040m (CO).

2.4.5 Exfoliation of hydroxylated biochar

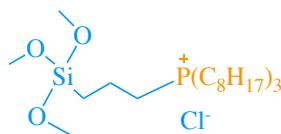
Procedure: In a 1000 mL round bottom flask, hydroxylated biochar (2.00 g) is suspended in ethyl acetate (500 mL); the mixture is sonicated for 30 min and the solids settle for 30 min.⁶ The suspended exfoliated hydroxylated biochar was siphoned off and dried under reduced pressure. Additional ethyl acetate was added to the remaining hydroxylated biochar that had settled in the round bottom flask, and the procedure was repeated until all hydroxylated biochar was exfoliated.

2.4.6 Synthesis of CPTMS biochar



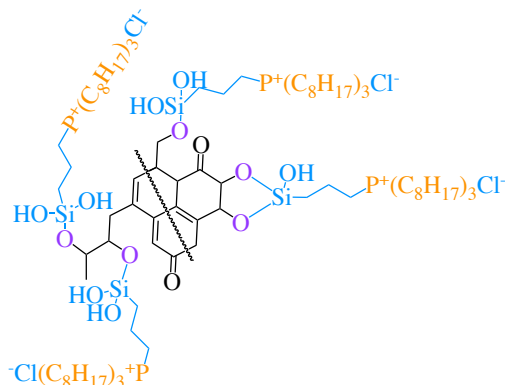
Procedure: Exfoliated and non-exfoliated hydroxylated hardwood biochar (200 mg) is suspended in anhydrous toluene (6.00 mL). Next, 3-chloropropyltrimethoxysilane, CPTMS, (0.62 g, 3.13 mmol) is added dropwise; the solution is refluxed and stirred for 24 h under a N₂ atmosphere. Finally, the reaction mixture was suction filtered, washed with toluene (3 × 20.0 mL), EtOH (1 × 10.0 mL) and solvent removed *in vacuo*. The resulting CPTMS-biochar (169 mg, 85% mass recovered) was a black powdery solid. $\nu_{\max}/\text{cm}^{-1}$: 3401br and 1700w (OH), 2894w (CH), 1597vs and 829w (C=C), 1237vs and 1018m (C–O), 1165vs (C–Si), 729w (Si–O), 692 (C–Cl). δC (600 MHz, solid) 127.8 (6 C, m, aromatic), 53.5 (2 C, s, CH₂–Si or –O), 21.2 (1 C, s, CH₂).

2.4.7 Synthesis of 3-(trioctylphosphonium chloride)propyltrimethoxysilane (TOPPTMS Cl⁻)



Procedure: The following procedure is modified by using acetonitrile as the solvent instead of toluene.⁶² CPTMS (1.00 mL, 5.50 mmol) is suspended in anhydrous acetonitrile (8.00 mL), trioctylphosphine, TOP, (7.30 mL, 16.5 mmol) is added dropwise, and the reaction mixture is refluxed and stirred under N₂ for 96 h. The organic layer is air dried under vacuum to yield TOPPTMS Cl⁻ (2.62 g, 84%) as a clear colourless oil. $\nu_{\text{max}}/\text{cm}^{-1}$: 2924vs (CH₃), 2852vs (C-H), 1088vs (Si-C), 1035vs (CO) and 919w The P-CH₂ band at 919 cm⁻¹. δH (300 MHz, CDCl₃) 3.56 (9 H, m, *SiOMe*), 2.38 (2 H, m, *PCH-CH2*), 1.90 (2 H, m, *Si-CH2*), 1.71-1.62 (6 H, m, *P-CH2*), 1.58-1.48 (12 H, m, *CH2*), 1.26 (24 H, m, *CH2*), 0.86 (9 H, t, *J*= 6.0 Hz, *CH3*), 0.70 (2 H, m, *CH2*). δP (300 MHz, CDCl₃): δ 32.15 (1 P, s, *R3'R''P+*).

2.4.7 Synthesis of $(C_8H_{17})_3P^+Cl^-$ biochar



Procedure 1: CPTMS-biochar (308 mg) is suspended in anhydrous. toluene (8.00 mL). Next, TOP (1.40 mL, 3.14 mmol) is added slowly dropwise to the reaction mixture. This reaction mixture was refluxed and stirred under N_2 for 96 h. Upon reaction completion, the mixture is suction filtered; the solid is washed with toluene (2×10.0 mL) and EtOH (2×10.0 mL). The black powdery solid is dried *in vacuo* and identified as the indirect synthesis of $(C_8H_{17})_3P^+Cl^-$ biochar (253 mg, 82%).

Procedure 2: TOPPTMS Cl^- (885 mg, 1.55 mmol) is suspended in anhydrous toluene (4.00 mL). Next, exfoliated hydroxylated biochar (205 mg) is added; this mixture is refluxed and stirred under N_2 for 24 h. Upon reaction completion, the mixture is the suction filtered; the solid is washed with toluene (2×20.0 mL) and EtOH (2×20.0 mL). The black powdery solid is dried under reduced pressure and identified as the direct synthesis of $(C_8H_{17})_3P^+Cl^-$ biochar (152 mg, 74%).

Characterization data: v_{max}/cm^{-1} : 3435vb and 1700wb (OH); 2919w (CH_3), 2846 (C–H), 1577vs and 877w (C=C); 1226vs and 1052w (CO); 1165vs (C–Si), 729w (Si–O), 692w (C–Cl). δC (600 MHz, solid) 127.2 (6 C, m, aromatic), 73.8 (1C, m, CH_2-PCl), 50.8 (1 C, s, CH_2-Si or $-O$), 31.0 (3 C, m, CH_2-P), 29.1 (6 C, m, CH_2), 27.2 (6 C, m, CH_2), 23.2

(1 C, s, CH_2), 14.8 (9 C, m, CH_3). δH (600 MHz, solid) 5.2 (2 H, bs, $C=CH_2$), 4.2 (H, bs), 4.0 (H, bs), 2.7 (2 H, m, $PCl-CH_2$), 2.1 (6 H, m, CH_2), 1.9 (2 H, m, $Si-CH_2$), 1.5 (12 H, m, CH_2), 1.2 (24 H, m, CH_2), 0.77 (9 H, bs, CH_3). δP (600 MHz, solid): 31.5 (1 P, s, $R_3'R''P^+$).

Co-Authorship Statement:

CHAPTER 3: Phosphonium-IL-modified biochar: electrochemical screening for suitability in supercapacitors

Sara M. K. Cheema, Francesca M. Kerton, Stephanie L. MacQuarrie, and T. Jane Stockmann.

Article in preparation to be submission

The first author (Sara M. K. Cheema) contributed 70% of the content of this article as the main researcher, including performing experiments, background literature reviews, collecting data, analysis of data and writing the manuscript.

The co-author (Francesca M. Kerton), my co-supervisor, was responsible for the original concept, suggested characterization experiments, revised and submitted the manuscript.

The co-author (Stephanie L. MacQuarrie), my primary supervisor, was the principal investigator of this work and was responsible for synthetic design, suggesting experiments, assisting with data interpretation and revising the manuscript.

The corresponding author (T. Jane Stockmann) was responsible for the original concept, for the experimental design, background literature review, suggesting experiments and assisting with data interpretation and revising the manuscript.

CHAPTER 3: Phosphonium-IL-modified biochar: electrochemical screening for suitability in supercapacitors

3.1 Introduction

A supercapacitor is an energy-storage device, that contains an electric double layer that can store a much larger capacity of energy and have fast charge/discharge rates compared with regular capacitors or batteries.⁶³ In supercapacitors, the electrode can be comprised of carbon-based materials such as activated carbon, graphite, graphene or nanocarbon tubes that increase energy storage compared with regular capacitors.^{64, 65, 66} These materials tend to have a high degree of conjugated species which contributes to high conductivity and capacitance that widely influences their application in energy storage devices.^{67, 68, 69} While carbon materials cannot be easily replaced in electrochemical storage applications, greener alternatives are being explored.⁷⁰

3.1.1 Biochar in supercapacitors

Biochar is a carbon-based material derived from renewable resources and is actively investigated as a green alternative for electrochemical applications such as batteries, sensors, and supercapacitors.^{22, 38} Biomass that has been pyrolyzed at higher temperatures (above 500 °C) increases the porosity and the surface area of the biochar, which has the potential to contribute to a higher capacitance when used in supercapacitor devices.⁴³ However, lower pyrolysis temperatures (under 500°C) have the added benefit of decreasing the energy expenditure needed to produce materials compared with activated carbon.⁷¹ Jisha et al. suggested that micropores (pore diameter = < 2 nm or < 20 Å) on biochar surface provide a high surface area that aids in the charging of

biochar.⁴⁰ While mesopores (pore diameter = $2 < 50$ nm or $20 < 500$ Å) allows good electrolyte wettability that increases the capacitance.⁴⁰ Although, biochar that has been pyrolyzed at lower temperatures exhibits poor conductivity.⁷² Functionalizing biochar by introducing heteroatoms such as S, O, N, and P may be required to enhance the electrode/electrolyte interaction on the surface of biochar when it is used as an electrode.⁷²

3.1.2 Ionic liquids in supercapacitors

Ionic liquids (ILs) are widely used in electrochemistry due to their tunable chemical properties such as excellent conductivity, wide electrochemical window, high viscosity, thermal stability, wide liquid range and tunable solvent properties.⁷³ In electrochemical applications, ionic liquids have found uses as electrolytes and can increase the electron density at the surface of a carbon-based electrode.^{74, 75, 76, 77}

Ionic liquids are commonly cationic and anionic species with properties governed by their substituents. The cations can include alkyl ammonium, alkyl phosphonium and alkyl imidazolium species with counter ions such as Cl^- , NTf_2^- , SO_4^{2-} and CH_3COO^- .⁷⁷ Phosphonium ILs have been demonstrated to have a wider electrochemical window and higher conductivity in electrochemical applications than ammonium ILs noted by Chen et al., based on characteristics of IL and poly-IL.⁷⁸ As an electrolyte, alkyl phosphonium ionic liquids can change specific capacitance by swapping the counter ion such as Cl^- , NTf_2^- and MeO^- as noted by Phillipi et al.⁷⁹

The electrochemical properties needed for a supercapacitor device was previously reported and discussed by Yiğit and coworkers using a conducting polymer-based

electrodes. This group applied cyclic voltammetry (CV) and galvanostatic charge-discharge (GCD) measurements on an assembled device with conducting polymer-based electrode using stainless steel plates and an electrolyte system soaked in filter paper.⁸⁰ In this thesis, we used a similar approach to study the functionalized biochar.

3.1.3 Electrochemical characterization

The electrochemical properties of functionalized biochar for electrodes are assessed with CV and GCD measurements to understand its electrochemical stability, and capacitance.⁸¹ The CV provides information on the stability of the material by reporting any oxidation or reduction reactions occurring on the surface of the modified biochar electrode and to identify its electrochemical potential window.⁸² To define the capacitance of functionalized biochar using GCD, the area under the discharge curve is assessed as a function of time using the non-linear capacitance equation defined recently in a review by Mathius et al. for a pseudocapacitor (equation 1).⁸¹

$$C(Fg^{-1}) = I \int \left(\frac{1}{V(t)} \right) dt \quad \text{Equation (1)}$$

Where I is the applied constant-current density, t is the discharge time, and $V(t)$ is the potential as a function of t .⁸¹

The identification of the electrochemical window and capacitance determines the suitability of biochar electrodes for use in supercapacitors. The factors that influence this for carbon-based electrodes are the particle size of the material, the electrolyte system and the surface interactions.⁸³ Lyu et al. reported a biochar surface-modified glassy carbon electrode using a decreased particle size biochar that was processed using a ball

mill. This 3-electrode cell was analyzed by CV in 5.00 mM $K_3Fe(CN)_6$ and 0.10 M KCl electrolyte systems, they compared the ball-milled biochar to pristine biochar. This group reported an increased electrical conductivity to the milled biochar when testing the redox reduction of $K_3Fe(CN)_6$.⁸⁴ The electrolyte systems are responsible for the electron exchange that occurs on the surface of the electrode. Thus, surface-modified biochar electrodes have also been made using functionalized biochar reported by Stephanie et al.⁸⁵ The sulfonated and aminated biochar was used for water desalination, demonstrating an increase in capacitance and a decrease in the resistive behaviour of biochar. The system's effectiveness was tested by CV and GCD in a 3-electrode cell with a 100 mM NaCl electrolyte solution. The sulfonated and aminated functionalized biochar had a specific capacitance of 24.29 and 17.75 F/g at scan rates of 5 and 10 mV/s, respectively.⁸⁵ The influence of varying scan rates and covalent functionalization on biochar surface demonstrates an increase in the capacitance of biochar. In this work, the electrochemical properties of pristine hardwood biochar and covalently bound phosphonium ionic liquids on the surface of hydroxylated hardwood biochar are reported for supercapacitor applications.

3.1.4 Synthesis of phosphonium salt-IL-modified biochar

The synthesis of phosphonium-IL-modified biochar in figure 3.1 is completed in 3 or 4 synthetic steps, consisting of hydroxylation, siloxane condensation and phosphonium modification. Steps 1, 2 and 3 are described in detail in Chapter 2.

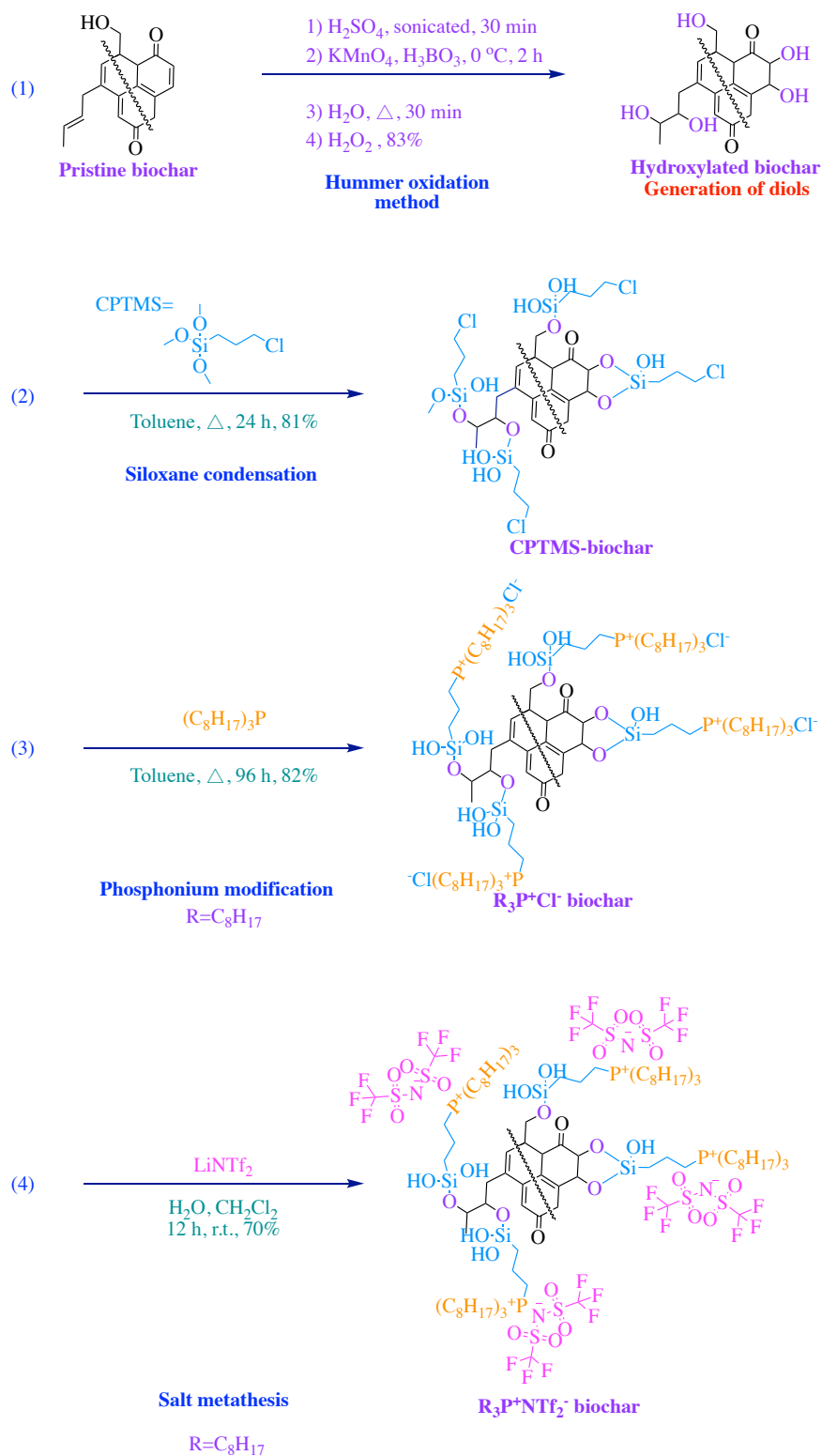


Figure 3.1 Synthesis of phosphonium-IL-modified biochars under investigation. (3 and 4)

The fourth step is a salt metathesis reaction between LiNTf_2 and $(\text{C}_8\text{H}_{17})_3\text{P}^+ \text{Cl}^-$ biochar to exchange the counter-ion for the production of $(\text{C}_8\text{H}_{17})_3\text{P}^+ \text{NTf}_2^-$ biochar. This will allow the counter-ion effects of the functionalized biochars to be evaluated.⁸⁶ Counter-ion effects can result in differing energy storage properties, such as diffusivity and electron transport, that contribute to an increased capacitance.⁸⁶ The phosphonium salt-IL-modifications are confirmed using heteroatom-specific solid-state NMR spectroscopy, ($^{31}\text{P}\{^1\text{H}\}$ and $^{19}\text{F}\{^1\text{H}\}$ CPMAS). In addition, the surface morphology of phosphonium salt-IL-modified biochar is assessed by transmission electron microscopy (TEM), surface area determined by Brunaur-Emmet-Teller (BET) analysis, and crystallinity by powder X-ray diffraction (pXRD).

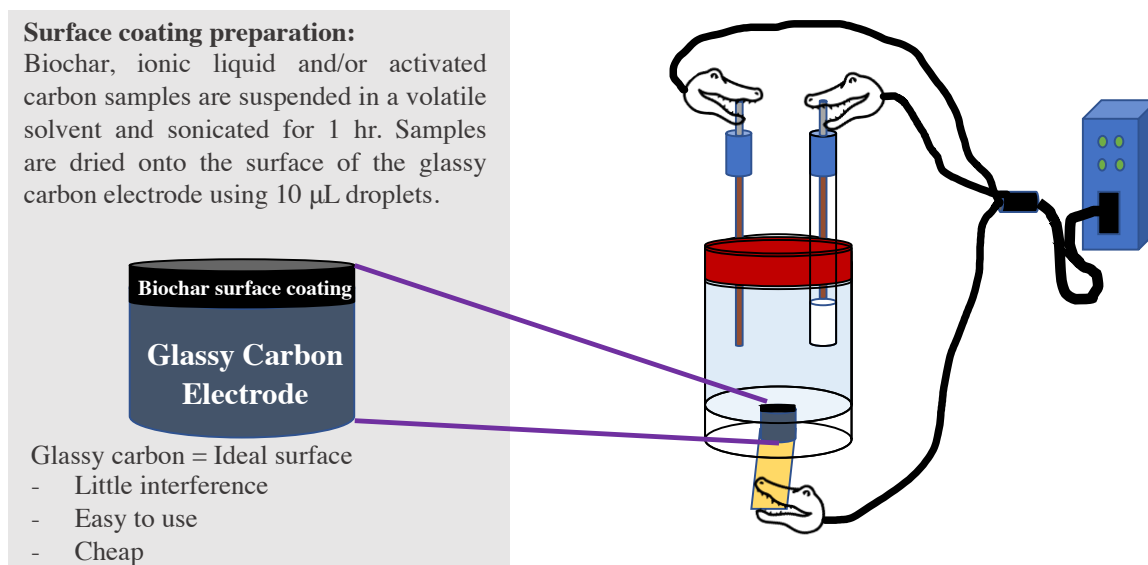


Figure 3.2 Surface coating preparation method and electrochemical cell using Teflon cup using Ag/AgCl reference electrode, Pt(s) counter electrode and functionalized biochar surface modified working electrode.

To screen biochar's electrochemical properties, the 3-electrode cells (**Cell I** and **Cell II**) with an experimental set-up consisting of a Pt/C wire auxiliary electrode, a saturated KCl Ag/AgCl reference electrode and a surface-modified working electrode

were used. The first set-up, Cell I, shown in figure 3.2, used a surface-modified glassy carbon working electrode fitted into a Teflon cup and filled with an aqueous electrolyte solution to submerge the electrodes. The second setup, Cell II, used a H-cell with surface-modified carbon paper for the working electrode to control the cell's atmosphere. For each of these cells, the supporting electrolyte systems were first 1.00 M NaCl, then switched to 100 mM Na₂SO₄ and 10 mM LiNTf₂ due to solubility and stability challenges.⁸⁷

The surface coating ink was prepared by adding ionic liquids, trihexyltetradecylphosphonium bromide (P_{6,6,6,14}Br) or trihexyltetradecylphosphonium bis(trifluoromethyl sulfonyl)imide (P_{6,6,6,14}NTf₂) to the biochar. The ionic liquid selection corresponded to the counter ion being either the same or similar to the modified biochar to make the surface coating ink.⁸⁸ In figure 3.2, the surface coating preparation method is noted, and 7 surface coatings were prepared and analyzed by CV and GCD.

Table 3.1 Electrode composition summary

Electrode	Cell	IL	Biochar and/or carbon
A	I	P _{6,6,6,14} Br	(C ₈ H ₁₇) ₃ P ⁺ Cl ⁻ biochar
B	I	P _{6,6,6,14} NTf ₂	(C ₈ H ₁₇) ₃ P ⁺ NTf ₂ ⁻ biochar
C	II	P _{6,6,6,14} Br	(C ₈ H ₁₇) ₃ P ⁺ Cl ⁻ biochar
D	II	P _{6,6,6,14} NTf ₂	(C ₈ H ₁₇) ₃ P ⁺ NTf ₂ ⁻ biochar
E	I	P _{6,6,6,14} Br	(C ₈ H ₁₇) ₃ P ⁺ Cl ⁻ biochar and activated carbon
F	I	P _{6,6,6,14} Br	Activated carbon
G	I	P _{6,6,6,14} NTf ₂	Pristine biochar

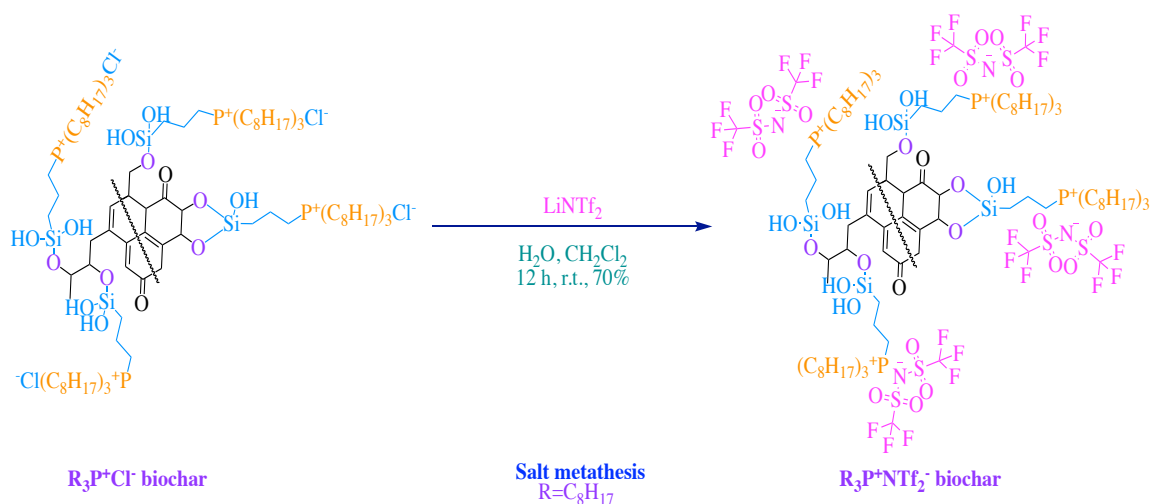
In table 3.1, the phosphonium-IL-modified biochar surface coating was a mixture of (C₈H₁₇)₃P⁺ Cl⁻ biochar with P_{6,6,6,14}Br for electrodes A and C in Cell I and Cell II. The (C₈H₁₇)₃P⁺ NTf₂⁻ biochar with P_{6,6,6,14} NTf₂ for electrodes B and D in Cell I and II. Many

literature procedures mix activated carbon, graphene and/or graphite when preparing their biochar surface coatings. Thus, a direct comparison of $(C_8H_{17})_3P^+$ biochar, $P_{6,6,6,14}Br$ and activated carbon of electrode E is reported to compare activated carbon with the ionic liquid in this system of electrode F. Next, pristine biochar with $P_{6,6,6,14}Br$ for electrode G is used to compare and confirm the modification of biochar to phosphonium-IL-modified biochar. Other routes to achieve phosphonium-IL-modification ball-milling with TOP can be applied to limit the use of solvent during the reaction step.

3.2 Results and Discussion

3.2.1 Preparation and characterization of $(C_8H_{17})_3P^+ NTf_2^-$ biochar

Phosphonium-IL-modified biochar was synthesized using the non-exfoliated indirect phosphonium-modified biochar method reported in Chapter 2. The added synthetic step in scheme 3.1 is a salt metathesis reaction that had a mass recovery of 70% that displaces the chloride counterion and replaces it with a bis(trifluoromethyl sulfonyl)imide (NTf_2^-) salt.



Scheme 3.1 Salt metathesis reaction of phosphonium bistriflimide-IL-modified biochar.

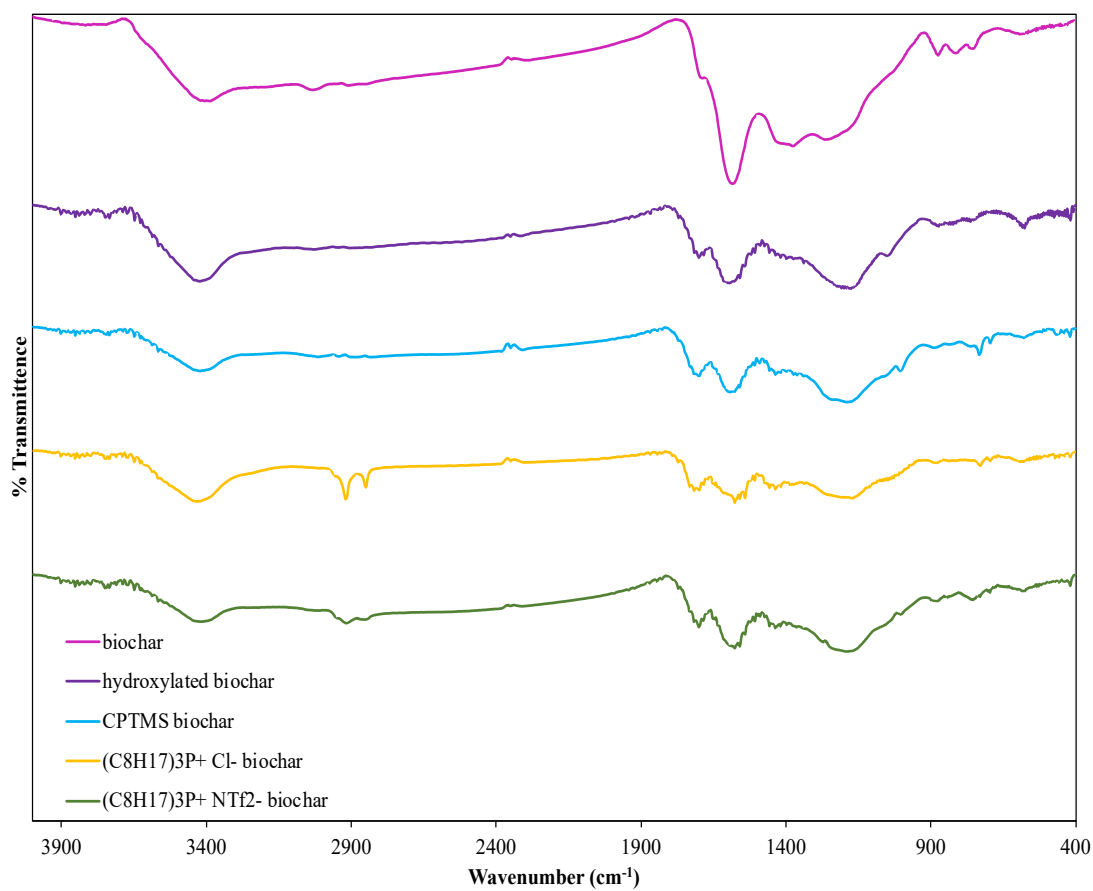


Figure 3.3 FT-IR spectra stacked of pristine biochar (pink, row 1), hydroxylated biochar (purple, row 2), CPTMS-biochar (blue, row 3), (C₈H₁₇)₃P⁺ Cl⁻ biochar (orange, row 4), and (C₈H₁₇)₃P⁺ NTf₂⁻ biochar (green, row 5).

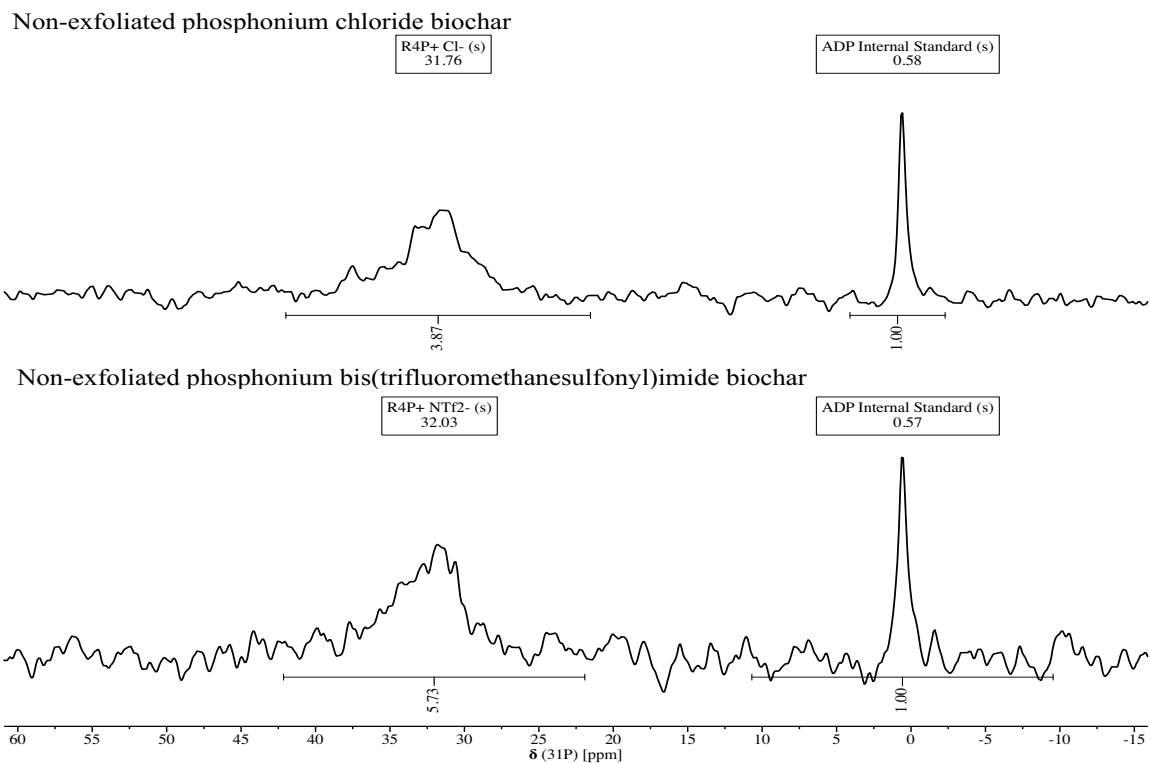


Figure 3.4 $^{31}\text{P}\{^1\text{H}\}$ CPMAS NMR spectra of $(\text{C}_8\text{H}_{17})_3\text{P}^+\text{Cl}^-$ biochar (top) and $(\text{C}_8\text{H}_{17})_3\text{P}^+\text{NTf}_2^-$ biochar (bottom).

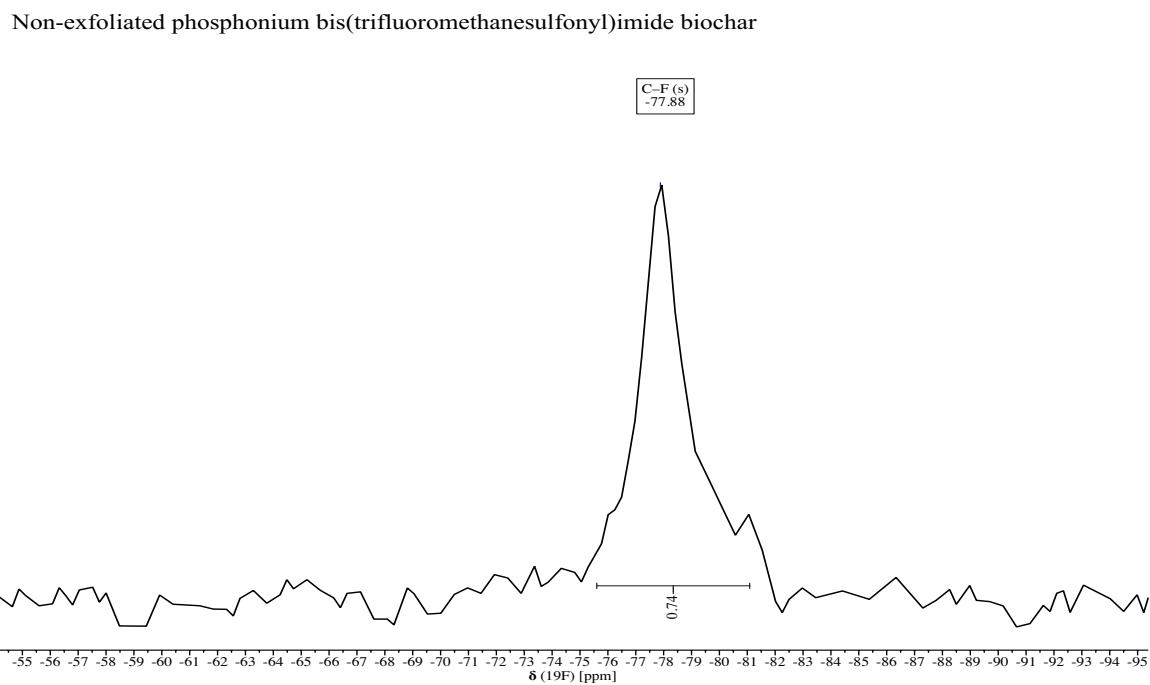


Figure 3.5 $^{19}\text{F}\{^1\text{H}\}$ CPMAS NMR spectra of $(\text{C}_8\text{H}_{17})_3\text{P}^+\text{NTf}_2^-$ biochar.

The salt metathesis reaction was difficult to characterize by FT-IR spectroscopy, figure 3.3, because, as expected, it did not result in significant differences in functional groups after the metathesis reaction. Therefore, characterization was completed using solid-state NMR spectroscopy. The phosphonium signal of both phosphonium salt-IL-modified biochars reported had the same ^{31}P shift regardless of the counterion (figure 3.4), at 31.8 ppm for the chloride salt biochar and 32.0 ppm for bis(trifluoromethyl sulfonyl)imide salt biochar. The $(\text{C}_8\text{H}_{17})_3\text{P}^+\text{NTf}_2^-$ biochar is an excellent candidate for more heteroatom-specific solid-state NMR spectroscopy, so the ^{19}F CPMAS NMR spectrum of this biochar is reported in figure 3.5. The trifluoromethyl functional group in the modified biochar had a chemical shift of -77.8 ppm, which has the similar shift that related NTf_2^- ILs that have a ^{19}F resonance at -78 ppm.⁸⁹

3.2.2 Surface morphology study of functionalized biochar

Scanning electron micrographs of the biochar showed rod-like structures in figure 3.6.

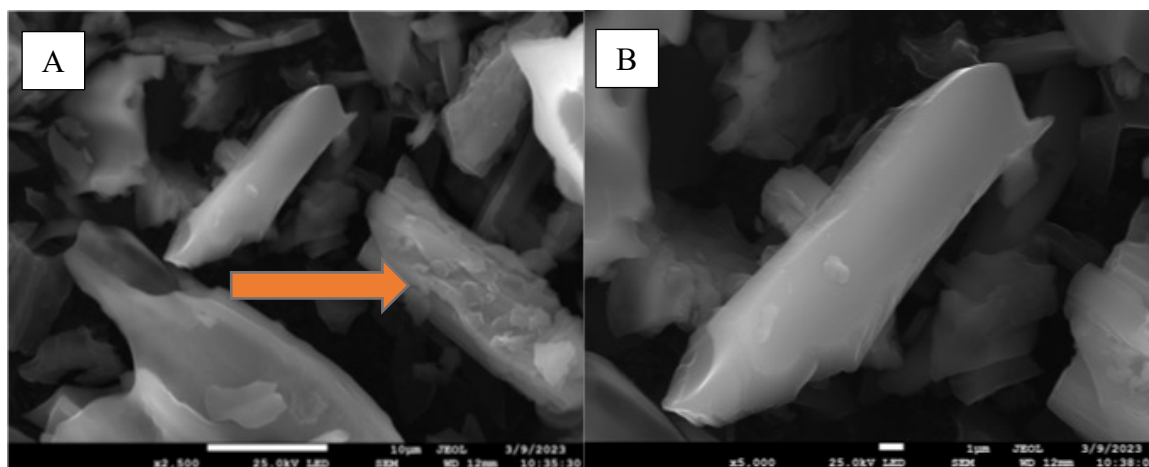


Figure 3.6 SEM images of $(\text{C}_8\text{H}_{17})_3\text{P}^+\text{Cl}^-$ biochar showing rod-like formations. Scale bars: (a) 10 μm and (b) 1 μm . The Orange arrow is showing rough spherical surface of biochar.

Vidal et al. reported oxidized hardwood biochar³⁴ SEM images to have a rough surface with rounded spheres that was confirmed using SEM electron dispersive X-ray (SEM-EDX) spectroscopy to have the elemental composition of mainly carbon-oxygen. In figure 3.6 B, the $(C_8H_{17})_3P^+Cl^-$ biochar has components of smooth rod-like materials and as well as some rod-like materials having rougher spherical surfaces (figure 3.6 A, orange arrow), larger ions may be visible by AFM but not by SEM images.

Surface area and pore diameter values were determined gas-isotherm experiments following Brunauer-Emmet-Teller (BET) theory of exfoliated and non-exfoliated $(C_8H_{17})_3P^+Cl^-$ biochar, in table 3.2. The two phosphonium chloride-IL-modified biochars exhibited similar surface areas of 2.0 and 2.3 m²/g, respectively, and pore diameters of 69 and 65 Å, respectively. The surface area reported previously for the hardwood biochar by Vidal et al reported a surface area of 231 m²/g and a pore diameter of 29 Å.³⁴ The significantly lower surface area can be expected for post modified biochars, the larger pore diameters can also confirm the change in the surface and confirm post-modification.

Table 3.2 BET measurements of exfoliated and non-exfoliated phosphonium chloride biochar.

$(C_8H_{17})_3P^+Cl^-$ biochar	Surface area (m ² /g)	Pore diameter (Å)
Indirect exfoliated	2.0	69
Indirect non-exfoliated	2.3	65

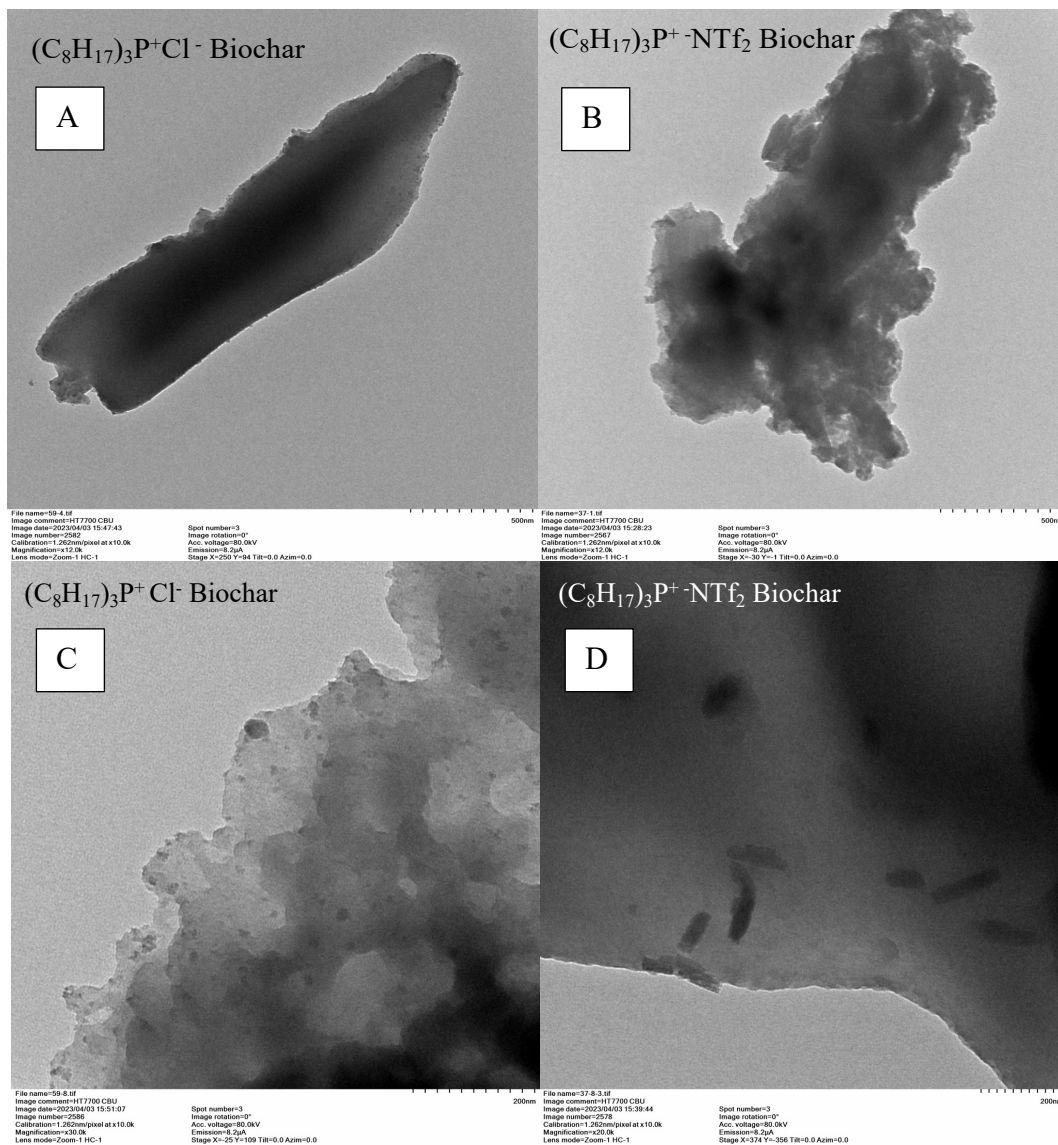


Figure 3.7 TEM images of $(C_8H_{17})_3P^+Cl^-$ biochar (left, A and C) and $(C_8H_{17})_3P^+NTf_2^-$ biochar (right, B and D). Scale bars: 500 nm (top) and 200 nm (bottom)

In figure 3.7 the TEM images of $(C_8H_{17})_3P^+ Cl^-$ and $(C_8H_{17})_3P^+ NTf_2^-$ biochar displays smoother surfaces and rougher surface, respectively. The $(C_8H_{17})_3P^+ Cl^-$ biochar contains rod-like structures with smooth edges in figure 3.7 A while $(C_8H_{17})_3P^+ NTf_2^-$ biochar has rougher rod-like structures with tiny round pores shown in figure 3.7 B. In the TEM images at higher magnifications comparing figure 3.7 C and 3.7 D, $(C_8H_{17})_3P^+$

Cl⁻ biochar does not look as smooth, whilst (C₈H₁₇)₃P⁺ NTf₂⁻ biochar is much smoother at a higher magnification. These surface qualities were then compared to a well-studied material such as activated carbon that has demonstrated high conductivity/capacitance.

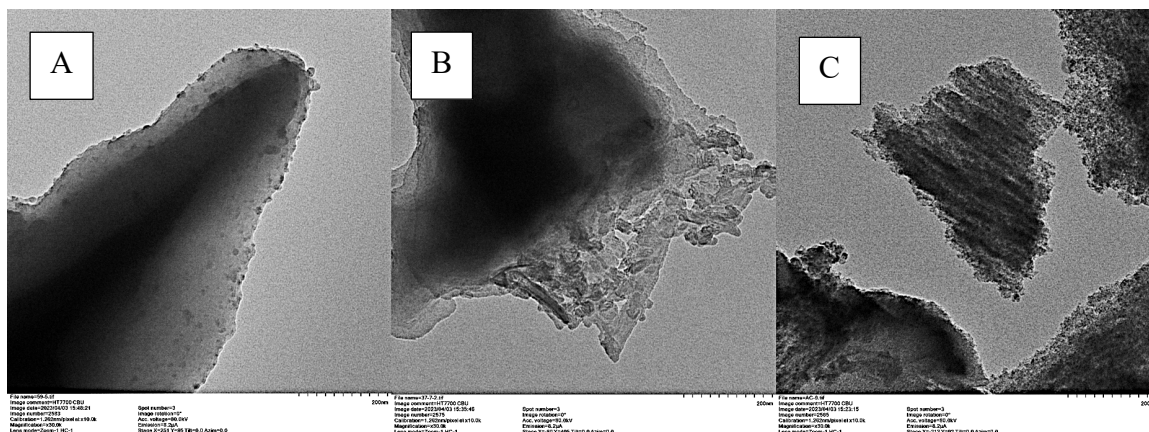


Figure 3.8 TEM images of (C₈H₁₇)₃P⁺ Cl⁻ biochar (left, A) and (C₈H₁₇)₃P⁺ NTf₂⁻ biochar (middle, B) and activated carbon (right, C). Scale bars: 200 nm.

Phosphonium-IL-modified biochar is an amorphous material shown in figure 3.8 A and B by the small rounded edges on the surface. The (C₈H₁₇)₃P⁺ Cl⁻ biochar demonstrated a lower resistance than (C₈H₁₇)₃P⁺ NTf₂⁻ biochar, where the roughness on the surface could have provided more surface area for electrolytic ions to coat. Activated carbon (figure 3.8 C) seems to be more ordered and shows layering which is desirable for electrochemical devices.

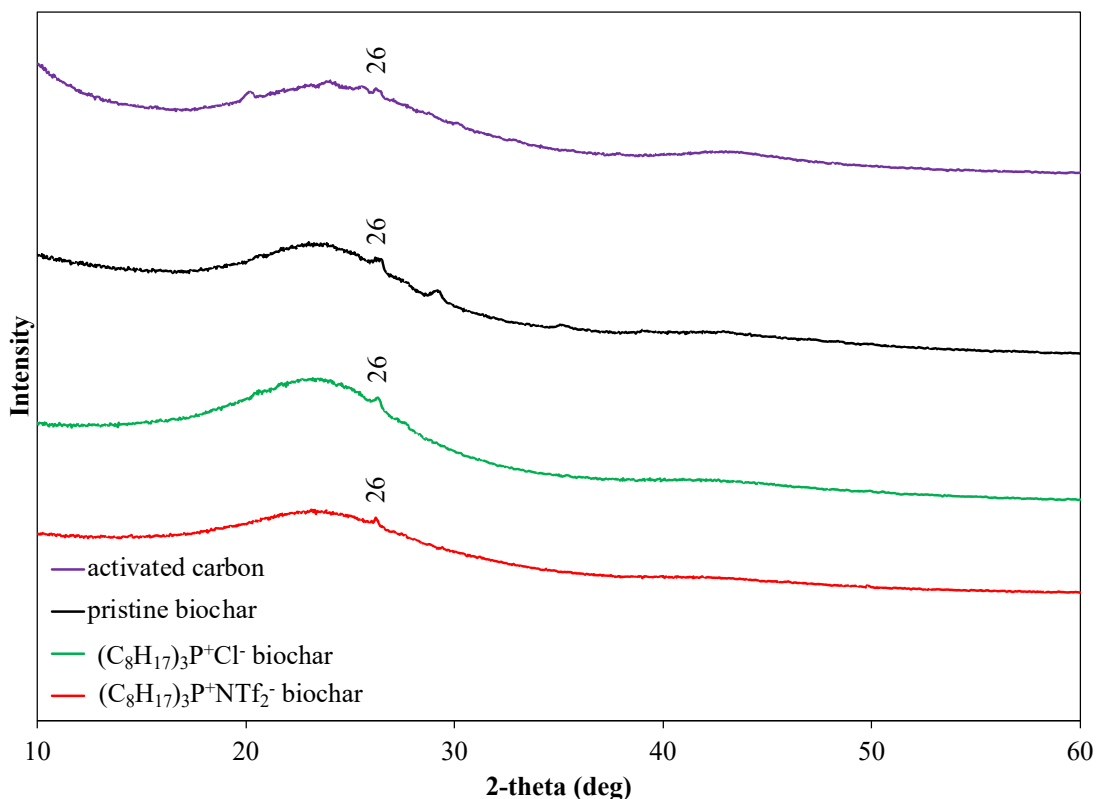


Figure 3.9 pXRD diffractograms of activated carbon, pristine biochar and phosphonium salt-IL-modified biochar. Diffractograms off-set on the y-axis for clarity.

To identify the crystallinity of carbon-based materials, powder XRD (figure 3.9) is used. For activated carbon, pristine biochar, (C₈H₁₇)₃P⁺ Cl⁻ and (C₈H₁₇)₃P⁺cNTf₂⁻ biochar diffractograms show each material being amorphous. However, each contain a peak at 26° that has been reported to indicate the presence of silica, with is in agreement with Kim et al. results for quartz peaks.⁹⁰ The broad peak from 15° to 30° indicate the presence of small crystals on the surface of that is perpendicular to the aromatic layers reported by Yea *et al.*⁹¹

3.2.3 Electrochemical study of functionalized biochar, pristine biochar and activated carbon with ionic liquid surface coating

The effect of phosphonium modification on the electrochemical properties of biochar is shown in figure 3.10 by the GCD curve characteristics. The modified and non-modified biochar demonstrated pseudocapacitive behaviour evidenced by the non-linearity of the discharge curve (GCD, electrode A), as described by Mathius et al.⁸¹ The GCD for pseudocapacitors can be identified by three features, as labelled in figure 3.10 i:

- (1) IR drop is the uncompensated resistance across the interface which leads to a sudden voltage change once the applied current is removed. During the initial charging step, the potential gradually increases until the constant applied current is stopped, in this case at 20 s (Figure 3.10i), at which point a rapid decrease in the potential-time plot was observed; this segment of the GCD curve is referred to as the IR drop.
- (2) One pseudocapacitive discharge region.
- (3) Second discharge region and approach to complete discharge of electrolytes from the surface of each material.⁸¹

The specific capacitance of the electrodes is determined by the area under the curve from regions (2) to (3).⁸¹ IR is the decrease in effective potential applied to the EDL, IR drop is often the result on charging the electrode surface beyond its capacitive limit along with parasitic electrolyte redox reactions or even resistances from instrument cabling.⁹² This follows Ohm's law (equation 2),

$$V = IR \text{ or } R = \frac{V}{I} \text{ and } G = \frac{I}{V} \quad \text{Equation (2)}$$

This describes the surface interaction to charge being resistive (R) or conductive (G) and describes susceptibility to charge transfer. In equation (2), V is the potential flow across the interface, and I is the current. Factors that affect conductivity are the concentration of ions, types of ions, the electroactive surface area of the electrode, and the temperature of the solution. Herein, the electrode surface areas were modified, the concentration and type of supporting electrolyte ions were investigated.

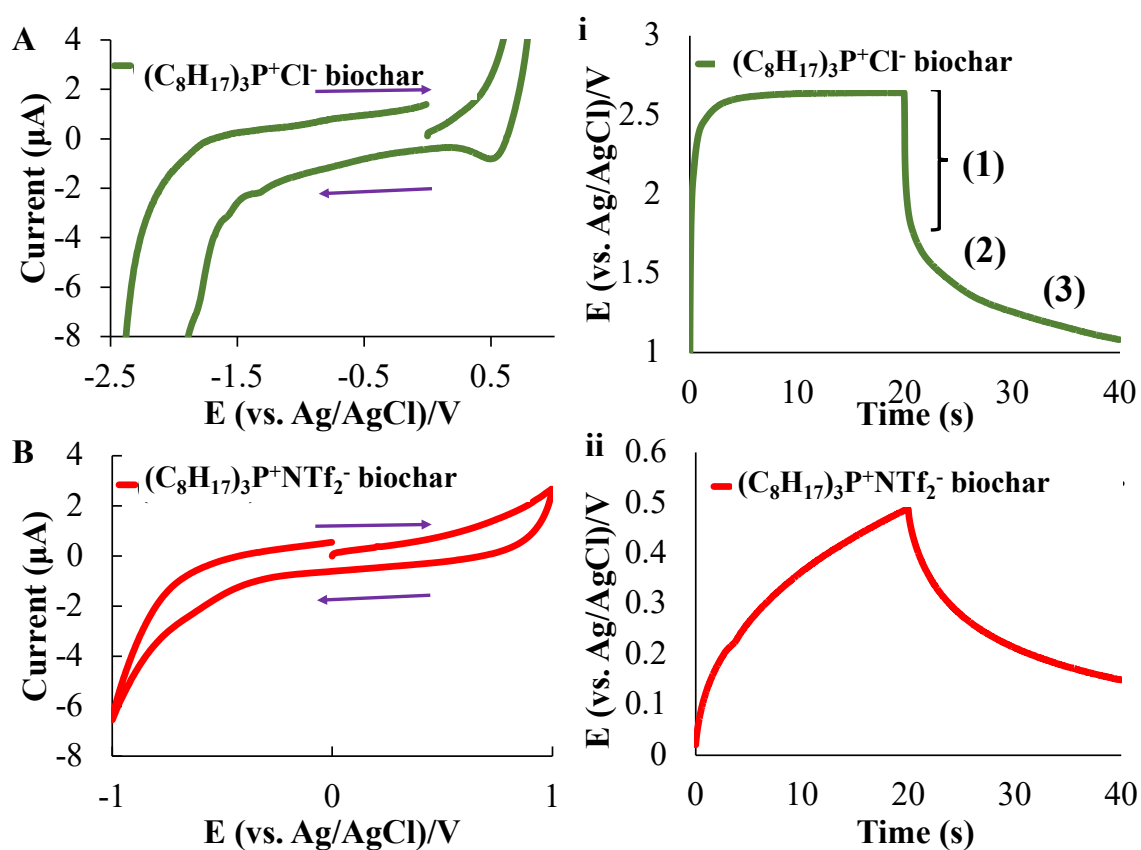


Figure 3.10 A and B Cell I: Cyclic voltammograms of electrode A (green, top) and B (red, bottom) with a 50 mV/s scan rate. (first column). **i.** and **ii.** The GCD of electrodes A (green, top) and B (red, bottom) using an applied current of 150 μA and 0.6 μA , respectively. (second column) The electrolyte systems used for electrodes A and B are 100 mM Na_2SO_4 and 10 mM LiNTf_2 solutions, respectively.

Cyclic voltammograms recorded using the phosphonium-IL-modified biochar surface coatings used in the Teflon cup (Cell-I) are shown in figures 3.10 A and B, using electrodes A and B, respectively. These electrodes (A and B) show relatively wide potential windows made possible with IL-modified carbon-based biochars. Electrode A and electrode B had potential windows of 2.57 V and 1.20 V, respectively. A cathodic peak at -1.45 V in figure 3.10 A is likely N_2 reduction. The GCD of electrode A under an applied current of 150 μA was determined to have a capacitance of 3.52 F/g via integration of regions 2 and 3 of the GCD curve. The IR drop region is present from 20.0 s to 20.62 s and was excluded from capacitance calculations. For electrode B in figure 3.10 B, the GCD measurement was completed under an applied current of 0.6 μA with a calculated capacitance of 0.08 F/g. Among the two phosphonium-IL-modified biochar samples, the $(\text{C}_8\text{H}_{17})_3\text{P}^+\text{Cl}^-$ biochar produced higher capacitance and a larger potential window (electrode A). This demonstrated the significance of the counter-ion effects for the two functionalized biochar.

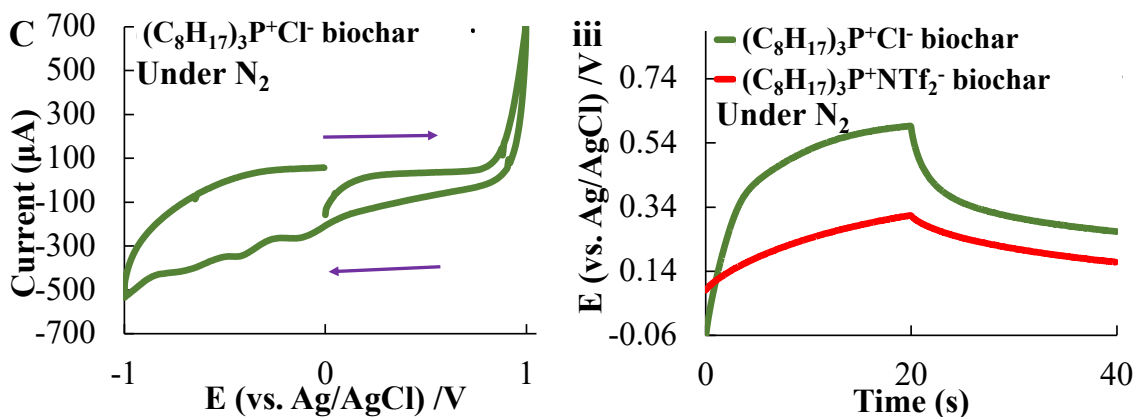


Figure 3.11 A Cell II: Cyclic voltammogram of electrode C prepared on carbon paper with a scan rate of 50 mV/s. (green, left) **iii.** The GCD measurements of electrodes C and D using an applied current of -132 μA and -4 μA , respectively. (right) The electrolyte systems used for electrodes C and D are 100 mM Na_2SO_4 and 10 mM LiNTf_2 solutions, respectively.

To eliminate the error from oxidation that occurs in air, the phosphonium-IL-modified biochar glassy carbon electrodes (Cell-I) were next tested using an H-cell (Cell-II). The surface modification was applied by deposition of the ionic liquid/biochar mixture onto carbon fiber paper electrodes (Cell-II), in which the cells were bubbled for 30 min with N_2 gas, for the measurement to be under inert conditions. The potential window of electrode C was 1.70 V in figure 3.11 C. The cathodic peaks for $(\text{C}_8\text{H}_{17})_3\text{P}^+\text{Cl}^-$ biochar was observed at -0.22 V, -0.53 V, and -0.84 V, which indicate other side reactions occurring on the material's surface that could affect the material's stability. For electrode C, GCD provided a measured capacitance of 1.22 F/g under an applied current of 132 μA , taken from the area under the curve from 20.06 s to 40.0 s. In this case, the IR drop is observed between points from 20.00 s to 20.06 s. Electrode D reports a potential window being 1.40 V in figure 3.11 D, which is close to the potential window of electrode B (1.20 V). For electrode D, the GCD measurement used an applied current of

4.00 μA with a calculated capacitance of 0.05 F/g and demonstrated no notable IR drop. The capacitance for $(\text{C}_8\text{H}_{17})_3\text{P}^+\text{Cl}^-$ biochar was superior to $(\text{C}_8\text{H}_{17})_3\text{P}^+$ NTf₂⁻ biochar, where the modified $(\text{C}_8\text{H}_{17})_3\text{P}^+\text{Cl}^-$ biochar's surface has been demonstrated to have a slower discharge based on time in cell II than in cell I. By using carbon fibre paper (CFP) instead of a glassy carbon electrode (GCE), there is notably a wider potential for the $(\text{C}_8\text{H}_{17})_3\text{P}^+\text{Cl}^-$ biochar in the cell I (2.57 V) compared to cell II (1.70 V). However, in cell II there was an increased discharge time. The CFP has a high surface area, and many biochar electrodes have large amounts of activated carbon incorporated to give surface-modified mixtures. Therefore, $(\text{C}_8\text{H}_{17})_3\text{P}^+\text{Cl}^-$ biochar was studied further to improve capacitance with activated carbon and ionic liquid mixtures.

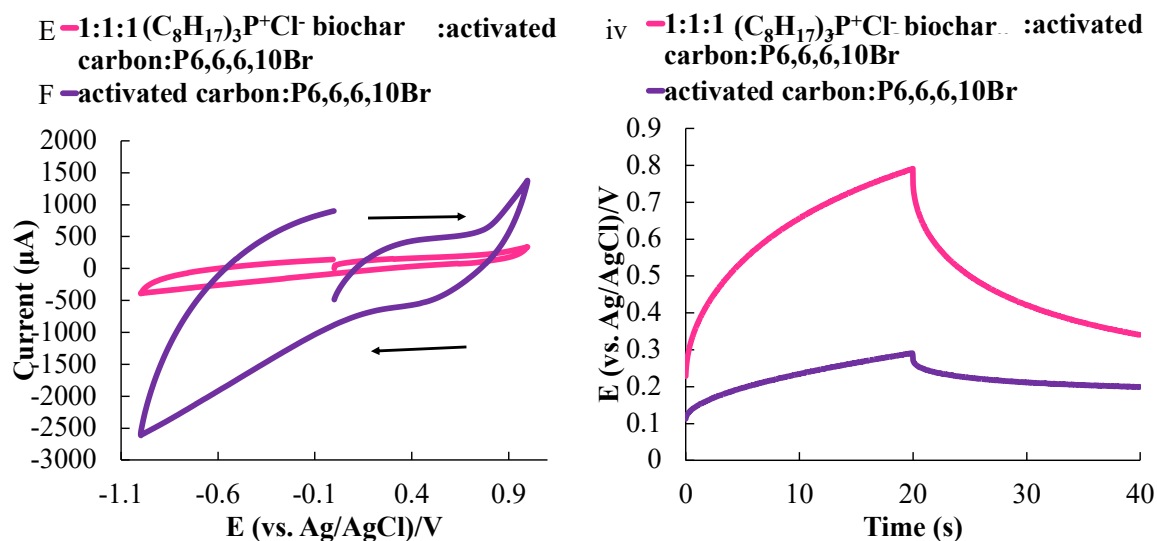


Figure 3.12 Cell I: E, F Cyclic voltammograms with a scan rate of 50 mV/s (left) and GCD measurements (iv) using an applied current of 150 μA (right) in 1.0 M NaCl (iv) of E (pink) and F (purple) modified electrodes.

Most reported biochar electrodes are made up of combinations of activated carbon/ graphite/ graphene and binding materials to help increase the surface area/conductivity of the surface-modified electrode.^{32, 93, 94, 64} In figure 3.12, the electrode is $(C_8H_{17})_3P^+ Cl^-$ biochar mixed with activated carbon and $P_{6,6,6,14}Br$ electrode (electrode E) and a blank electrode of activated carbon and $P_{6,6,6,14}Br$ (electrode F). Electrode E and F have potential windows of 1.89 V and 0.59 V, respectively, at a scan rate of 50 mV/s using 1.0 M NaCl. The GCD measurements of electrodes are in figure 3.12 iv with and without $(C_8H_{17})_3P^+ Cl^-$ biochar with a capacitance determined to be 11.0 F/g and 29.3 F/g, respectively, under an applied current of 150 μA . The IR drop for the blank was excluded in calculations from 20.0 s to 20.8 s. The $(C_8H_{17})_3P^+ Cl^-$ biochar demonstrates its resistance by its capacitance at 11.0 F/g, which lowers the capacity of the blend when compared to the blank 29.3 F/g. Adding activated carbon increased capacitance in comparison to electrode A (3.52 F/g in 100 mM Na_2SO_4) and electrode C (1.22 F/g). The added porous activated carbon material increased the electrodes capacitance, however, the use of activated carbon is not environmentally sustainable.⁷¹ Therefore, a screening of pristine biochar was completed to get a direct comparison.

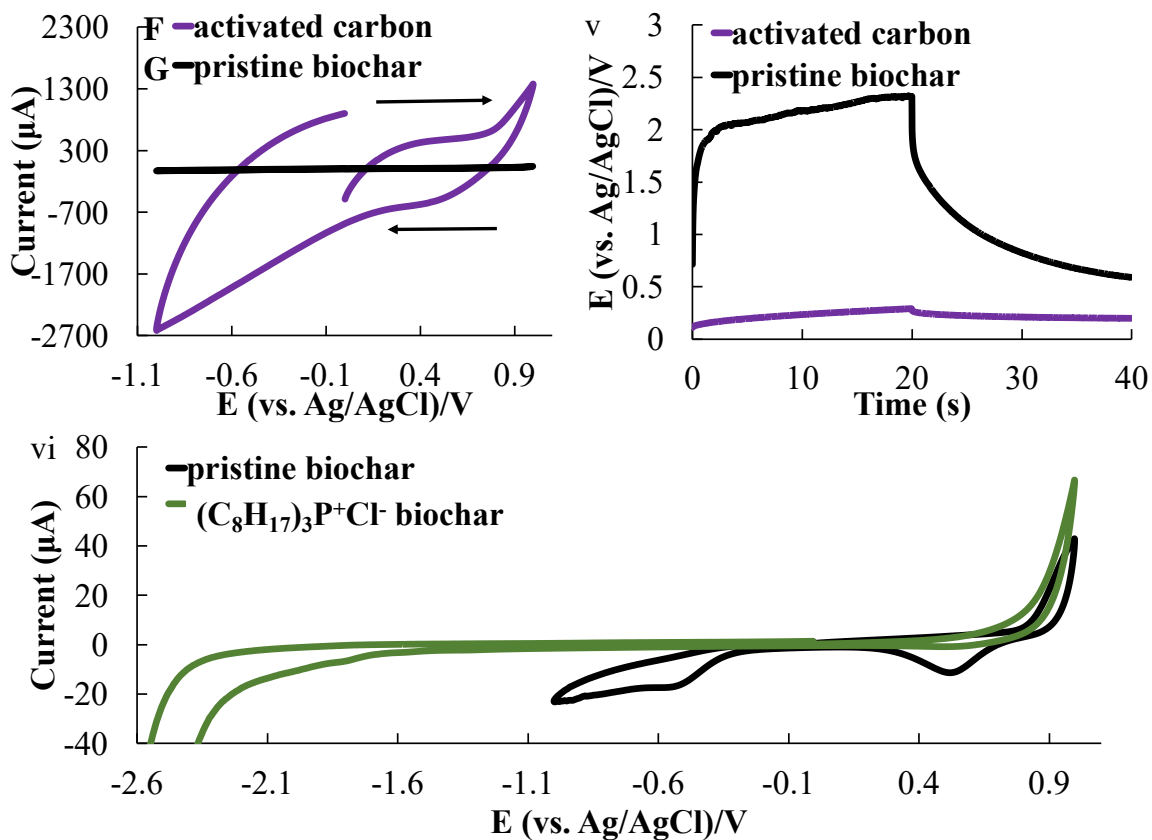


Figure 3.13 Cell I: F, G Cyclic voltammogram with a scan rate of 50 mV/s and GCD measurements (v) of electrode F and G electrodes under the applied current of 150 μ A for each electrode and with an electrolyte system is 1.0 M NaCl. Vi. is the voltammogram of electrode G and A with a scan rate of 50 mV/s in 100 mM Na₂SO₄.

In figure 3.13 F and G, electrode G is pristine biochar mixed with the P_{6,6,6,14}Br binder and gave a potential window of 1.82 V. This is a wider potential window than activated carbon (0.59 V), however, pristine biochar has a noticeably lower capacitance of 10.2 F/g when comparing to activated carbon (29.3 F/g) GCD measurements. The IR drop between 20.0 s and 20.5 s is excluded in determining the capacitance. The significant increase in the potential window of electrode A compared to electrode G can be attributed to the surface of (C₈H₁₇)₃P⁺Cl⁻ biochar. The added cationic functional group

to the surface increases the charge's retention and release based on the applied current. The $(C_8H_{17})_3P^+ Cl^-$ biochar is a resistive but stable material.

3.3 Conclusion

In this study, $(C_8H_{17})_3P^+ Cl^-$ biochar showed greater capacitance than the other $(C_8H_{17})_3P^+ NTf_2^-$ biochar. In Cell I, electrode A had a specific capacitance of 3.52 F/g; in Cell II, the specific capacitance lowered to 1.22 F/g for electrode C in 100 mM Na_2SO_4 . Incorporating a higher surface area material, such as activated carbon, resulted in a higher specific capacitance of 11.0 F/g (electrode E). The effect of functionalization was demonstrated when comparing the capacitance of pristine biochar electrode G, with a specific capacitance of 10.2 F/g. Functionalization in these cases caused the material to have wide electrochemical windows, especially for electrode A, being 2.70 V, showing promise for further work in this area. The future work of this project will consist of decreasing biochar particle size by milling the particles and constructing a device. The device parameters include changing the electrolyte system to an ionic liquid and changing the solvent phase to limit the redox reactions occurring on the electrode surface or in the system. This $(C_8H_{17})_3P^+ Cl^-$ biochar continues to be studied for application as an electrocatalyst for water splitting process.⁹⁵

3.4 Experimental

3.4.1 General materials

Unless stated otherwise, chemicals purchased for experimentation were obtained from Sigma Aldrich, Fisher Scientific and TGI Chemicals were used as received. Pristine

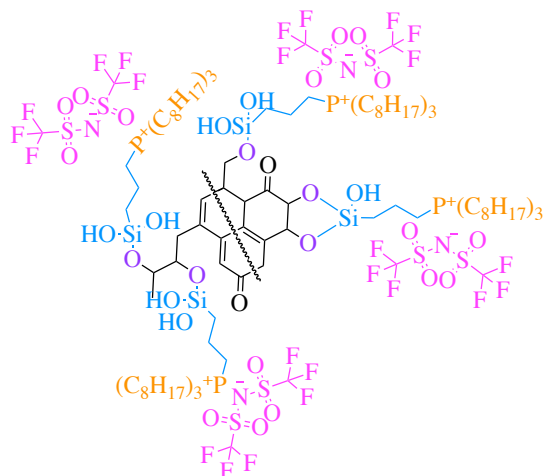
biochar was obtained from Cape Breton University (MacQuarrie research group, Sydney, Nova Scotia) and commercially available solvents unless otherwise stated.

3.4.2 Methods

3.4.3 Synthesis of $(C_8H_{17})_3P^+Cl^-$ biochar

The $(C_8H_{17})_3P^+Cl^-$ biochar used for these electrochemical measurements was by the indirect phosphonium modification of non-exfoliated CPTMS–biochar in **Chapter 2** on pages 66–69.

3.4.4 Synthesis of $(C_8H_{17})_3P^+NTf_2^-$ biochar



Procedure: $(C_8H_{17})_3P^+Cl^-$ biochar (108 mg) is suspended in a 1:1 $H_2O:CH_2Cl_2$. Next, lithium bis(trifluoromethane sulfonyl)imide (119 mg, 0.41 mmol) is left to stir overnight at room temperature. The reaction mixture was filtered and washed with H_2O (2×10.0 mL) and CH_2Cl_2 (2×10.0 mL) to yield a black powdery solid (57.8 mg, 53%). δP (600 MHz, solid, ppm): 32.03 (1 P, s, $R_3R''P^+$), and δF (600 MHz, solid, ppm): --77.81.

3.4.5 Characterization

Functional group analysis

Functional group characterization on phosphonium-modified biochar were observed at 298 K using a Bruker Avance II 600 MHz SSNMR spectrometer, equipped with a SB Bruker 3.2 mm MAS triple-tuned probe operating at 243.00 MHz for ^{31}P and 564.77 MHz for ^{19}F nuclei. The samples were spun at 10 kHz for ^{31}P and 16 kHz ^{19}F . The Cross-polarization (CPMAS) spectra were collected with a Hartmann-Hahn match at 62.5 kHz and 100 kHz ^1H -decoupling, a contact time of 2 ms and a recycling time of 5 s. 1k scans were collected for both ^{31}P and ^{19}F nuclei; and spectra were referenced externally to ASP for ^{31}P .

FT-IR spectra were obtained using a Bruker Alpha FTIR spectrometer. The samples were prepared in KBr with a ratio of 0.2:200 (biochar: KBr) and pressed into pellets. In transmission mode, the spectra were collected from 4000 to 400 cm^{-1} , using 4 cm^{-1} spectra resolution and 24 scans for each collection. The spectra were corrected against pure KBr pellet and data was processed using OPUS data software.

Surface measurements

Scanning electron microscopy (SEM) images of the surfaces of the activated carbon, $(\text{C}_8\text{H}_{17})_3\text{P}^+ \text{Cl}^-$ and $(\text{C}_8\text{H}_{17})_3\text{P}^+ \text{NTf}_2^-$ biochar electrodes were obtained using an FEI Quanta 400 FEG under a high vacuum (10^{-6} torr). The voltage was 25 kV with an electron dispersive X-ray detector (EDX). Transmission electron microscopy (TEM) images were of activated carbon; $(\text{C}_8\text{H}_{17})_3\text{P}^+ \text{Cl}^-$ and $(\text{C}_8\text{H}_{17})_3\text{P}^+ \text{NTf}_2^-$ biochar using a

Hitachi HT7700 Transmission Electron Microscope in high contrast (HC) mode containing a tungsten filament at 80 kV at Cape Breton University.

Brunauer-Emmett-Teller (BET) theory was applied to gas adsorption isotherms determine surface area measurements were obtained using a TriStar II PLUS surface area analyzer from micromeritics using N_2 @ 77K after degassing samples at 110 °C for 6 h.

Powder X-ray diffraction (pXRD) was performed using a Rigaku Ultima IV XRD for 10 °/min from a range of 3–100 °.

Electrochemical measurements

CV and GCD measurements were performed at room temperature on a Wave Now potentiostat (Pine Research Instrumentation). The working electrodes surfaces (GCE: A, B, E, and F; CFP: C and D) were modified and analyzed using a 3-electrode setup with a Pt/C auxiliary electrode and Ag(s)/AgCl in KCl (sat) reference electrode. For CV measurements, a scan rate of 50 mV/s was applied. The GCD measurements were performed by chronopotentiometry in 20 s intervals of charge-discharging with varied current densities. Sample calculations are located in **SI 4**. Each measurement was completed in aqueous electrolyte systems such as 1.0 M NaCl, 100 mM Na_2SO_4 , or 10 mM $LiNTf_2$.

3.4.6 Experimental set-up

Cell I: Teflon cup

A small plastic cup with an insert for a small GCE (5mm OD × 4mm thick glassy carbon, mirror polish) from Pine Research was connected as the working electrode using a folded brass sheet, the GCE was placed into the Teflon cup where the electrode surface was coated and air-dried. The electrolyte solution (23 mL) was added, and a septum was added to the cup. This allowed the insertion of the Ag/AgCl reference electrode and Pt/C auxiliary electrode into the top of the system, and each electrode was connected to the potentiostat for measurements.

Cell I: Preparation of surface-modified glassy carbon working electrodes.

The biochar ink was prepared by suspending a combination of functionalized biochar, pristine biochar and/or activated carbon, and ionic liquid, P_{6,6,6,14}Br or P_{6,6,6,14}NTf₂ (for electrodes A, B, E, or F) in ethyl acetate (1000 μL) and sonicating for 1 h. The ink (20 μL) was then dried onto the GCE for Cell I setup and analysis was completed in 1.0 M NaCl, 100 mM Na₂SO₄ and 10 mM LiNTF₂ electrolyte solution.

Electrode A: A 2:1 (C₈H₁₇)₃P⁺Cl⁻ biochar: P_{6,6,6,14}Br (32.4 mg) suspended in ethyl acetate (1000 μL), sonicate, and 20 μL was dried on the GCE surface (0.65 mg).

Electrode B: A 2:1 mixture of (C₈H₁₇)₃P⁺NTf₂⁻ biochar: P_{6,6,6,14}NTf₂ (33.9 mg) suspended in ethyl acetate (1000 μL), sonicate, and 20 μL was dried on the GCE surface (0.68 mg).

Electrode E: A 1:1:1 mixture of $(C_8H_{17})_3P^+Cl^-$ biochar: activated carbon: $P_{6,6,6,14}Br$ (31.5 mg) suspended in ethyl acetate (1000 μL), sonicate, and 20 μL was dried on the GCE surface (0.63 mg).

Electrode F: A 1:1 mixture of activated carbon: $P_{6,6,6,14}Br$ (22.9 mg) suspended in ethyl acetate (1000 μL), sonicate, and 20 μL was dried on the GCE surface (0.46 mg).

Electrode G: A 1:1 mixture of pristine biochar: $P_{6,6,6,14}Br$ (34.3 mg) suspended in ethyl acetate (2000 μL), sonicate, and 20 μL was then dried on the GCE surface (0.34 mg).

Cell II: H-Cell

A H-Type Sealed Electrochemical Cell (45 mL) was obtained from Dek Research, and used with a HYDRion™ N117 25cm² water electrolysis membrane from Ion Power Inc for optimal air-free conditions. 20.0 mL of electrolyte solutions (100 mM Na_2SO_4 or 10 mM $LiNTf_2$) was added to each side of the H-cell (2 × 20.0 mL). The H-cell was degassed by bubbling N_2 gas through the cell and then attaching the CFP blanks or electrodes C and D using a TiO_2 rod.

Cell II: Preparation of surface-modified carbon fiber paper working electrode.

Biochar ink was prepared by suspending a combination of phosphonium-IL-modified biochar, and ionic liquid (2:1), $P_{6,6,6,14}Br$ or $P_{6,6,6,14}NTf_2$ and these mixtures were sonicated for 1 h. CFP was coated on one side (1 cm × 1 cm) with biochar ink (200 μL) and left to dry overnight. These samples were connected to a TiO_2 rod in cell II set up and analyzed in 100 mM Na_2SO_4 or 10 mM $LiNTF_2$.

Electrode C: A 2:1 $(C_8H_{17})_3P^+Cl^-$ biochar: $P_{6,6,6,14}Br$ (32.4 mg) suspended in ethyl acetate (1000 μL), sonicate, and 200 μL was dried on CFP electrode surface. (6.5 mg)

Electrode D: A 2:1 mixture of $(C_8H_{17})_3P^+ NTf_2^-$ biochar: $P_{6,6,6,14}NTf_2$ (33.9 mg) suspended in ethyl acetate (1000 μ L), sonicate, and 200 μ L was dried on CFP electrode surface (6.8 mg).

Acknowledgements

Judy MacInnis for TEM analysis at Cape Breton University, Dr. Wanda Aylward for SEM data at Memorial University of NL, Rodney Blanchard and Dr. Mike Katz for the BET analysis at Memorial University of NL; and Sachel Christian-Robinson for the pXRD data at Memorial University of NL.

Co-authorship statement:

CHAPTER 4: Molecular speciation of hardwood, crab shell and sugar kelp biochar: solvent extrography using APPI-21T-FT-ICR mass spectrometry.

Sara M. K. Cheema, Amy McKenna, Huan Chen, Martha L. Chacón-Patiño, Francesca M. Kerton, and Stephanie L. MacQuarrie.

Article in preparation to be submitted to *Analytical Chemistry*.

The first author (Sara M. K. Cheema) contributed to data analysis and writing manuscript.

The co-author (Stephanie L. MacQuarrie), my primary supervisor, was responsible for providing samples for analysis and revising the manuscript.

The co-author (Francesca M. Kerton), my co-supervisor, was responsible for revising and submitted manuscript.

The co-author (Huan Chen) was responsible for experimental design and FT-ICR analysis.

The co-author (Martha L. Chacón-Patiño) was responsible for experimental design of the solvent extrography method and FT-ICR analysis.

The corresponding author (Amy McKenna) was the principal investigator of this work and was responsible for the experimental design, FT-ICR analysis, data organization, assisting with data interpretation and revising the manuscript.

Chapter 4: Molecular speciation of hardwood, crab shell and sugar kelp biochar: solvent extrography using APPI-21T-FT-ICR mass spectroscopy

4.1 Introduction

Biochar is produced from the thermal degradation of biomass and is composed of a convoluted mixture of condensed organic compounds such as arenes and/or more polar aromatics such as quinones (or phenolic) and/or pyridinic moieties built onto a carbon base.⁹⁶ Lignocellulosic-derived biochar from hard and softwood materials is well understood and applied as a soil amendment or an adsorbent for the treatment of environmental toxins such as poly-fluoroalkyl substances (PFAS).^{14, 97, 98, 99} In comparison with other biochars, lignocellulosic biochar tends to contain high carbonized fractions, as noted by Bednik et al.¹⁰⁰ This group stated this through the investigation of 6 different feedstocks of biochar from the forestry and agriculture industries and household food waste to compare the elemental composition obtained from the elemental analysis of each.¹⁰⁰ Thus, further investigations are needed to advance the molecular speciation of a well-understood source of biochar (i.e, hardwood biochar) using ultrahigh resolution mass spectrometry such as Fourier Transform Ion Cyclotron Resonance mass spectrometry (FT-ICR-MS). Then compare it to less understood aquatically sourced biochar (i.e, crab shell and sugar kelp) to allow a better understanding of the molecular speciation in biochars. This also has the potential to help optimize functionalized biochar reactions more efficiently to produce functionalized biochar for advanced applications such as heavy metal sorption, catalysis and electrochemical devices.^{101, 50, 102}

In the past decade, there have been a few reports studying biochar materials and their complex molecular differences based on a variety of feedstocks using extraction methods, combined with FT-ICR-MS.^{49, 47, 103} Previous to that, bio-oil, which is also produced by pyrolysis, was heavily studied by petrol industries to gain an understanding of the molecular compositions for applications.¹⁶ The earlier characterization methods used with bio-oil include 2D gas chromatography-mass spectrometry (GC-MS) and pyrolysis-GC-MS.^{104, 105, 106, 107} A recent study of the characterized crab shell biochar using pyrolysis-GC-MS to identify the degradation mechanism of crab shell throughout pyrolysis, was completed by Sebestyén et al.²³ This group identified specific bond cleavage reactions of chitin, such as dehydration, deacetylation and depolymerization reactions based on the retention time and abundance of volatiles at specific temperatures.²³ FT-ICR MS is a remarkable tool for the separation and mass analysis of ionized biochar due to its ultra-high resolution and high mass accuracy. The mass analysis of biochar advanced to FT-ICR-MS, due to the success in identifying the molecular speciation of lipids (bio-oil) produced from pyrolysis.¹⁰⁸

Biochar characterization has limitations when it comes to mass spectrometric methods due to its high polydispersity, complexity, aggregation and low solubility characteristics. These characteristics cause hindrances in the effective separation and the ability to become ionized for mass analysis of biochar components by TOF and FT-ICR.⁴⁹ Therefore, solvent extrography is an extremely impactful method to separate various components of biochar. Solvent extrography methods were originally developed for carbon-based materials such as asphaltenes and coal-tar materials.^{109, 110} Tian et al. characterized biochar components using FT-ICR and solvent extrography with solvents

that increase in polarities such as dichloromethane (CH_2Cl_2), acetone (CH_3COCH_3), methanol (CH_3OH), and distilled water (H_2O).¹¹¹ Each of the solvents selected demonstrated a manageable way to separate compounds based on solid-solvent interactions and stabilizing intermolecular forces.¹¹¹ Their work reports that the greater solvent polarity leads to a higher extraction rate and the most abundant dissolved organic matter (DOM) was in the CH_3OH fraction of soybean biochar. The CH_3OH and H_2O solvents act as nucleophiles to stabilize components through hydrogen bonding of the smaller molecules in oxygen- and nitrogen-containing functional groups. The CH_2Cl_2 stabilized unsaturated aliphatic compounds, CH_3OH and CH_3COCH_3 extracts higher molecular weight compounds in biochar with oxygen-containing functional groups.¹¹¹ Besides, intermolecular forces like hydrogen bonding that provide electron accepting or donating interactions, other solvents such as toluene can lead to stabilizing effects caused by similar polarizabilities.

This report identifies the molecular speciation of hardwood biochar (bc_{hw}), crab shell biochar (bc_{cs}), and sugar kelp biochar (bc_{sk}) that were pyrolyzed at temperatures of 400–515 °C underwent solvent extrography and fractions are characterized using APPI-21 T-FT-ICR tandem mass spectroscopy. The tandem MS consists of a linear ion trap and a 21 T-FT-ICR-MS to separate complex mixtures of ions based on m/z .

Solvent Extrography

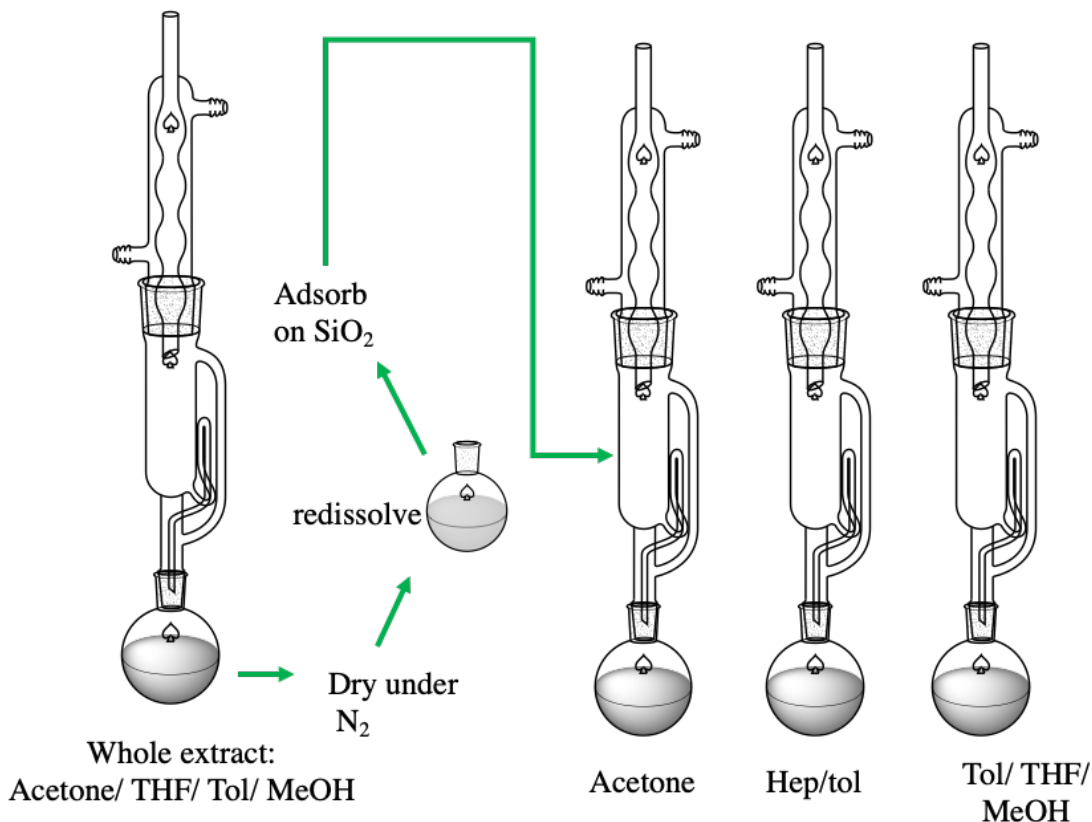


Figure 4.1 Solvent extrography method by fractionation.

The first solvent system used for the extrography is the whole extract (1:1:1:1 CH₃COCH₃/CH₃OH/Tol/ tetrahydrofuran (THF)) fraction that should obtain all extractable components of the materials under analysis. The whole extract is adsorbed onto SiO₂ and is further extracted using solvent systems: CH₃COCH₃, Hep/Tol(1:1) and CH₃OH/Tol/THF (1:1:1) to isolate peri condensed aromatic molecular species.¹¹² The data visualization is completed by double bond equivalents (DBE) to carbon number isoabundant contour plots.

4.2 Discussion

4.2.1 Positive mode APPI identification of aromatic species by solvent extrography

Heteroatom class distribution

The classes of molecules from bc_{hw} , bc_{cs} , and bc_{sk} were identified through solvent extrography by using positive-ion APPI-21 T-FT-ICR MS, this analysis produced a copious amount of data for the wide range of classes (figure 4.2). The most abundant heteroatom class distributions of bc_{hw} , bc_{cs} , and bc_{sk} that are discussed range from hydrocarbon (HC) to phenolic (O_1) to pyrrolic or pyridinic (N_1) classes based on relative abundance. Chacón-Patiño et al. report asphaltene fractionation using the same solvent extrography that facilitates the extraction of aromatic and peri-condensed structures.¹¹² The dipole-dipole interactions of acetone allow the extraction of alkyl-deficient aromatics, and the Hep/Tol fraction isolates the alkyl-aromatic compounds. The Tol/THF/MeOH mixture promotes the extraction of molecules based on hydrogen bonding which should be abundant in polar aromatic species. Tol is also used as a dopant for the transfer of the ionization energy to biochar extracted molecules to form ionized species using APPI.¹¹³ APPI allows for the identification of non-polar species as radical ion and protonated species are stabilized on tertiary sp^3 carbons (C). APPI or ESI paired with FT-ICR allows for the complete identification of polar and non-polar molecular speciation in biochar.

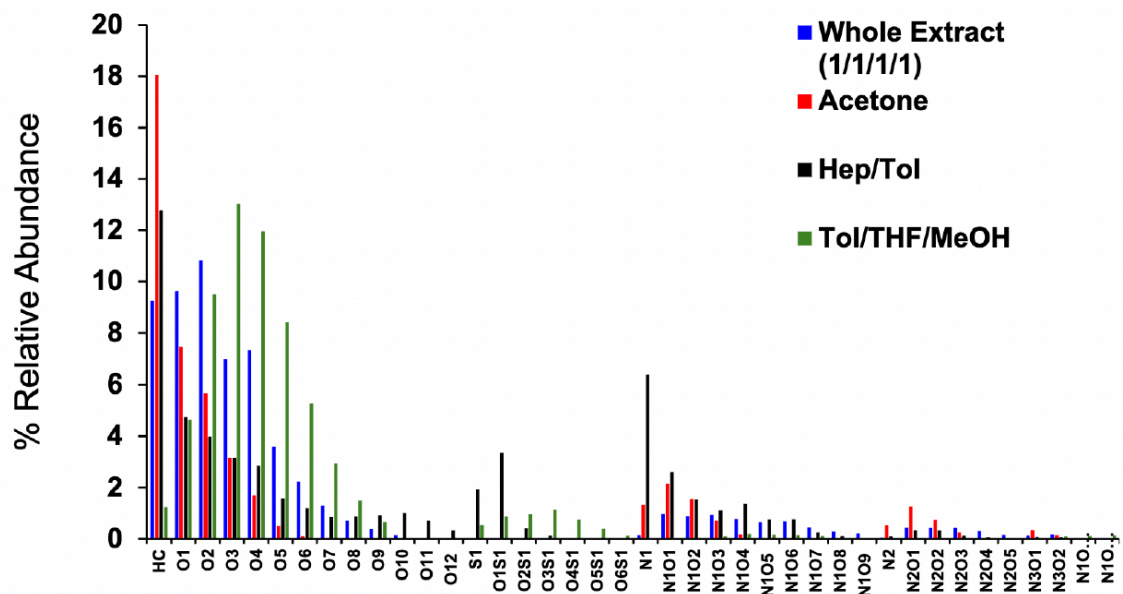


Figure 4.2 Heteroatom class distribution of bc_{hw} for each solvent extraction fraction from the whole extract, acetone, Hep/Tol, Tol/THF/MeOH. This plot and bc_{hw} data were obtained from NHMFL at FSU.

Figures 4.2–4.4 show the relative abundances of the dominant class species of each bc_{hw} , bc_{cs} , and bc_{sk} and its sub-fractions. The spectral complexity and various molecular species containing several heteroatoms and multi-heteroatom-containing compounds, from $O_1 - O_{12}$, $S_1 - O_6S_1$ to N_mO_n , ($m = 0 - 3$, $n = 1 - 9$) were extracted and identified in the solvent extractions. In **Figure 4.2**, the most abundant class of compounds in the bc_{hw} extract is the HC in the acetone fraction. For the O_1 class, the most abundant species is in the whole extract, and the N_1 class the most abundant species based on % R.A. for the bc_{hw} species is in the Hep/Tol fraction.

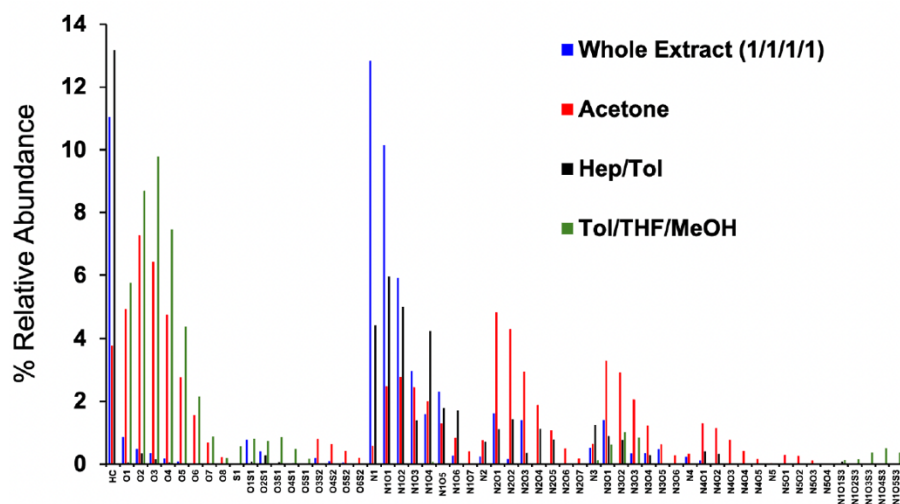


Figure 4.3 Heteroatom class distribution of bc_{cs} for each solvent extraction fraction from the whole extract, acetone, Hep/Tol, Tol/THF/MeOH. This plot and bc_{cs} data were obtained from NHMFL at FSU.

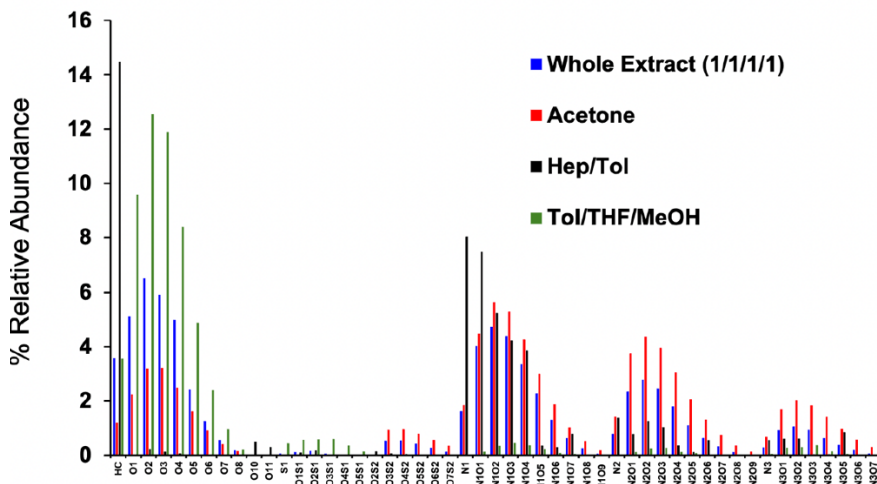


Figure 4.4 Heteroatom class distribution of bc_{sk} for each solvent extraction fraction from the whole extract, acetone, Hep/Tol, Tol/THF/MeOH. This plot and bc_{sk} data were obtained from NHMFL at FSU.

For bc_{cs} in figure 4.3, the highest overall % R. A. of extracted material was the HC and N₁ classes in the Hep/Tol and whole extract, respectively. The O₁ classes have the highest % R. A. extracted species in the Tol/THF/MeOH fraction. Based on these solvents, it is likely that compounds extracted have hydrogen bonding accepting qualities

such as species like 2-pyrenol. For bc_{sk} in figure 4.4, the HC fraction had the highest % R. A. peak was the Hep/Tol fraction. The O_1 class had the highest % R. A. species in the whole extract. The N_1 class had the higher % R. A. in the Hep/Tol fraction.

In the HC, O_1 and N_1 species consisted of both protonated and radical molecular ions, the protonated species are expected to have more aromatic structures and are stabilized by the presence of sp^2 carbons (C), whereas and the radical species are stabilized by less conjugated systems. The O_1 species represent molecular classes such as phenols, ketones, aldehydes, ethers and alcohols. N_1 species represent the pyrolytic 5- and 6-membered rings, as previously reported by Purcell et al., who confirmed this using models of 5 and 6-ring systems of nitrogen-containing aromatics.¹¹⁴ Thus, we see the bc_{sk} and bc_{cs} contain significantly more extracted nitrogen-containing species than bc_{hw} . The increased R. A. of nitrogen-containing species likely is accounted for by the composition of proteins and chitosan in the biomass, causing the influx of nitrogen-containing species in the extracts.

4.2.2 DBE versus carbon number plots for the identification of core structures of hardwood, crab and sugar kelp biochar

The DBE as a function of carbon number was plotted for the HC, N_1 and O_1 classes of bc_{hw} , bc_{cs} , and bc_{sk} using +APPI FT-ICR MS with solvent extrography data. These isoabundant maps allow easy comparison of data based on ionization mode since ionization can incur to identify thousands of molecular formulas in each of the solvent fractions. This allows the visualization of the most abundant core structures within classes of extracted material (i.e, HC, N_1 , and O_1) are shown in colour-coded plots of DBE (double bond equivalents, the number of rings plus double bonds to carbons,

$DBE = C - h/2 + n/2 + 1$) as a function of carbon number plots. Hot spots for the plots are identified by the closeness of the color to red and the most abundant species were found in the HC class, and can be expected to be condensed PAHs. The experimental summaries are found in SI 5, 6, and 7 in the thesis appendix. The following molecular formula are ranked according to the most relative abundant (R. A.) species in the protonated and radical forms.

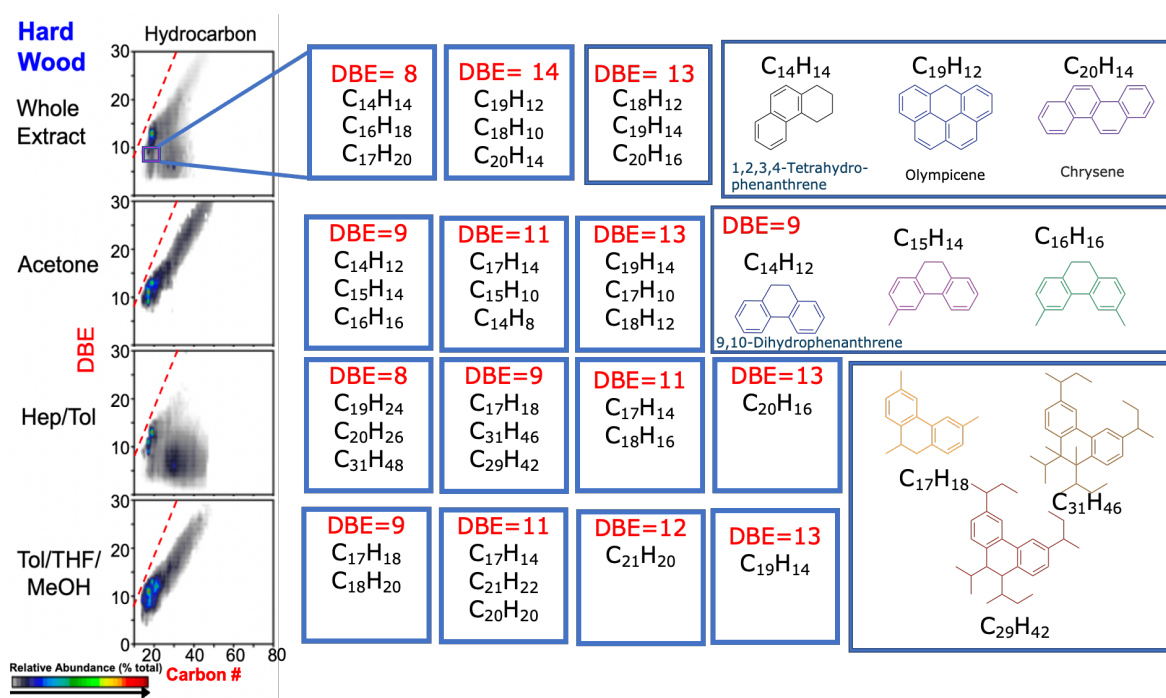


Figure 4.5 Isoabundant maps of DBE as a function of carbon number for HC class species of the whole extract, acetone, Hept/ Tol, Tol/THF/MeOH solvent fractions of bc_{hw} extractions. Plots and data provided by NHMFL at FSU.

In figure 4.5, the hot spots of bc_{hw} from the whole extract have a DBE of 8, 13 and 14. The representative peri-fused condensed structures could be identified as 1, 2, 3, 4-tetrahydrophenanthrene ($C_{14}H_{14}$, 8.4 R. A.), olympicene ($C_{19}H_{12}$, 4.2 R. A.) and chrysene ($C_{20}H_{14}$, 2.4 R.A.). In DBE 8, the most abundant core structures contain C_{14} , C_{16} and C_{17} species, and are ranked based on R.A. These core structures could represent the

same base structure with an added/removed methene group ($-\text{CH}_2-$). The whole extract solvent fraction also contains hotspots at DBE 13 and 14 containing C_{18} to C_{20} hydrocarbon species that differ in $\pm 2\text{H}$. We cannot assume them to be the same compounds with differing degrees of aromaticity as FT-ICR cannot separate structural isomers due to the complexity of data.

The acetone fraction for bc_{hw} (figure 4.5) has hot spots at 9, 11 and 13 DBE. The species identified with DBE of 9 ranged from C_{14} to C_{16} (figure 4.5, row 2), the possible structures are identified by showing the added methyl groups contributing to highest R. A. fractions. The protonated species with a DBE 9 in the acetone fraction can be confirmed to demonstrate added methyl functional groups by reporting molecular species such as $\text{C}_{14}\text{H}_{12}$ (27.0 R. A.), $\text{C}_{15}\text{H}_{14}$ (12.9 R. A.), and $\text{C}_{16}\text{H}_{16}$ (4.38 R. A.). In comparing species with the highest abundance in DBE 11 of $\text{C}_{17}\text{H}_{14}$ to DBE 13 for $\text{C}_{19}\text{H}_{14}$ this can be indicative of another fused ring to the core structure with added degrees of aromaticity on the core structure. In conjunction with this, the molecular species that could be the most abundant in one fraction may not be in another. This is demonstrated in DBE 13 for acetone fraction to the whole extract fraction, where the C_{20} molecular species are not found to be the most abundant. The 11 DBE hydrocarbon species in the acetone fraction are composed of lower molecular weight compounds such as C_{14} and C_{15} hydrocarbons with significantly higher relative abundances to the whole fractions.

The Hep/Tol solvent fractions for the HC class species are specific to aliphatic aromatic species that are not as abundant in the whole extract. This agrees with the fact that Hep is a non-polar aliphatic molecule, thus, will stabilize molecules that contain aliphatic functionality. Comparing this result to the acetone fraction, the Hep/Tol is

selective for condensed HC and aliphatic species due to non-polar properties of heptane and non-polar aromatic properties of toluene and its polarizability. In this fraction, the identification of C₂₉ to C₃₁ species in the lower DBE (8 and 9) hot spots. The 11 DBE hot spot extracted C₁₇ and C₁₈ molecules identified by protonated species while the lower DBE (8 and 9) identified and DBE 13 isolated C₂₀ species. The Tol/THF/MeOH fractions contain several hot spots, including DBE 9, 11, and 13. These contain compounds that are between C₁₇ – C₂₁ (15.2 – 2.90 R. A.) and also contains the highest abundant species in acetone C₁₇H₁₄ that was most abundant. These trends continue in bc_{cs} and bc_{sk}, however, some species are more abundant comparatively.

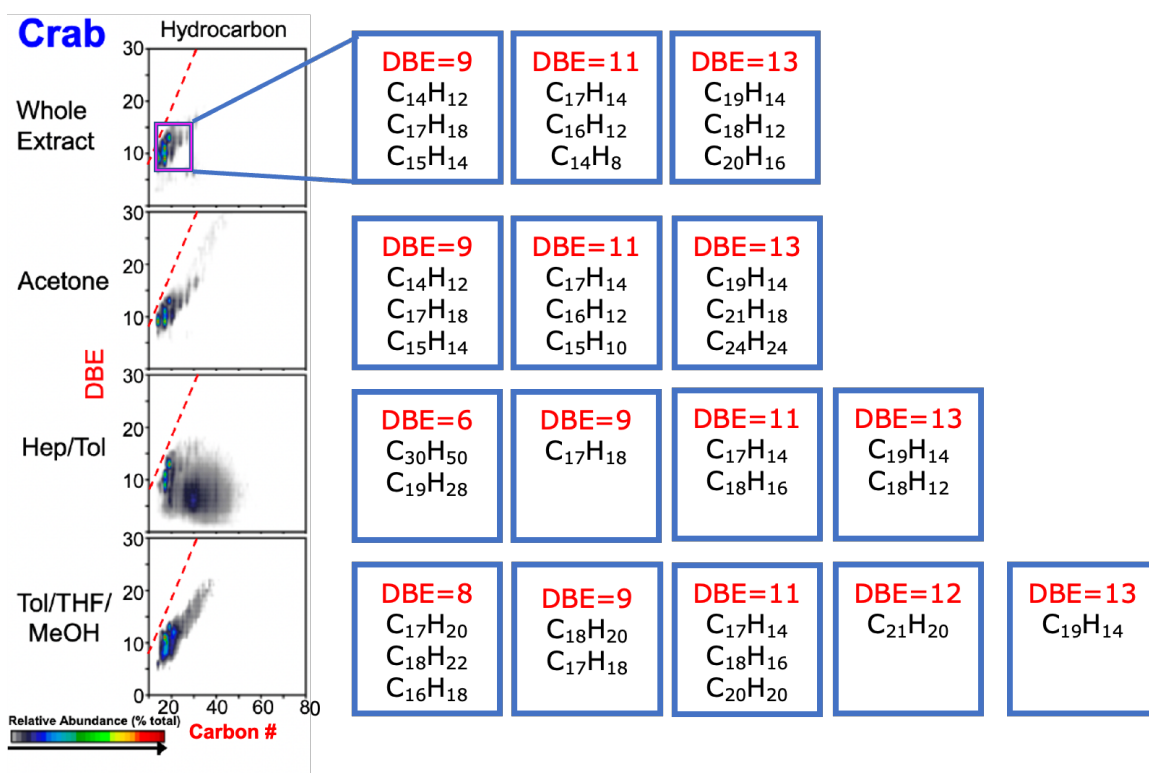


Figure 4.6 Isoabundant maps of DBE as a function of carbon number for HC class species of the whole extract, acetone, Hep/ Tol, Tol/ THF/ MeOH solvent fractions of bc_{cs} extractions. Plots and data provided by NHMFL at FSU.

In figure 4.6, the hot spots of bc_{cs} from the whole extract are found at DBE 9, 11 and 13. There is a range of C_{14} to C_{20} species in the whole extract, $C_{17}H_{14}$ (102 R. A.) and $C_{14}H_{12}$ (94.9 R. A.) are the most abundant protonated HC class species, while $C_{17}H_{18}$ is the most abundant radical species and one of the most abundant for the protonated species. The composition of the bc_{cs} extracts is similar to the composition of bc_{hw} , this demonstrates the solvent specificity for specific molecular species in biochar. The difference of the molecular species for bc_{cs} when looking at the DBE as a function of carbon number plots is the larger variation for DBE for specific carbon numbers. Comparatively, the bc_{hw} molecular species differs compositionally to the bc_{cs} more widely on DBE but overall, the trends are the same.

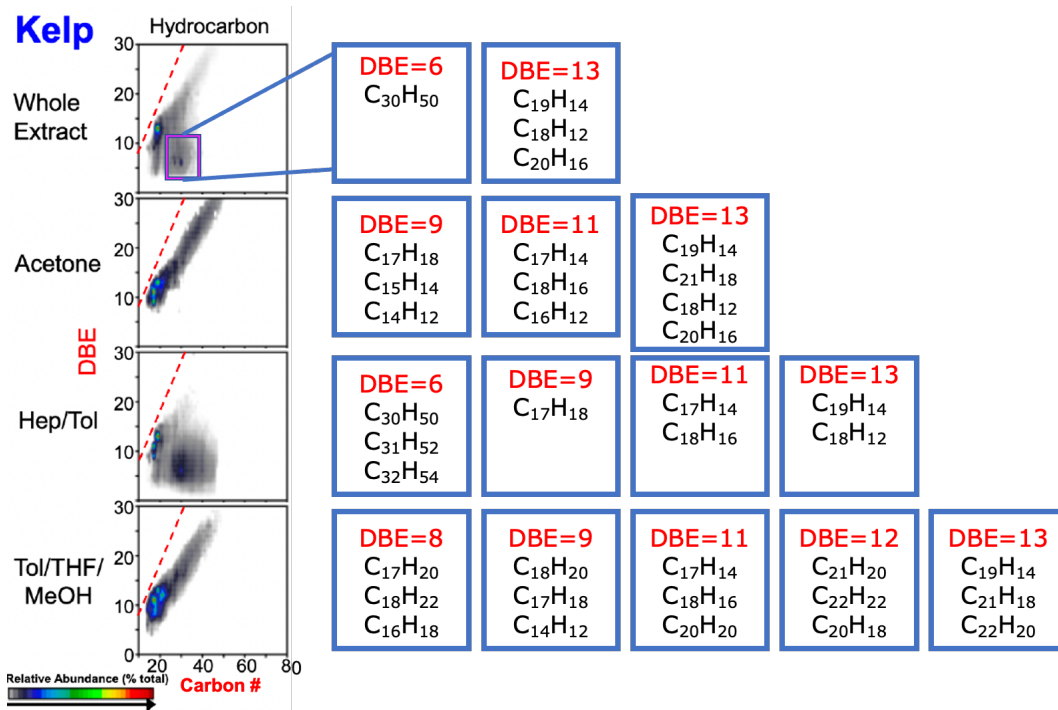


Figure 4.7 Isoabundant maps of DBE as a function of carbon number for HC class species of the whole extract, acetone, Hep/Tol, Tol/THF/MeOH solvent fractions of bc_{sk} extractions. Plots and data provided by NHMFL at FSU.

The bc_{sk} differs from bc_{hw} and bc_{cs} due to the high relative abundance of $C_{30}H_{50}$ (DBE 6) in the whole extract and the Hep/Tol fraction, this could be due to bc_{sk} being produced from fast pyrolysis, while the bc_{hw} and bc_{cs} underwent slow pyrolysis. The comparison of biochar through different preparation methods using FT-ICR has been discussed by Cole et al. to compare switchgrass biochar produced by gasification, slow pyrolysis and fast pyrolysis.¹¹⁵ This group noted that during fast pyrolysis, the vapours produced could condense on the surface of the biochar producing a condensate depending on the isolation method and experimental setup.¹¹⁵ This might explain the low DBE (6) species that are more abundant as the bc_{sk} was the only biochar analyzed produced by fast pyrolysis. Many of the same molecular species are found in the whole extract, acetone Hep/Tol of each species, this is shown in figure 4.7. Overall, the DBE for each of the HC compounds identified in each biochar ranges between 6 – 14 DBE with C_{14} – C_{31} .

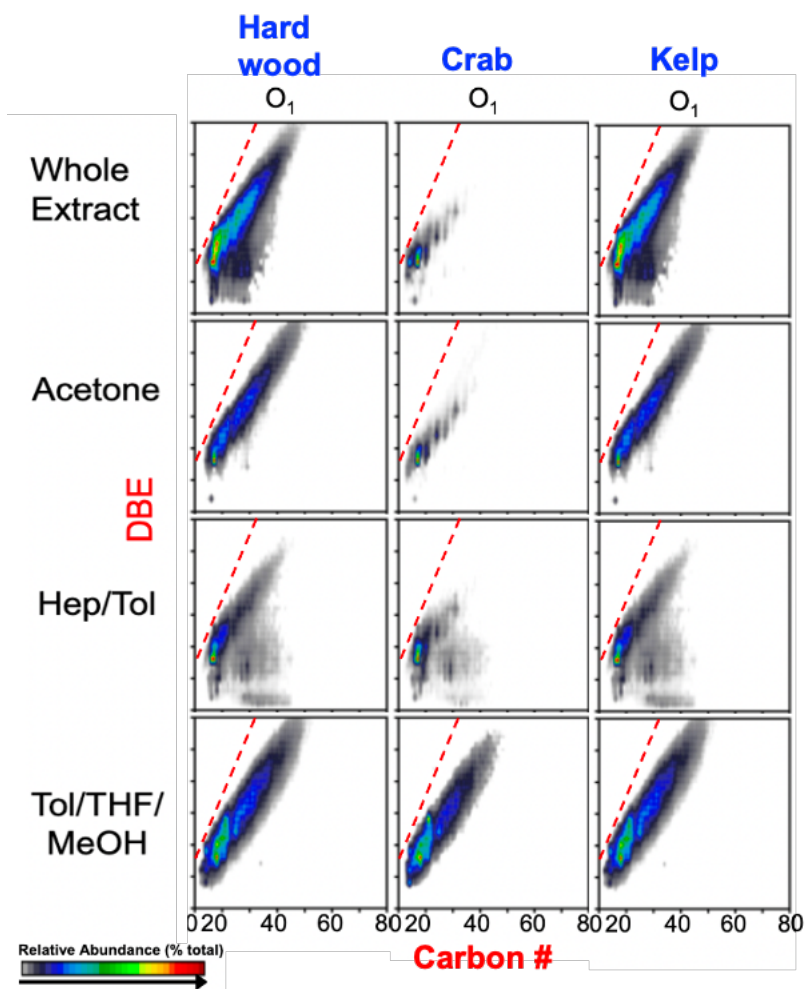


Figure 4.8 Isoabundant maps of DBE as a function of carbon number for O₁ class species of the whole extract, acetone, Hep/Tol, Tol/THF/MeOH solvent fractions of each biochar species. Plots and data provided by NHMFL at FSU.

The isoabundant maps in figure 4.8 show for the whole extract of the bc_{hw} produces two hot spots for O₁ materials around DBE 8 – 9; and another DBE 12. These hotspots can account for C₁₄ and C₁₇ O₁ species for bc_{hw} with DBE of 8 and 9 having high R. A., 74.9 and 21.5, respectively. The hotspot with 12 DBE identifies the molecular species such as C₂₄H₂₀O (7.71 R. A.) and other C₂₁ – C₂₄ compounds in 12 DBE. There is a tail like region from C₂₀ – C₄₀ of very condensed materials, which increase in DBEs with carbon number in a linear pattern. The bc_{cs} follows the same trend with DBE 8 or 9

and identified the same abundant molecular species. The bc_{sk} exhibited all the same compounds but did not present C_{14} molecular species instead presented C_{16} and C_{18} species in the top abundant components extracted and contained hot spots at DBE 8 and 11 as bc_{hw} . The acetone fractions in each biochar have a hot spot of 8 DBE composed of $C_{14} - C_{15}$ molecular species for bc_{hw} , $C_{17} - C_{24}$ for bc_{cs} with a hot spot ranging from DBE 8 to 9 and for bc_{sk} , $C_{17} - C_{24}$, a hot spot at DBE 8 to 11.

Hep/Tol solvent extrography gave a hot spot at 9 DBE for each biochar and suggests that aliphatic compounds identified in HC class of species are the same for each biochar. The Tol/THF/MeOH extraction fractions for the O_1 classes in each biochar had a hot spot at DBE 8 composed of $C_{17}H_{20}O$ as the most abundant for bc_{hw} and this fraction is made up of $C_{16} - C_{18}$. For bc_{cs} , the most abundant species is $C_{18}H_{22}O$ and the fraction is abundant in $C_{16} - C_{20}$ species. For bc_{sk} , the most abundant species is $C_{16}H_{18}O$ and the fraction is abundant in $C_{17} - C_{25}$ oxygen-containing compounds.

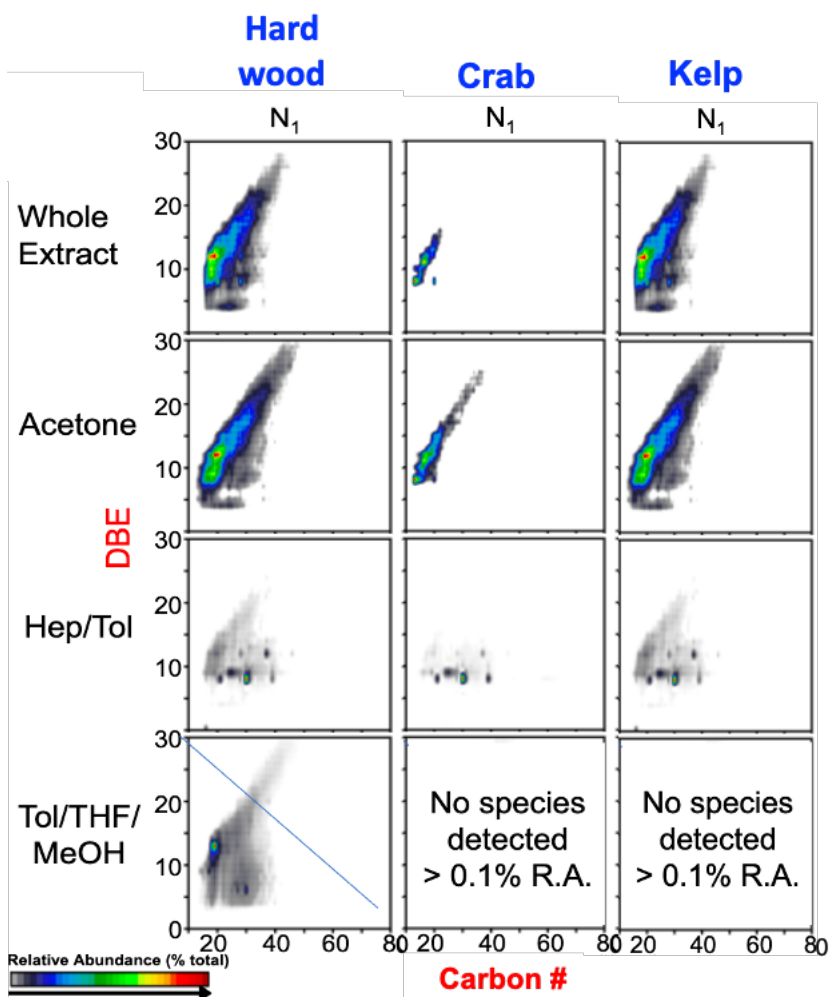


Figure 4.9 Isoabundant maps of DBE as a function of carbon number for N_1 class species of the whole extract, acetone, Hept/ Tol, Tol/ THF/ MeOH solvent fractions of each biochar species. Plots and data provided by NHMFL at FSU.

The hotspot, in **Figure 4.9**, N_1 classes in the whole extract (DBE 12) for bc_{cs} , it contains $C_{16} - C_{18}$ species with DBE of 12 and bc_{sk} follows the same trend. The acetone fraction reveals aromatic structures in the $C_{15} - C_{19}$ range for bc_{hw} , the bc_{cs} extraction results in the identification of $C_{13} - C_{17}$ range of species and bc_{sk} gives a range of species between $C_{19} - C_{22}$ for the N_1 classes. The most abundant species in the Hep/Tol fractions are species that range from $C_{21} - C_{37}$. The most abundant species in bc_{hw} , bc_{cs} , and bc_{sk} is

$C_{30}H_{47}N$ with DBE 8 and R. A. of 100 (bc_{hw}), 103 (bc_{cs}) and 55.7 (bc_{sk}). There is no N_1 species detected in the Tol/THF/MeOH fraction from each biochar.

During visit to Florida State University, attempts were made to analyze phosphonium modified biochar using FT-ICR MS. However, due to the limited time available during the visit, experiments could not be optimized and good quality spectra were not obtained (i.e. poor S/N signals).

4.3 Conclusion

Hardwood, crab shell and sugar kelp biochar have been analyzed using FT-ICR MS to report its differing molecular speciation that is caused by varying pyrolysis temperatures and biomass sources. When biochar is produced by pyrolysis using temperatures below 500 °C, the production of low molecular weight PAHs dominates. Biochar produced above temperatures 500 °C contains more dominant high molecular weight PAHs.¹¹⁶ The biochar investigated in this work are hardwood pyrolyzed at 400 °C (slow pyrolysis), crab shell at 515 °C (slow pyrolysis) and sugar kelp at 450 °C (fast pyrolysis), thus we expect an abundance of lower molecular weight PAHs. PAHs are peri-condensed hydrocarbons that can contaminate the environment.¹¹⁷ The extraction of these lower molecular weight PAHs prior to using biochar in soil amendment or other applications can limit negative environmental impacts.

From the heteroatom distribution graphs (figure 4.2--4.4) the varying fraction heteroatom classes that make up each biochar are showed and they highlight the most dominant species extracted being the HC class from each source. Using the calculation of DBE and analyzing the isoabundant maps allowed for comparison of the most abundant

extracted material. To summarize, the hot spots in the whole extract are consistently the DBE 8, 9 and 13 molecular species, and in the bc_{sk} , the species with DBE of 6 for the HC, O_1 and N_1 classes. The acetone fraction consistently had hot spots of DBE 9, 11, and 13 for the HC fraction for each source and for bc_{hw} the O_1 fraction had 12 DBE, while bc_{cs} O_1 fraction DBE ranges from 8–11. Uniquely, bc_{cs} has a hot spot predominantly at DBE 12 for N_1 class which may result from the more nitrogen-containing nature of the biomass. The Hep/Tol fraction extracts species with DBE 9, 11, and 13 for each source, the HC classes for bc_{cs} and bc_{sk} also isolated an abundance of species with DBE 6. For bc_{hw} and bc_{sk} it also extracted DBE 8 and 10 species for O_1 classes. For bc_{cs} , the most abundant species in the Hep/Tol fraction in the N_1 class had a DBE of 8. For the Tol/THF/MeOH fraction from each source, consistently gave spectra containing species with DBE 9, 11, 12 and 13 in HC, O_1 and N_1 classes. Even though the pyrolysis temperatures and ramp rates are different for the hardwood, crab shell and sugar kelp biochar, there are molecular similarities for the temperature range from 400–515 °C.

4.4 Experimental

4.4.1 Materials

Preparation of hardwood, crab and kelp biochar

All biochar was obtained from Cape Breton University (MacQuarrie research group, Sydney, Nova Scotia). The hardwood biochar was prepared by the anaerobic pyrolysis of debarked birch wood at 400 °C under an inert atmosphere.¹¹⁸ The crab biochar was prepared as follows; Louisbourg Seafoods Ltd provided the crab bodies. The crab was dehydrated and milled to a particle size of approximately 0.5 cm. Pyrolysis was

then performed on dried and milled crab under the conditions of a ramp of 330 °C/hr to a desired temperature of 515 °C and held for a dwell time of 150 minutes in an inert nitrogen atmosphere. The frozen sugar kelp was washed using hot water to remove ice and other surface contaminants and was patted dry; the kelp was cut up into smaller pieces to facilitate consistent drying at 100 °C for 3 h. Samples were rotated every 90 min. The kelp was then ground into a fine powder, pyrolyzed at a ramp rate of 450 °C/hr, and held for a dwell time of 1 hour.

4.4.2 Characterization

21 tesla Fourier transform ion cyclotron resonance mass spectrometry

Data provided for this work was conducted in 2021 with a custom-built 21 Tesla superconducting magnet FT-ICR mass spectrometer at the National High Magnetic Field Laboratory (NHMFL) in Tallahassee, Florida, USA. The excitation ranged from 200--1500 m/z. Ions were produced using APPI positive mode and separated in a 9.4 T ion trap, then the FT-ICR.

4.4.3 Methods

Solvent extrography

Solvent extrography was completed and refined by Martha L. Chacón-Patiño from Florida State University and High Magnetic Field Laboratory, 500 mg of biochar was extracted using a soxhlet extraction using a 1:1:1:1 acetonitrile: toluene: tetrahydrofuran: methanol. The biochar extract is dried under N₂, redissolved into 1:1:1:1 acetonitrile: toluene: tetrahydrofuran: methanol (10.0 mg/mL) and adsorbed on SiO₂ (10 mg sample/g SiO₂). Subsequent extraction using acetone, heptane/toluene,

toluene/tetrahydrofuran/methanol on the whole extracted biochar adsorbed SiO₂ produced 9 extract fractions.

The phosphonium chloride-modified biochar was extracted in 1:1 cyclohexane and acetone via Soxhlet extraction. The biochar extract is dried under N₂, and redissolved in toluene for analysis.

CHAPTER 5: Conclusion and future work

5.1 Ideas for future work

Chapter 1 highlights the principles of green chemistry applied to biochar and the impact of upcycling biomass from industrial waste biomass to biochar. This provided an overview of biochar characteristics based on its preparation, activations, and physical and chemical modifications. However, the completed degradation mechanisms for each source need to be described due to the limitation of information in the literature. Identifying the thermal degradation (and decomplexation) of the vast organic and inorganic materials in biomass could provide a pathway for researchers to obtain ‘designer biochar.’ This could be based on mixing biomass sources to achieve desired surface area, porosity, and functional groups necessary for applications. While also identifying ways to limit energy expenditure and decrease environmental impacts for processes to remain sustainable for producing biochar and tailoring it for applications.

Chapter 2 reports the synthesis and characterization of phosphonium chloride-IL-modified biochar. The quantification results achieved by $^{31}\text{P}\{^1\text{H}\}$ CPMAS SSNMR spectroscopy of each exfoliated and non-exfoliated phosphonium chloride-IL-modified biochar should be confirmed by elemental analysis (EA). EA can be completed at the University of Alberta because of the capability to identify halogens, sulfur and phosphorus-containing compounds. To do this, enough starting material must be made for the direct and indirect synthesis of the phosphonium IL-modified biochar on exfoliated and non-exfoliated biochar for the complete characterization. The siloxane condensation results using TOPPTMS Cl^- on non-exfoliated hydroxylated biochar should

be repeated for reporting; the quantification was affected by contamination with another sample and could not be reported. The surface contact angle measurements should also be completed on each exfoliated and non-exfoliated phosphonium chloride-IL-modified biochar to try to identify a correlation between the degree of phosphonium functionalization and biochar's hydrophobicity.

Chapter 3 reports the synthesis and electrochemical behaviour of indirect synthesis of non-exfoliated phosphonium chloride and bistrifimide-IL-modified biochar. For more confirmation of the phosphonium bistrifimide-IL-modified biochar, a gravimetric titration should be completed using AgNO_3 to precipitate AgCl salt and quantify to the displaced counter ion. This should be further confirmed with ^{19}F and ^{29}Si solid-state NMR spectroscopy, elemental analysis (C, N, O, H, Si, P, Cl, F and S), and surface contact angle measurements to identify hydrophobicity/hydrophilicity.

Overall, the electrochemical behaviour of the phosphonium-IL-modified biochar is highly resistant. Thus, future work will increase the material's conductivity by switching to a higher surface area biochar or adding sustainably derived conductive metals to the biochar frameworks. However, more characterization data, such as gas isotherm adsorption studies, are needed to identify and compare the surface area and pore sizes of the phosphonium salt-IL-modified biochar. The limited SA and large pore size could be contributing to phosphonium salt-IL-modified biochar limited specific capacity by affecting the material's capacitance through electrolyte storage. An interesting result was the high specific capacitance of pristine biochar (10.2 F/g) compared to the phosphonium salt-IL-modified (3.62 F/g) in the cell I, that could be influenced by the lower surface area.

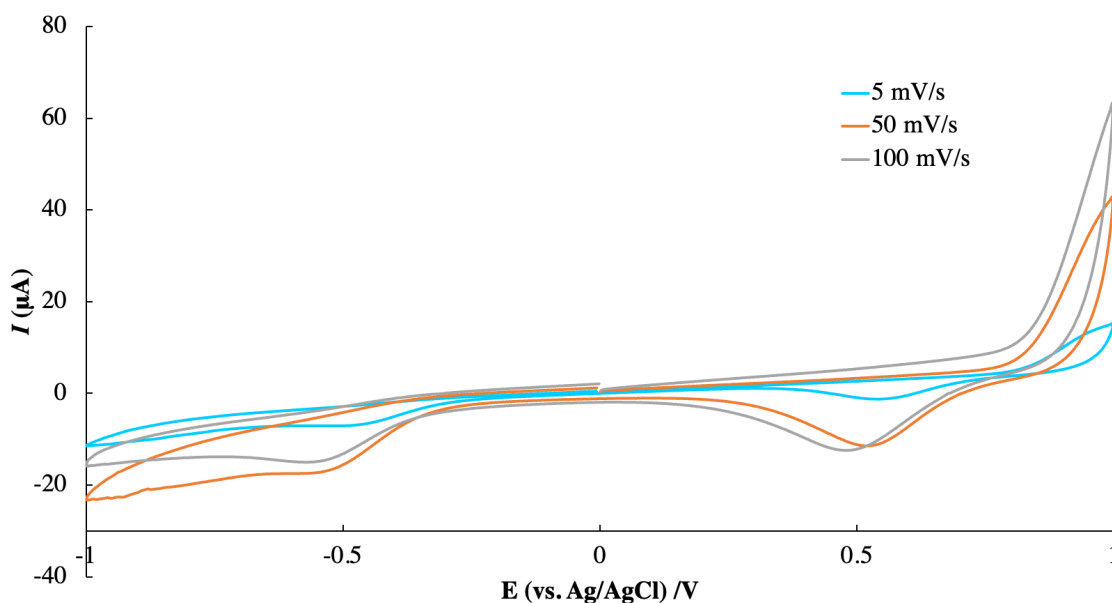


Figure 5.1 The cyclic voltammogram of pristine biochar with P_{6,6,6,10}Br (IL) on a GCE in 100 mM Na₂SO₄.

The electrochemical behaviour of biochar in this thesis was studied with applied scan rates of 50 mV/s; however, Mathias et al. report that a scan rate between 2-5 mV/s can improve the material's capacitance. However, the opposite is shown in figure 5.1. When increasing the scan rate from 5 mV/s to 100 mV/s, a slightly larger current can be extrapolated (Figure 5. 2., gray). Also, due to the workstation being located in a busier part of the lab and the potentiostat being vibration sensitive, the results weren't always run in 5 mV/s or 10 mV/s, so they were excluded.

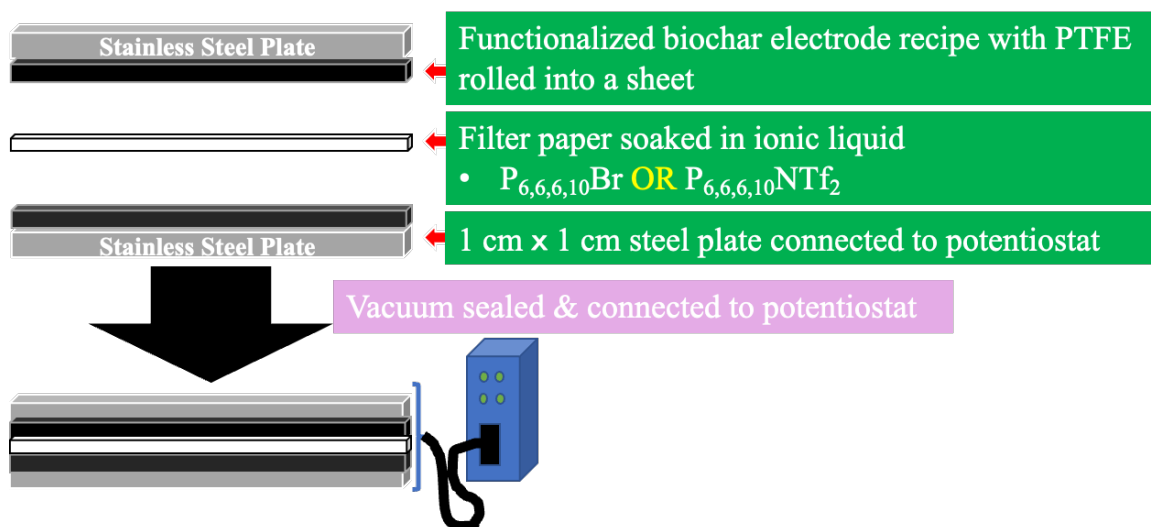


Figure 5.2 Future device-making operation for phosphonium chloride-IL-modified biochar.

Figure 5.2 displays the next step in experimentation for the phosphonium chloride-IL-modified biochar when made into a device. Biochar is first made into a putty mixture using polytetrafluoroethylene (PTFE) and flattened into sheets.⁸⁰ This is completed by stacking biochar sheets between two stainless steel plates connected to the wire that connects the system to the potentiostat. The electrolyte system is a piece of filter paper soaked in ionic liquid with a solid supporting electrolyte mixed in between the two biochar PTFE sheets. This device will be vacuum sealed and electrochemically studied to represent a more realistic cell than the GCE and H-Cell setups.

For Chapter 4, the future work is to analyze functionalized biochar using FT-ICR, this would be the first-ever sample of functionalized biochar characterized by + APPI-FT-ICR to report the phosphonium chloride-IL-modified biochar. During preliminary attempts, a peak was produced at 382.4 m/z, which is 3 orders of magnitude higher signal-to-noise ratio (S/N) than the biochar analyte due to the ionization efficiency and

concentration of the unknown compound. Further experiments were halted due to the risk of long-term contamination in the ion source and front-end mass analyzer. Oxidized hardwood and softwood biochar and sulfonated hardwood biochar were also provided to the Florida State group and still need to be characterized; there were challenges in preparing the sample for ESI due to solubility issues after sonication.

5.2 Conclusions

This thesis shows that hardwood biochar has been functionalized, spectroscopically characterized, electrochemically studied and characterized using APPI-21T- FT-ICR. In Chapter 1 Introduction, the factors that contribute to biochar following the principles of Green Chemistry, a summary of pyrolysis conditions on the carbon base of biochar, applications of hardwood, crab shell and algae biochar composition and application were discussed. Additionally, the most recent reports of modified biochar and how modification enhanced applications were also discussed and the overarching challenge with characterization methods is impacting growth of proving post modification of biochar is briefly discussed. There is also a short discussion on the electrochemical surface interactions that occur with carbon-based materials in the electrochemical application and the desirable characteristics needed. There were also discussions on physical and chemical modification methods and how it influenced biochar application in electrochemistry.

Chapter 2 described the synthesis of phosphonium-IL-modified biochar, the effect of exfoliation through ultrasonication and how it affects the functionalization of hydroxylated biochar and quantification by solid-state NMR spectroscopy. The synthetic steps were completed by indirect and direct grafting methods (condensation reactions);

the indirect synthetic steps were on CPTMS, then TOP and the direct were the preparation of the substituent first, then condensing it onto the surface. The successful incorporation of phosphorus via exfoliated indirect synthesis and; the non-exfoliated and exfoliated direct synthesis were quantified using $^{31}\text{P}\{^1\text{H}\}$ CPMAS solid-state NMR spectroscopy. The phosphonium-IL-modified biochar was further characterized using surface contact angle measurements and electrochemical characterization.

Chapter 3 reports the electrochemical behaviour of two phosphonium salt-IL-modified biochar for use in supercapacitors by identifying the potential window and its specific capacitance. This is characterized by cyclic voltammetry and galvanostatic charge-discharge curves. The phosphonium chloride-IL-modified biochar demonstrated superior performance compared to the phosphonium bistriflimide-IL-modified biochar: a potential window of 2.57 V and specific capacitance of 3.52 F/g were measured. This chapter also summarizes the surface morphology characterization and compares phosphonium salt -IL-modified biochar to activated carbon.

In Chapter 4, the characterization of hardwood, crab and kelp biochars was completed using solvent extrography and positive mode APPI-21T-FT-ICR to identify specificity for organic motifs. The compositional information of the non-polar species present in hardwood, crab and kelp biochars is described.

This thesis is an in-depth overview of newly synthesized phosphonium-IL-modified biochar and new characterization methods for biochar to prove modification.

References

- (1) Anastas, P. T.; Warner, J. C. *Green Chemistry: Theory and Practice*; Oxford University Press: Oxford [England] ; New York, 1998.
- (2) Zhang, Y.; He, M.; Wang, L.; Yan, J.; Ma, B.; Zhu, X.; Ok, Y. S.; Mechtcherine, V.; Tsang, D. C. W. Biochar as Construction Materials for Achieving Carbon Neutrality. *Biochar* **2022**, *4* (1), 59. <https://doi.org/10.1007/s42773-022-00182-x>.
- (3) Hopkins, D. T.; MacQuarrie, S.; Hawboldt, K. A. Removal of Copper from Sulfate Solutions Using Biochar Derived from Crab Processing By-Product. *J. Environ. Manage.* **2022**, *303*, 114270. <https://doi.org/10.1016/j.jenvman.2021.114270>.
- (4) Vijayaraghavan, K. Recent Advancements in Biochar Preparation, Feedstocks, Modification, Characterization and Future Applications. *Environ. Technol. Rev.* **2019**, *8* (1), 47–64. <https://doi.org/10.1080/21622515.2019.1631393>.
- (5) Tan, X.-F.; Zhu, S.-S.; Wang, R.-P.; Chen, Y.-D.; Show, P.-L.; Zhang, F.-F.; Ho, S.-H. Role of Biochar Surface Characteristics in the Adsorption of Aromatic Compounds: Pore Structure and Functional Groups. *Chin. Chem. Lett.* **2021**, *32* (10), 2939–2946. <https://doi.org/10.1016/j.ccllet.2021.04.059>.
- (6) Jamal, M. U.; Fletcher, A. J. Design of Experiments Study on Scottish Wood Biochars and Process Parameter Influence on Final Biochar Characteristics. *BioEnergy Res.* **2023**. <https://doi.org/10.1007/s12155-023-10595-6>.
- (7) Tomczyk, A.; Sokołowska, Z.; Boguta, P. Biochar Physicochemical Properties: Pyrolysis Temperature and Feedstock Kind Effects. *Rev. Environ. Sci. Biotechnol.* **2020**, *19* (1), 191–215. <https://doi.org/10.1007/s11157-020-09523-3>.
- (8) Jamal, M. U.; Fletcher, A. J. *Design of Experiments Optimisation of Scottish Wood Biochars and Process Parameter Significance for Target Applications*; preprint; In Review, 2022. <https://doi.org/10.21203/rs.3.rs-2209948/v1>.
- (9) Ding, W.; Dong, X.; Ime, I. M.; Gao, B.; Ma, L. Q. Pyrolytic Temperatures Impact Lead Sorption Mechanisms by Bagasse Biochars. *Chemosphere* **2014**, *105*, 68–74. <https://doi.org/10.1016/j.chemosphere.2013.12.042>.
- (10) Eisenbarth, S. Do Exports of Renewable Resources Lead to Resource Depletion? Evidence from Fisheries. *J. Environ. Econ. Manag.* **2022**, *112*, 102603. <https://doi.org/10.1016/j.jeem.2021.102603>.
- (11) Abril, G.; Parize, M.; Pérez, M. A. P.; Filizola, N. Wood Decomposition in Amazonian Hydropower Reservoirs: An Additional Source of Greenhouse Gases. *J. South Am. Earth Sci.* **2013**, *44*, 104–107. <https://doi.org/10.1016/j.jsames.2012.11.007>.
- (12) Mosa, A.; Mansour, M. M.; Soliman, E.; El-Ghamry, A.; El Alfy, M.; El Kenawy, A. M. Biochar as a Soil Amendment for Restraining Greenhouse Gases Emission and Improving Soil Carbon Sink: Current Situation and Ways Forward. *Sustainability* **2023**, *15* (2), 1206. <https://doi.org/10.3390/su15021206>.
- (13) Zhang, Y.; Zhang, H.; Zhang, A.; Héroux, P.; Sun, Z.; Liu, Y. Remediation of Atrazine-Polluted Soil Using Dielectric Barrier Discharge Plasma and Biochar

- Sequential Batch Experimental Technology. *Chem. Eng. J.* **2023**, *458*, 141406. <https://doi.org/10.1016/j.cej.2023.141406>.
- (14) Huang, H.; Reddy, N. G.; Huang, X.; Chen, P.; Wang, P.; Zhang, Y.; Huang, Y.; Lin, P.; Garg, A. Effects of Pyrolysis Temperature, Feedstock Type and Compaction on Water Retention of Biochar Amended Soil. *Sci. Rep.* **2021**, *11* (1), 7419. <https://doi.org/10.1038/s41598-021-86701-5>.
- (15) BUTLER, L.; Altdorff, D.; Young, E.; Galagedara, L.; Hawboldt, K.; Helleur, R.; Unc, A. *Organic Waste in Newfoundland and Labrador: A Review of Available Agriculture, Fishery, Forestry and Municipal Waste Literature*; 2016.
- (16) Kuznetsov, B. N.; Sudakova, I. G.; Chudina, A. I.; Garyntseva, N. V.; Kazachenko, A. S.; Skripnikov, A. M.; Malyar, Y. N.; Ivanov, I. P. Fractionation of Birch Wood Biomass into Valuable Chemicals by the Extraction and Catalytic Processes. *Biomass Convers. Biorefinery* **2022**. <https://doi.org/10.1007/s13399-022-02498-x>.
- (17) Kumar, A.; Bhattacharya, T. Biochar for Improvement of Soil Properties. In *Bio-Inspired Land Remediation*; Pandey, V. C., Ed.; Springer International Publishing: Cham, 2023; pp 403–444. https://doi.org/10.1007/978-3-031-04931-6_16.
- (18) Peterson, S. C.; Chandrasekaran, S. R.; Sharma, B. K. Birchwood Biochar as Partial Carbon Black Replacement in Styrene–Butadiene Rubber Composites. *J. Elastomers Plast.* **2016**, *48* (4), 305–316. <https://doi.org/10.1177/0095244315576241>.
- (19) Burke, H. J. Green Chemistry and an Ocean Based Biorefinery Approach for the Valorization of Newfoundland and Labrador Snow Crab (*Chionoecetes Opilio*) Processing Discards, Memorial University of Newfoundland, 2022. <https://research.library.mun.ca/15774/3/converted.pdf>.
- (20) Kerton, F. M.; Yan, N. *Fuels, Chemicals and Materials from the Oceans and Aquatic Sources*; Wiley series in renewable resources; John Wiley & Sons: Chichester, 2017.
- (21) *Canadian Resource Utilization from Aquaculture and the Commercial Fishery*; P-5387; Fisheries and Marine Institute, Memorial University of Newfoundland: Centre for Aquaculture and Seafood Development, 2011.
- (22) Wan Mahari, W. A.; Waiho, K.; Azwar, E.; Fazhan, H.; Peng, W.; Ishak, S. D.; Tabatabaei, M.; Yek, P. N. Y.; Almomani, F.; Aghbashlo, M.; Lam, S. S. A State-of-the-Art Review on Producing Engineered Biochar from Shellfish Waste and Its Application in Aquaculture Wastewater Treatment. *Chemosphere* **2022**, *288*, 132559. <https://doi.org/10.1016/j.chemosphere.2021.132559>.
- (23) Sebestyén, Z.; Jakab, E.; Domán, A.; Bokrossy, P.; Bertóti, I.; Madarász, J.; László, K. Thermal Degradation of Crab Shell Biomass, a Nitrogen-Containing Carbon Precursor. *J. Therm. Anal. Calorim.* **2020**, *142* (1), 301–308. <https://doi.org/10.1007/s10973-020-09438-9>.
- (24) Yan, N.; Chen, X. Sustainability: Don't Waste Seafood Waste. *Nature* **2015**, *524* (7564), 155–157. <https://doi.org/10.1038/524155a>.
- (25) Dai, L.; Zhu, W.; He, L.; Tan, F.; Zhu, N.; Zhou, Q.; He, M.; Hu, G. Calcium-Rich Biochar from Crab Shell: An Unexpected Super Adsorbent for Dye Removal. *Bioresour. Technol.* **2018**, *267*, 510–516. <https://doi.org/10.1016/j.biortech.2018.07.090>.

- (26) Luo, M.; Wang, L.; Li, H.; Bu, Y.; Zhao, Y.; Cai, J. Hierarchical Porous Biochar from Kelp: Insight into Self-Template Effect and Highly Efficient Removal of Methylene Blue from Water. *Bioresour. Technol.* **2023**, *372*, 128676. <https://doi.org/10.1016/j.biortech.2023.128676>.
- (27) Li, L.; Hu, X.; Guo, N.; Chen, S.; Yu, Y.; Yang, C. Synthesis O/S/N Doped Hierarchical Porous Carbons from Kelp via Two-Step Carbonization for High Rate Performance Supercapacitor. *J. Mater. Res. Technol.* **2021**, *15*, 6918–6928. <https://doi.org/10.1016/j.jmrt.2021.11.076>.
- (28) Wang, D.; Dong, S.; Fu, S.; Shen, Y.; Zeng, T.; Yu, W.; Lu, X.; Wang, L.; Song, S.; Ma, J. Catalytic Ozonation for Imazapic Degradation over Kelp-Derived Biochar: Promotional Role of N- and S-Based Active Sites. *Sci. Total Environ.* **2023**, *860*, 160473. <https://doi.org/10.1016/j.scitotenv.2022.160473>.
- (29) Goswami, L.; Kushwaha, A.; Kafle, S. R.; Kim, B.-S. Surface Modification of Biochar for Dye Removal from Wastewater. *Catalysts* **2022**, *12* (8), 817. <https://doi.org/10.3390/catal12080817>.
- (30) Kowalczyk, A.; Zgardzińska, B.; Osipiuk, K.; Jędruchiewicz, K.; Tyszczyk-Rotko, K.; Goździuk, M.; Wang, H.; Czech, B. The Visible-Light-Driven Activity of Biochar-Doped TiO₂ Photocatalysts in β -Blockers Removal from Water. *Materials* **2023**, *16* (3), 1094. <https://doi.org/10.3390/ma16031094>.
- (31) Fan, Q.; Sun, J.; Chu, L.; Cui, L.; Quan, G.; Yan, J.; Hussain, Q.; Iqbal, M. Effects of Chemical Oxidation on Surface Oxygen-Containing Functional Groups and Adsorption Behavior of Biochar. *Chemosphere* **2018**, *207*, 33–40. <https://doi.org/10.1016/j.chemosphere.2018.05.044>.
- (32) Pourhosseini, S. E. M.; Norouzi, O.; Salimi, P.; Naderi, H. R. Synthesis of a Novel Interconnected 3D Pore Network Algal Biochar Constituting Iron Nanoparticles Derived from a Harmful Marine Biomass as High-Performance Asymmetric Supercapacitor Electrodes. *ACS Sustain. Chem. Eng.* **2018**, *6* (4), 4746–4758. <https://doi.org/10.1021/acssuschemeng.7b03871>.
- (33) Bamdad, H.; Hawboldt, K.; MacQuarrie, S. Nitrogen Functionalized Biochar as a Renewable Adsorbent for Efficient CO₂ Removal. *Energy Fuels* **2018**, *32* (11), 11742–11748. <https://doi.org/10.1021/acs.energyfuels.8b03056>.
- (34) Vidal, J. L.; Andrea, V. P.; MacQuarrie, S. L.; Kerton, F. M. Oxidized Biochar as a Simple, Renewable Catalyst for the Production of Cyclic Carbonates from Carbon Dioxide and Epoxides. *ChemCatChem* **2019**, *11* (16), 4089–4095. <https://doi.org/10.1002/cctc.201900290>.
- (35) Shafiee, A.; Karimi Abdolmaleki, M.; Laurencin, Y.; Vela, G. G.; Velazquez, C. A.; Irwin, D. J. G.; Davachi, S. M.; Forbes, C. B.; MacQuarrie, S. Amine-Functionalized Biochar: Highly Re-Useable and Green Alternative for Heparin Recovery from Porcine Intestinal Mucosa. *Sustain. Chem. Pharm.* **2023**, *33*, 101040. <https://doi.org/10.1016/j.scp.2023.101040>.
- (36) Brewer, C. E.; Unger, R.; Schmidt-Rohr, K.; Brown, R. C. Criteria to Select Biochars for Field Studies Based on Biochar Chemical Properties. *BioEnergy Res.* **2011**, *4* (4), 312–323. <https://doi.org/10.1007/s12155-011-9133-7>.

- (37) Zhang, M.; Zhu, H.; Xi, B.; Tian, Y.; Sun, X.; Zhang, H.; Wu, B. Surface Hydrophobic Modification of Biochar by Silane Coupling Agent KH-570. *Processes* **2022**, *10* (2), 301. <https://doi.org/10.3390/pr10020301>.
- (38) Kalinke, C.; De Oliveira, P. R.; Bonacin, J. A.; Janegitz, B. C.; Mangrich, A. S.; Marcolino-Junior, L. H.; Bergamini, M. F. State-of-the-Art and Perspectives in the Use of Biochar for Electrochemical and Electroanalytical Applications. *Green Chem.* **2021**, *23* (15), 5272–5301. <https://doi.org/10.1039/D1GC00843A>.
- (39) Li, X.; Zhang, J.; Liu, B.; Su, Z. A Critical Review on the Application and Recent Developments of Post-Modified Biochar in Supercapacitors. *J. Clean. Prod.* **2021**, *310*, 127428. <https://doi.org/10.1016/j.jclepro.2021.127428>.
- (40) Jisha, M. R.; Hwang, Y. J.; Shin, J. S.; Nahm, K. S.; Prem Kumar, T.; Karthikeyan, K.; Dhanikaivelu, N.; Kalpana, D.; Renganathan, N. G.; Stephan, A. M. Electrochemical Characterization of Supercapacitors Based on Carbons Derived from Coffee Shells. *Mater. Chem. Phys.* **2009**, *115* (1), 33–39. <https://doi.org/10.1016/j.matchemphys.2008.11.010>.
- (41) Zhang, P.; Duan, W.; Peng, H.; Pan, B.; Xing, B. Functional Biochar and Its Balanced Design. *ACS Environ. Au* **2022**, *2* (2), 115–127. <https://doi.org/10.1021/acsenvironau.1c00032>.
- (42) Li, Y.; Li, Z.; Xing, B.; Li, H.; Ma, Z.; Zhang, W.; Reubroycharoen, P.; Wang, S. Green Conversion of Bamboo Chips into High-Performance Phenol Adsorbent and Supercapacitor Electrodes by Simultaneous Activation and Nitrogen Doping. *J. Anal. Appl. Pyrolysis* **2021**, *155*, 105072. <https://doi.org/10.1016/j.jaap.2021.105072>.
- (43) Ding, M.; Ma, Z.; Su, H.; Li, Y.; Yang, K.; Dang, L.; Li, F.; Xue, B. Preparation of Porous Biochar and Its Application in Supercapacitors. *New J. Chem.* **2022**, *46* (45), 21788–21797. <https://doi.org/10.1039/D2NJ03455G>.
- (44) Gao, Y.; Sun, R.; Li, A.; Ji, G. In-Situ Self-Activation Strategy toward Highly Porous Biochar for Supercapacitors: Direct Carbonization of Marine Algae. *J. Electroanal. Chem.* **2021**, *882*, 114986. <https://doi.org/10.1016/j.jelechem.2021.114986>.
- (45) Norouzi, O.; Pourhosseini, S. E. M.; Naderi, H. R.; Di Maria, F.; Dutta, A. Integrated Hybrid Architecture of Metal and Biochar for High Performance Asymmetric Supercapacitors. *Sci. Rep.* **2021**, *11* (1), 5387. <https://doi.org/10.1038/s41598-021-84979-z>.
- (46) Nikolaev, E. N.; Kostyukevich, Y. I.; Vladimirov, G. N. Fourier Transform Ion Cyclotron Resonance (FT ICR) Mass Spectrometry: Theory and Simulations: FT ICR MS. *Mass Spectrom. Rev.* **2016**, *35* (2), 219–258. <https://doi.org/10.1002/mas.21422>.
- (47) Aubriet, F.; Ghislain, T.; Hertzog, J.; Sonnette, A.; Dufour, A.; Mauviel, G.; Carré, V. Characterization of Biomass and Biochar by LDI-FTICRMS – Effect of the Laser Wavelength and Biomass Material. *J. Am. Soc. Mass Spectrom.* **2018**, *29* (10), 1951–1962. <https://doi.org/10.1007/s13361-018-2005-z>.
- (48) Smith, C. R.; Sleighter, R. L.; Hatcher, P. G.; Lee, J. W. Molecular Characterization of Inhibiting Biochar Water-Extractable Substances Using Electrospray Ionization Fourier Transform Ion Cyclotron Resonance Mass Spectrometry. *Environ. Sci. Technol.* **2013**, *47* (23), 13294–13302. <https://doi.org/10.1021/es4034777>.

- (49) McKenna, A. M.; Chacón-Patiño, M. L.; Chen, H.; Blakney, G. T.; Mentink-Vigier, F.; Young, R. B.; Ippolito, J. A.; Borch, T. Expanding the Analytical Window for Biochar Speciation: Molecular Comparison of Solvent Extraction and Water-Soluble Fractions of Biochar by FT-ICR Mass Spectrometry. *Anal. Chem.* **2021**, *93* (46), 15365–15372. <https://doi.org/10.1021/acs.analchem.1c03058>.
- (50) Zhong, Y.; Deng, Q.; Yao, Q.; Lu, C.; Zhang, P.; Li, H.; Wang, J.; Zeng, Z.; Zou, J.-J.; Deng, S. Functionalized Biochar with Superacidity and Hydrophobicity as a Highly Efficient Catalyst in the Synthesis of Renewable High-Density Fuels. *ACS Sustain. Chem. Eng.* **2020**, *8* (21), 7785–7794. <https://doi.org/10.1021/acssuschemeng.9b07367>.
- (51) Mosaffa, E.; Patel, R. I.; Purohit, A. M.; Basak, B. B.; Banerjee, A. Efficient Decontamination of Cationic Dyes from Synthetic Textile Wastewater Using Poly(Acrylic Acid) Composite Containing Amino Functionalized Biochar: A Mechanism Kinetic and Isotherm Study. *J. Polym. Environ.* **2022**. <https://doi.org/10.1007/s10924-022-02744-3>.
- (52) Zhou, X.; Zhou, J.; Liu, Y.; Guo, J.; Ren, J.; Zhou, F. Preparation of Iminodiacetic Acid-Modified Magnetic Biochar by Carbonization, Magnetization and Functional Modification for Cd(II) Removal in Water. *Fuel* **2018**, *233*, 469–479. <https://doi.org/10.1016/j.fuel.2018.06.075>.
- (53) Zhou, Y.; Xiao, J.; Hu, R.; Wang, T.; Shao, X.; Chen, G.; Chen, L.; Tian, X. Engineered Phosphorous-Functionalized Biochar with Enhanced Porosity Using Phytic Acid-Assisted Ball Milling for Efficient and Selective Uptake of Aquatic Uranium. *J. Mol. Liq.* **2020**, *303*, 112659. <https://doi.org/10.1016/j.molliq.2020.112659>.
- (54) Ayiania, M.; Smith, M.; Hensley, A. J. R.; Scudiero, L.; McEwen, J.-S.; Garcia-Perez, M. Deconvoluting the XPS Spectra for Nitrogen-Doped Chars: An Analysis from First Principles. *Carbon* **2020**, *162*, 528–544. <https://doi.org/10.1016/j.carbon.2020.02.065>.
- (55) Xie, J.; Liu, M.; He, M.; Liu, Y.; Li, J.; Yu, F.; Lv, Y.; Lin, C.; Ye, X. Ultra-Efficient Adsorption of Diclofenac Sodium on Fish-Scale Biochar Functionalized with H₃PO₄ via Synergistic Mechanisms. *Environ. Pollut.* **2023**, *322*, 121226. <https://doi.org/10.1016/j.envpol.2023.121226>.
- (56) Vidal, J. L.; Gallant, S. M. V.; Connors, E. P.; Richards, D. D.; MacQuarrie, S. L.; Kerton, F. M. Green Solvents for the Liquid-Phase Exfoliation of Biochars. *ACS Sustain. Chem. Eng.* **2021**, *9* (27), 9114–9125. <https://doi.org/10.1021/acssuschemeng.1c02823>.
- (57) Hummers, W. S. Jr.; Offeman, R. E. Preparation of Graphitic Oxide. *J. Am. Chem. Soc.* **1958**, *80* (6), 1339–1339. <https://doi.org/10.1021/ja01539a017>.
- (58) Chen, J.; Yao, B.; Li, C.; Shi, G. An Improved Hummers Method for Eco-Friendly Synthesis of Graphene Oxide. *Carbon* **2013**, *64*, 225–229. <https://doi.org/10.1016/j.carbon.2013.07.055>.
- (59) Bonanomi, G.; Incerti, G.; Cesarano, G.; Gaglione, S. A.; Lanzotti, V. Cigarette Butt Decomposition and Associated Chemical Changes Assessed by ¹³C CPMAS NMR. *PLOS ONE* **2015**, *10* (1), e0117393. <https://doi.org/10.1371/journal.pone.0117393>.

- (60) Wiench, J. W.; Avadhut, Y. S.; Maity, N.; Bhaduri, S.; Lahiri, G. K.; Pruski, M.; Ganapathy, S. Characterization of Covalent Linkages in Organically Functionalized MCM-41 Mesoporous Materials by Solid-State NMR and Theoretical Calculations. *J. Phys. Chem. B* **2007**, *111* (15), 3877–3885. <https://doi.org/10.1021/jp067417x>.
- (61) Image J. Js. <https://ij.imjoy.io/>.
- (62) Zhu, J. M.; Xin, F.; Sun, Y. C.; Dong, X. C. Phosphonium-Based Ionic Liquids Grafted onto Silica for CO₂ Sorption. *Theor. Found. Chem. Eng.* **2014**, *48* (6), 787–792. <https://doi.org/10.1134/S0040579514060141>.
- (63) Ghosh, S.; Santhosh, R.; Jeniffer, S.; Raghavan, V.; Jacob, G.; Nanaji, K.; Kollu, P.; Jeong, S. K.; Grace, A. N. Natural Biomass Derived Hard Carbon and Activated Carbons as Electrochemical Supercapacitor Electrodes. *Sci. Rep.* **2019**, *9* (1), 16315. <https://doi.org/10.1038/s41598-019-52006-x>.
- (64) Ding, Y.; Wang, T.; Dong, D.; Zhang, Y. Using Biochar and Coal as the Electrode Material for Supercapacitor Applications. *Front. Energy Res.* **2020**, *7*, 159. <https://doi.org/10.3389/fenrg.2019.00159>.
- (65) Berrabah, S. E.; Benchettara, A.; Smaili, F.; Benchettara, A.; Mahieddine, A. High Performance Hybrid Supercapacitor Based on Electrochemical Deposited of Nickel Hydroxide on Zinc Oxide Supported by Graphite Electrode. *J. Alloys Compd.* **2023**, *942*, 169112. <https://doi.org/10.1016/j.jallcom.2023.169112>.
- (66) Lu, Z.; Liu, X.; Wang, T.; Huang, X.; Dou, J.; Wu, D.; Yu, J.; Wu, S.; Chen, X. S/N-Codoped Carbon Nanotubes and Reduced Graphene Oxide Aerogel Based Supercapacitors Working in a Wide Temperature Range. *J. Colloid Interface Sci.* **2023**, *638*, 709–718. <https://doi.org/10.1016/j.jcis.2023.02.013>.
- (67) Gabhi, R. S.; Kirk, D. W.; Jia, C. Q. Preliminary Investigation of Electrical Conductivity of Monolithic Biochar. *Carbon* **2017**, *116*, 435–442. <https://doi.org/10.1016/j.carbon.2017.01.069>.
- (68) Kane, S.; Ulrich, R.; Harrington, A.; Stadie, N. P.; Ryan, C. Physical and Chemical Mechanisms That Influence the Electrical Conductivity of Lignin-Derived Biochar. *Carbon Trends* **2021**, *5*, 100088. <https://doi.org/10.1016/j.cartre.2021.100088>.
- (69) Gabhi, R.; Basile, L.; Kirk, D. W.; Giorcelli, M.; Tagliaferro, A.; Jia, C. Q. Electrical Conductivity of Wood Biochar Monoliths and Its Dependence on Pyrolysis Temperature. *Biochar* **2020**, *2* (3), 369–378. <https://doi.org/10.1007/s42773-020-00056-0>.
- (70) Liang, X.; Liu, R.; Wu, X. Biomass Waste Derived Functionalized Hierarchical Porous Carbon with High Gravimetric and Volumetric Capacitances for Supercapacitors. *Microporous Mesoporous Mater.* **2021**, *310*, 110659. <https://doi.org/10.1016/j.micromeso.2020.110659>.
- (71) Alhashimi, H. A.; Aktas, C. B. Life Cycle Environmental and Economic Performance of Biochar Compared with Activated Carbon: A Meta-Analysis. *Resour. Conserv. Recycl.* **2017**, *118*, 13–26. <https://doi.org/10.1016/j.resconrec.2016.11.016>.
- (72) Zhang, W.; Zou, Y.; Yu, C.; Zhong, W. Nitrogen-Enriched Compact Biochar-Based Electrode Materials for Supercapacitors with Ultrahigh Volumetric Performance. *J. Power Sources* **2019**, *439*, 227067. <https://doi.org/10.1016/j.jpowsour.2019.227067>.

- (73) Armand, M.; Endres, F.; MacFarlane, D. R.; Ohno, H.; Scrosati, B. Ionic-Liquid Materials for the Electrochemical Challenges of the Future. *Nat. Mater.* **2009**, *8* (8), 621–629. <https://doi.org/10.1038/nmat2448>.
- (74) Sánchez-Ramírez, N.; Monje, I. E.; Bélanger, D.; Camargo, P. H. C.; Torresi, R. M. High Rate and Long-Term Cycling of Silicon Anodes with Phosphonium-Based Ionic Liquids as Electrolytes for Lithium-Ion Batteries. *Electrochimica Acta* **2023**, *439*, 141680. <https://doi.org/10.1016/j.electacta.2022.141680>.
- (75) Shabeeba, P.; Thasneema, K. K.; Thayyil, M. S.; Pillai, M. P.; Niveditha, C. V. A Graphene-Based Flexible Supercapacitor Using Trihexyl(Tetradecyl)Phosphonium Bis(Trifluoromethanesulfonyl)Imide Ionic Liquid Electrolyte. *Mater. Res. Express* **2017**, *4* (8), 085501. <https://doi.org/10.1088/2053-1591/aa7b14>.
- (76) Latham, K. G.; Forghani, M.; Dose, W. M.; Allen, J. A.; Donne, S. W. Influence of Counter Ions of Ammonium for Nitrogen Doping and Carbon Properties in Hydrothermal Carbonization: Characterization and Supercapacitor Performance. *Mater. Adv.* **2021**, *2* (1), 384–397. <https://doi.org/10.1039/D0MA00601G>.
- (77) Liu, H.; Liu, Y.; Li, J. Ionic Liquids in Surface Electrochemistry. *Phys. Chem. Chem. Phys.* **2010**, *12* (8), 1685. <https://doi.org/10.1039/b921469k>.
- (78) Chen, M.; White, B. T.; Kasprzak, C. R.; Long, T. E. Advances in Phosphonium-Based Ionic Liquids and Poly(Ionic Liquid)s as Conductive Materials. *Eur. Polym. J.* **2018**, *108*, 28–37. <https://doi.org/10.1016/j.eurpolymj.2018.08.015>.
- (79) Philippi, F.; Rauber, D.; Zapp, J.; Hempelmann, R. Transport Properties and Ionicity of Phosphonium Ionic Liquids. *Phys. Chem. Chem. Phys.* **2017**, *19* (34), 23015–23023. <https://doi.org/10.1039/C7CP04552B>.
- (80) Yiğit, D.; Aykan, M.; Güllü, M. Substituent Effect on Supercapacitive Performances of Conducting Polymer-Based Redox Electrodes: Poly(3',4'-Bis(Alkyloxy) 2,2':5',2''-Terthiophene) Derivatives. *J. Polym. Sci. Part Polym. Chem.* **2018**, *56* (5), 480–495. <https://doi.org/10.1002/pola.28927>.
- (81) Mathis, T. S.; Kurra, N.; Wang, X.; Pinto, D.; Simon, P.; Gogotsi, Y. Energy Storage Data Reporting in Perspective—Guidelines for Interpreting the Performance of Electrochemical Energy Storage Systems. *Adv. Energy Mater.* **2019**, *9* (39), 1902007. <https://doi.org/10.1002/aenm.201902007>.
- (82) Elgrishi, N.; Rountree, K. J.; McCarthy, B. D.; Rountree, E. S.; Eisenhart, T. T.; Dempsey, J. L. A Practical Beginner's Guide to Cyclic Voltammetry. *J. Chem. Educ.* **2018**, *95* (2), 197–206. <https://doi.org/10.1021/acs.jchemed.7b00361>.
- (83) Zhai, Z.; Zhang, L.; Du, T.; Ren, B.; Xu, Y.; Wang, S.; Miao, J.; Liu, Z. A Review of Carbon Materials for Supercapacitors. *Mater. Des.* **2022**, *221*, 111017. <https://doi.org/10.1016/j.matdes.2022.111017>.
- (84) Lyu, H.; Yu, Z.; Gao, B.; He, F.; Huang, J.; Tang, J.; Shen, B. Ball-Milled Biochar for Alternative Carbon Electrode. *Environ. Sci. Pollut. Res.* **2019**, *26* (14), 14693–14702. <https://doi.org/10.1007/s11356-019-04899-4>.
- (85) Stephanie, H.; Mlsna, T. E.; Wipf, D. O. Functionalized Biochar Electrodes for Asymmetrical Capacitive Deionization. *Desalination* **2021**, *516*, 115240. <https://doi.org/10.1016/j.desal.2021.115240>.
- (86) Dou, Q.; Liu, L.; Yang, B.; Lang, J.; Yan, X. Silica-Grafted Ionic Liquids for Revealing the Respective Charging Behaviors of Cations and Anions in

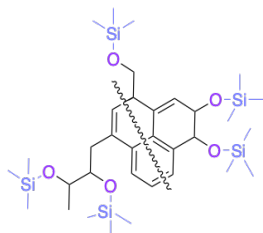
- Supercapacitors. *Nat. Commun.* **2017**, *8* (1), 2188. <https://doi.org/10.1038/s41467-017-02152-5>.
- (87) Bhatt, A. I.; May, I.; Volkovich, V. A.; Hetherington, M. E.; Lewin, B.; Thied, R. C.; Ertok, N. Group 15 Quaternary Alkyl Bistriflimides: Ionic Liquids with Potential Application in Electropositive Metal Deposition and as Supporting Electrolytes. *J. Chem. Soc. Dalton Trans.* **2002**, No. 24, 4532–4534. <https://doi.org/10.1039/b208968h>.
- (88) Wei, Y.; Liu, H.; Jin, Y.; Cai, K.; Li, H.; Liu, Y.; Kang, Z.; Zhang, Q. Carbon Nanoparticle Ionic Liquid Functionalized Activated Carbon Hybrid Electrode for Efficiency Enhancement in Supercapacitors. *New J. Chem.* **2013**, *37* (4), 886. <https://doi.org/10.1039/c3nj41151f>.
- (89) Ghorbani, M.; Simone, M. I. Developing New Inexpensive Room-Temperature Ionic Liquids with High Thermal Stability and a Greener Synthetic Profile. *ACS Omega* **2020**, *5* (22), 12637–12648. <https://doi.org/10.1021/acsomega.9b04091>.
- (90) Kim, P.; Johnson, A.; Edmunds, C. W.; Radosevich, M.; Vogt, F.; Rials, T. G.; Labbé, N. Surface Functionality and Carbon Structures in Lignocellulosic-Derived Biochars Produced by Fast Pyrolysis. *Energy Fuels* **2011**, *25* (10), 4693–4703. <https://doi.org/10.1021/ef200915s>.
- (91) Yea, Y.; Kim, G.; Wang, D.; Kim, S.; Yoon, Y.; Elanchezhian, S. Sd.; Park, C. M. Selective Sequestration of Perfluorinated Compounds Using Polyaniline Decorated Activated Biochar. *Chem. Eng. J.* **2022**, *430*, 132837. <https://doi.org/10.1016/j.cej.2021.132837>.
- (92) Yang, K.; Cho, K.; Kim, S. Effect of Carbon Black Addition on Thermal Stability and Capacitive Performances of Supercapacitors. *Sci. Rep.* **2018**, *8* (1), 11989. <https://doi.org/10.1038/s41598-018-30507-5>.
- (93) Ma, Z.-W.; Liu, H.-Q.; Lü, Q.-F. Porous Biochar Derived from Tea Saponin for Supercapacitor Electrode: Effect of Preparation Technique. *J. Energy Storage* **2021**, *40*, 102773. <https://doi.org/10.1016/j.est.2021.102773>.
- (94) Li, Y.; Zhu, L.; Shi, J.; Dou, Y.; Li, S.; You, R.; Zhang, S.; Miao, X.; Shi, S.; Ji, H.; Yang, G. Super-Hydrophilic Microporous Biochar from Biowaste for Supercapacitor Application. *Appl. Surf. Sci.* **2021**, *561*, 150076. <https://doi.org/10.1016/j.apsusc.2021.150076>.
- (95) Yu, H.-Z.; Bencherif, S.; Pham-Truong, T.-N.; Ghilane, J. Immobilization of Molecule-Based Ionic Liquids: A Promising Approach to Improve Electrocatalyst Performance towards the Hydrogen Evolution Reaction. *New J. Chem.* **2022**, *46* (2), 454–464. <https://doi.org/10.1039/D1NJ04400A>.
- (96) Chen, G.; Zhang, Z.; Zhang, Z.; Zhang, R. Redox-Active Reactions in Denitrification Provided by Biochars Pyrolyzed at Different Temperatures. *Sci. Total Environ.* **2018**, *615*, 1547–1556. <https://doi.org/10.1016/j.scitotenv.2017.09.125>.
- (97) Podgorski, D. C.; Hamdan, R.; McKenna, A. M.; Nyadong, L.; Rodgers, R. P.; Marshall, A. G.; Cooper, W. T. Characterization of Pyrogenic Black Carbon by Desorption Atmospheric Pressure Photoionization Fourier Transform Ion Cyclotron Resonance Mass Spectrometry. *Anal. Chem.* **2012**, *84* (3), 1281–1287. <https://doi.org/10.1021/ac202166x>.

- (98) Jiang, S.; Huang, L.; Nguyen, T. A. H.; Ok, Y. S.; Rudolph, V.; Yang, H.; Zhang, D. Copper and Zinc Adsorption by Softwood and Hardwood Biochars under Elevated Sulphate-Induced Salinity and Acidic PH Conditions. *Chemosphere* **2016**, *142*, 64–71. <https://doi.org/10.1016/j.chemosphere.2015.06.079>.
- (99) Zhang, Y.; Tan, X.; Lu, R.; Tang, Y.; Qie, H.; Huang, Z.; Zhao, J.; Cui, J.; Yang, W.; Lin, A. Enhanced Removal of Polyfluoroalkyl Substances by Simple Modified Biochar: Adsorption Performance and Theoretical Calculation. *ACS EST Water* **2023**, *3* (3), 817–826. <https://doi.org/10.1021/acsestwater.2c00597>.
- (100) Bednik, M.; Medyńska-Juraszek, A.; Ćwieląg-Piasecka, I. Effect of Six Different Feedstocks on Biochar's Properties and Expected Stability. *Agronomy* **2022**, *12* (7), 1525. <https://doi.org/10.3390/agronomy12071525>.
- (101) Bacirhonde, P. M.; Dzade, N. Y.; Eya, H. I.; Kim, C. S.; Park, C. H. A Potential Peanut Shell Feedstock Pyrolyzed Biochar and Iron-Modified Peanut Shell Biochars for Heavy Metal Fixation in Acid Mine Drainage. *ACS Earth Space Chem.* **2022**, *6* (11), 2651–2665. <https://doi.org/10.1021/acsearthspacechem.2c00185>.
- (102) Rahman, M. Z.; Edvinsson, T.; Kwong, P. Biochar for Electrochemical Applications. *Curr. Opin. Green Sustain. Chem.* **2020**, *23*, 25–30. <https://doi.org/10.1016/j.cogsc.2020.04.007>.
- (103) Li, S.; Xu, C.; Qin, S.; Guo, X.; Bai, Y.; Guo, F. Molecular Characteristics of Biochar-Derived Organic Matter Sub-Fractions Extracted by Ultrasonication. *Sci. Total Environ.* **2022**, *806*, 150190. <https://doi.org/10.1016/j.scitotenv.2021.150190>.
- (104) Salami, A.; Vilppo, T.; Pitkänen, S.; Weisell, J.; Raninen, K.; Vepsäläinen, J.; Lappalainen, R. Cost-Effective FTIR and ¹H NMR Spectrometry Used to Screen Valuable Molecules Extracted from Selected West African Trees by a Sustainable Biochar Process. *Sci. Afr.* **2020**, *8*, e00315. <https://doi.org/10.1016/j.sciaf.2020.e00315>.
- (105) Mahinpey, N.; Murugan, P.; Mani, T.; Raina, R. Analysis of Bio-Oil, Biogas, and Biochar from Pressurized Pyrolysis of Wheat Straw Using a Tubular Reactor. *Energy Fuels* **2009**, *23* (5), 2736–2742. <https://doi.org/10.1021/ef8010959>.
- (106) Russell, S. H.; Turrion-Gomez, J. L.; Meredith, W.; Langston, P.; Snape, C. E. Increased Charcoal Yield and Production of Lighter Oils from the Slow Pyrolysis of Biomass. *J. Anal. Appl. Pyrolysis* **2017**, *124*, 536–541. <https://doi.org/10.1016/j.jaap.2017.01.028>.
- (107) Buss, W.; Hertzog, J.; Pietrzyk, J.; Carré, V.; Mackay, C. L.; Aubriet, F.; Mašek, O. Comparison of Pyrolysis Liquids from Continuous and Batch Biochar Production—Influence of Feedstock Evidenced by FTICR MS. *Energies* **2020**, *14* (1), 9. <https://doi.org/10.3390/en14010009>.
- (108) Chiaberge, S.; Leonardis, I.; Fiorani, T.; Cesti, P.; Reale, S.; Angelis, F. D. Bio-Oil from Waste: A Comprehensive Analytical Study by Soft-Ionization FTICR Mass Spectrometry. *Energy Fuels* **2014**, *28* (3), 2019–2026. <https://doi.org/10.1021/ef402452f>.
- (109) Wang, S.; Yang, C.; Xu, C.; Zhao, S.; Shi, Q. Separation and Characterization of Petroleum Asphaltene Fractions by ESI FT-ICR MS and UV-Vis Spectrometer. *Sci. China Chem.* **2013**, *56* (7), 856–862. <https://doi.org/10.1007/s11426-013-4900-2>.

- (110) Musin, L. I.; Foss, L. E.; Shabalin, K. V.; Nagornova, O. A.; Borisova, Y. Y.; Borisov, D. N.; Yakubov, M. R. Simple Methods for the Separation of Various Subfractions from Coal and Petroleum Asphaltenes. *Energy Fuels* **2020**, *34* (6), 6523–6543. <https://doi.org/10.1021/acs.energyfuels.9b03283>.
- (111) Tian, Y. X.; Guo, X.; Ma, J.; Liu, Q. Y.; Li, S. J.; Wu, Y. H.; Zhao, W. H.; Ma, S. Y.; Chen, H. Y.; Guo, F. Characterization of Biochar-Derived Organic Matter Extracted with Solvents of Differing Polarity via Ultrahigh-Resolution Mass Spectrometry. *Chemosphere* **2022**, *307*, 135785. <https://doi.org/10.1016/j.chemosphere.2022.135785>.
- (112) Chacón-Patiño, M. L.; Nelson, J.; Rogel, E.; Hench, K.; Poirier, L.; Lopez-Linares, F.; Ovalles, C. Vanadium and Nickel Distributions in Selective-Separated n-Heptane Asphaltenes of Heavy Crude Oils. *Fuel* **2022**, *312*, 122939. <https://doi.org/10.1016/j.fuel.2021.122939>.
- (113) Purcell, J. M.; Hendrickson, C. L.; Rodgers, R. P.; Marshall, A. G. Atmospheric Pressure Photoionization Fourier Transform Ion Cyclotron Resonance Mass Spectrometry for Complex Mixture Analysis. *Anal. Chem.* **2006**, *78* (16), 5906–5912. <https://doi.org/10.1021/ac060754h>.
- (114) Purcell, J. M.; Hendrickson, C. L.; Rodgers, R. P.; Marshall, A. G. Atmospheric Pressure Photoionization Proton Transfer for Complex Organic Mixtures Investigated by Fourier Transform Ion Cyclotron Resonance Mass Spectrometry. *J. Am. Soc. Mass Spectrom.* **2007**, *18* (9), 1682–1689. <https://doi.org/10.1016/j.jasms.2007.07.001>.
- (115) Cole, D. P.; Smith, E. A.; Lee, Y. J. High-Resolution Mass Spectrometric Characterization of Molecules on Biochar from Pyrolysis and Gasification of Switchgrass. *Energy Fuels* **2012**, *26* (6), 3803–3809. <https://doi.org/10.1021/ef300356u>.
- (116) Buss, W.; Hilber, I.; Graham, M. C.; Mašek, O. Composition of PAHs in Biochar and Implications for Biochar Production. *ACS Sustain. Chem. Eng.* **2022**, *10* (20), 6755–6765. <https://doi.org/10.1021/acssuschemeng.2c00952>.
- (117) Kuśmierz, M.; Oleszczuk, P.; Kraska, P.; Pałys, E.; Andruszczak, S. Persistence of Polycyclic Aromatic Hydrocarbons (PAHs) in Biochar-Amended Soil. *Chemosphere* **2016**, *146*, 272–279. <https://doi.org/10.1016/j.chemosphere.2015.12.010>.
- (118) Carrier, A. J.; Abdullahi, I.; Hawboldt, K. A.; Fiolek, B.; MacQuarrie, S. L. Probing Surface Functionality on Amorphous Carbons Using X-Ray Photoelectron Spectroscopy of Bound Metal Ions. *J. Phys. Chem. C* **2017**, *121* (47), 26300–26307. <https://doi.org/10.1021/acs.jpcc.7b06311>.

Appendix I: Additional optimized reactions

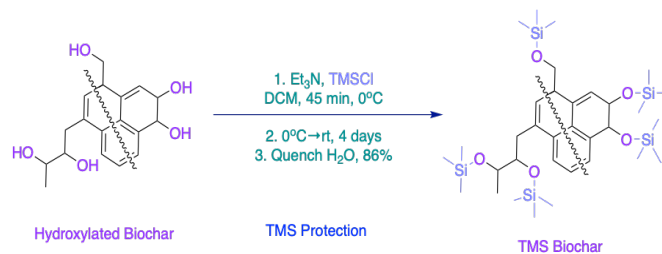
Synthesis of TMS-biochar



Procedure: Hydroxylated non-exfoliated hardwood biochar (250 mg) is suspended in CH_2Cl_2 (40.0 mL), and the reaction is cooled to 0°C under N_2 . The suspension is successively treated with Et_3N (9.30 mL) and TMSCl (7.00 mL) added dropwise. After complete transfer, the reaction mixture is warmed to r.t. and stirred for 96h days. The reaction mixture cooled on an ice bath and was quenched slowly with ice-cold H_2O (30.0 mL). The cooled mixture is suction filtered and washed with CH_2Cl_2 (10.0 mL), acetone (10.0 mL), CH_2Cl_2 (10.0 mL), H_2O (10.0 mL) and $\text{CH}_3\text{CH}_2\text{OH}$ (10.0 mL). The solid was dried in a vacuum oven overnight, and the resulting product was a black powdery solid (216 mg, 86%).

Discussion of TMS protection of Hydroxylated Biochar.

The non-exfoliated hydroxylated biochar underwent protection group chemistry that allowed the successful installation of a TMS group on the surface of the biochar (scheme 2.6) in 86% recovery. The nucleophilic hydroxyl group on the surface of biochar becomes deprotonated by TEA. The electrophilic silicon on the TMSCl substituent causes the chloride to be replaced, and TMS is added to the surface.



Scheme AI.1 Reaction scheme for TMS biochar.

The TMS-protecting group on the surface of the biochar was characterized by FT-IR (Figure AI.1.) The characteristic peaks were the less significant -OH stretching band at 3401 cm^{-1} and the methyl stretching bands at 2894 cm^{-1} . Another solid-state NMR characterization was completed by ^{13}C CPMAS, identifying the methyl peak at 46.23 ppm.

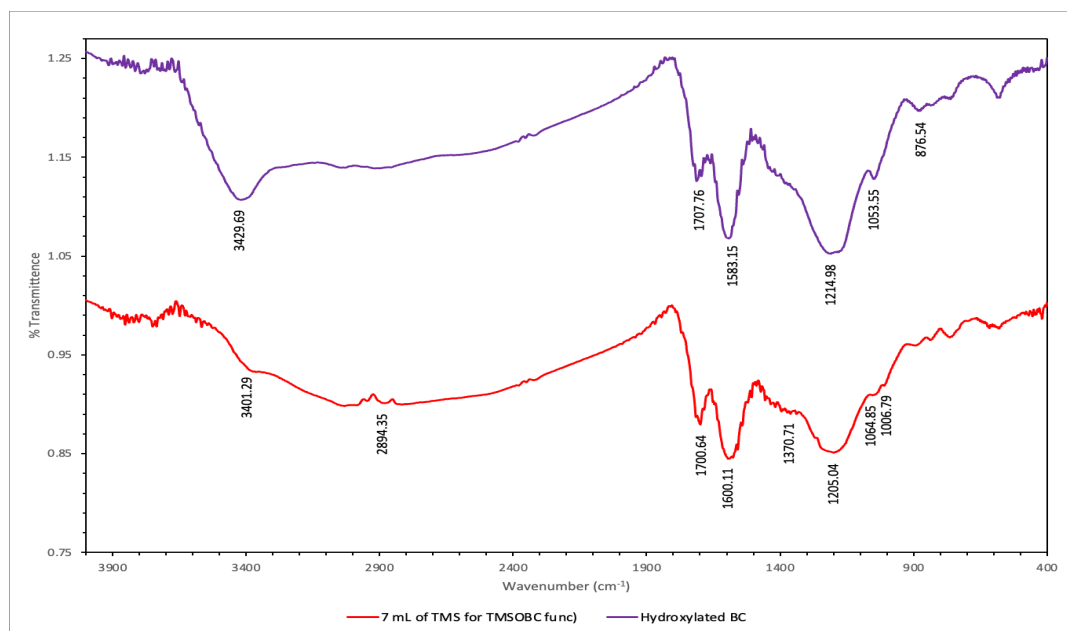


Figure AI.1 Stacked FT-IR spectra of TMS biochar and hydroxylated biochar.

Sample: Sample: SC-02-99 Oxydized biochar with TMS
Probe: MAS HCND
Expt: 13C{1H} CPMAS, 62.5 kHz HH, 100kHz dec
v=20kHz
T= 298K
ns=1k

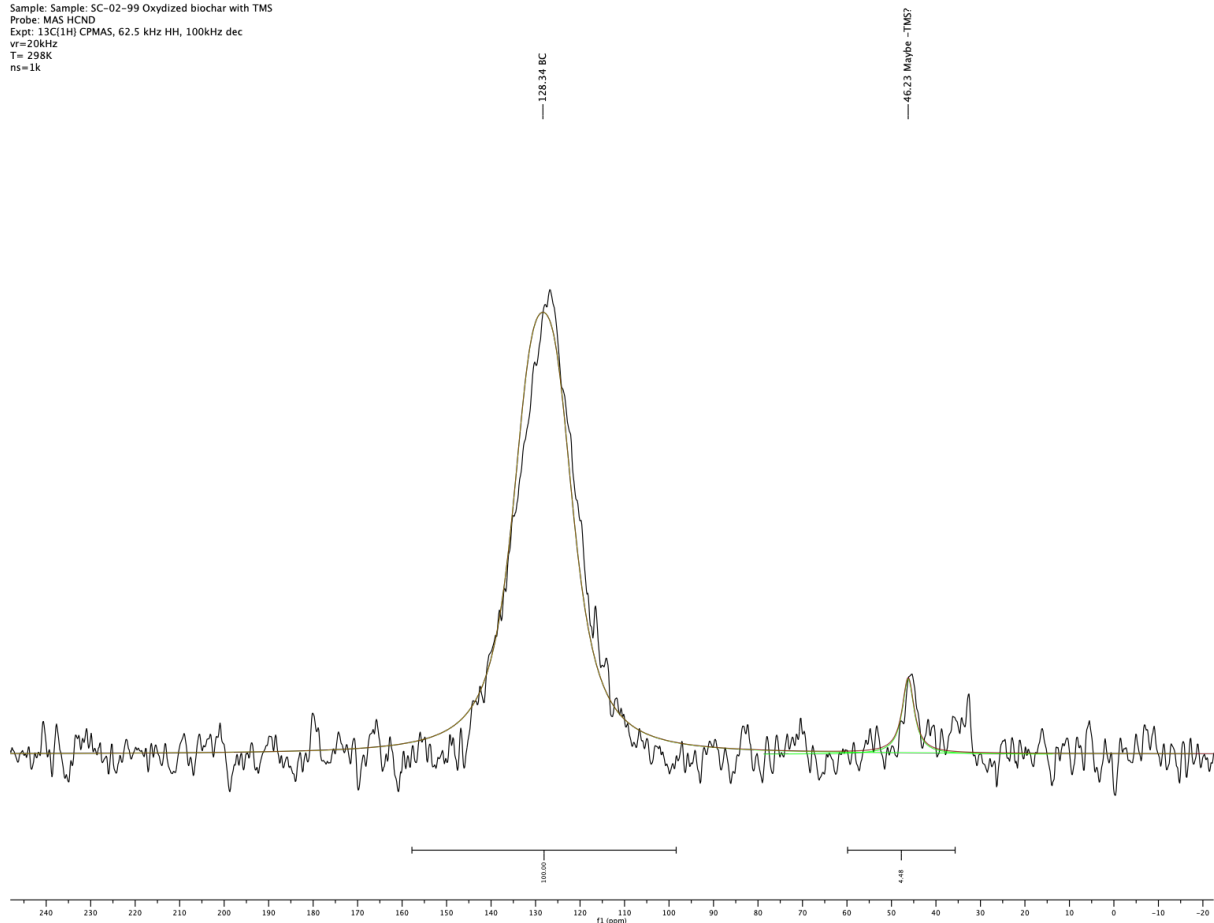


Figure A1.2 $^{13}\text{C}\{^1\text{H}\}$ CPMAS NMR spectrum of TMS biochar.

Appendix II: Reaction optimization studies

The optimization reaction studies for Chapter 2 CPTMS functionalization and phosphonium modification reaction.

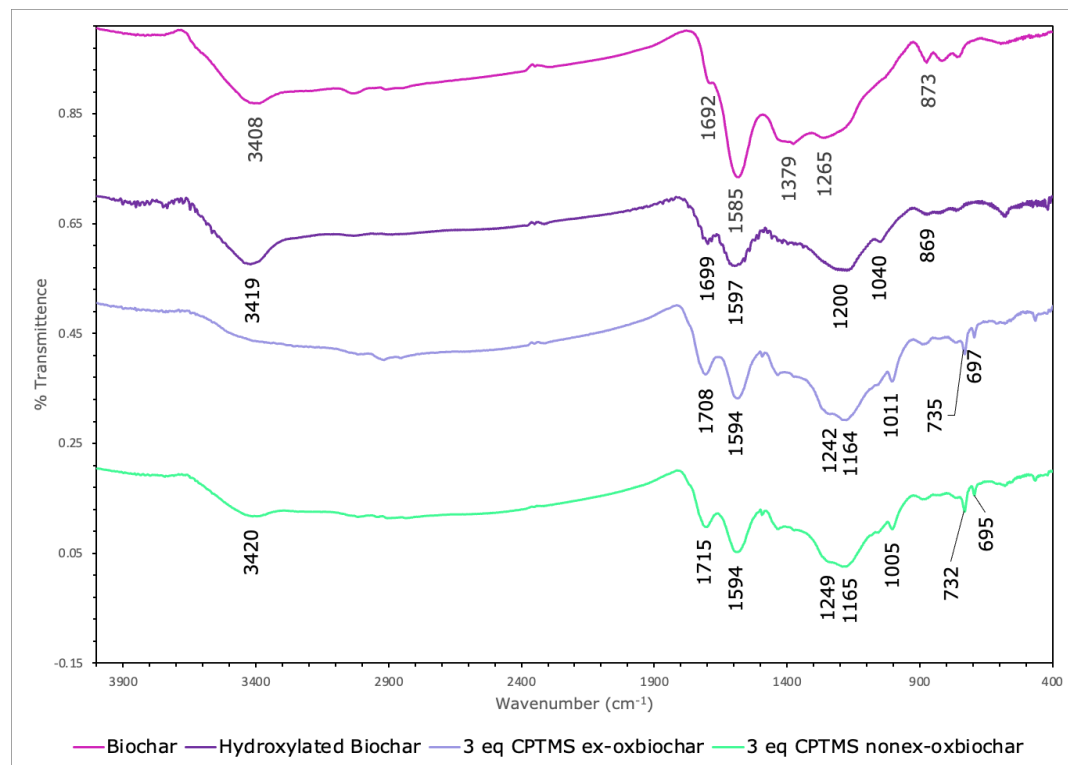


Figure AII.1 Stacked FT-IR spectra of biochar, hydroxylated biochar, and 3 eq CPTMS functionalized biochars.

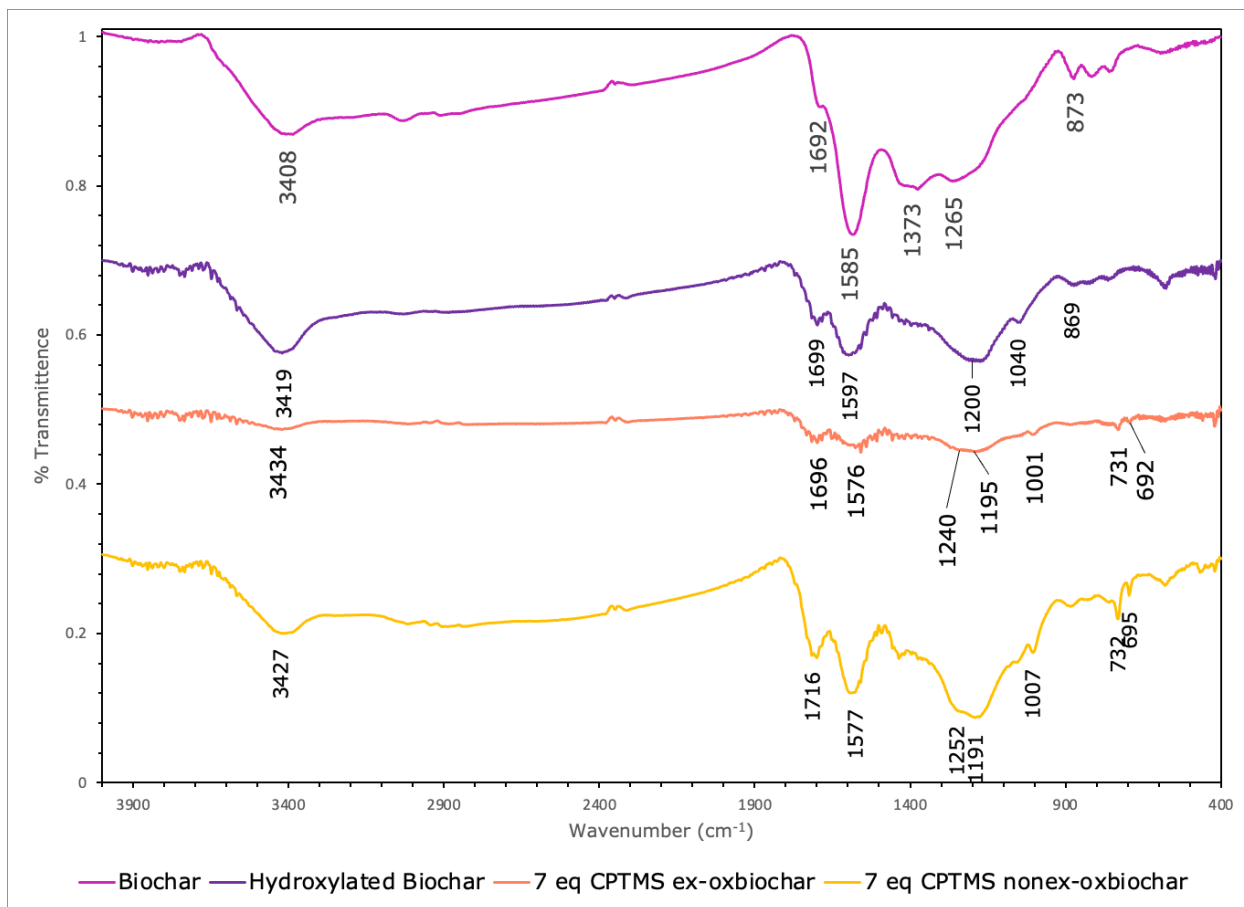


Figure AII.2 Stacked FT-IR spectra of biochar, hydroxylated biochar, and 7 eq CPTMS functionalized biochars

Table AII.1 The data summary of the 3, 7 and 9 eq of CPTMS optimization reactions for CPTMS biochar.

Eq of CPTMS	Exfoliation	Hydroxylated biochar	Experimental mass of CPTMS Biochar	Mass yield	Amount of CPTMS used	Mass of CPTMS recovered	Mass of CPTMS applied	Estimation of %CPTMS added to biochar
3	yes✓	202 mg	147 mg	73%	600 mg	294 mg	306 mg	51%
3	no✗	205 mg	170 mg	83%	600 mg	530 mg	70 mg	12%
7	yes✓	203 mg	159 mg	78%	1400 mg	790 mg	610 mg	44%
7	no✗	202 mg	176 mg	87%	1400 mg	750 mg	650 mg	46%
9	yes✓	201 mg	163 mg	81%	1800 mg	1120 mg	680 mg	38%
9	no✗	204 mg	169 mg	83%	1800 mg	1130 mg	670 mg	37%

Table AII.1 summarizes each optimization reaction condition; from this data, we can summarize that the most successful reaction was the most consistent for the subsequent synthesis step. 3 equivalents of CPTMS had the highest percent of CPTMS added to the surface of the hydroxylated biochar. Exfoliation seemed to have little effect on yield past 7 equivalents of CPTMS added by difference in mass of CPTMS applied to the surface of the hydroxylated biochar (table 2, mass of CPTMS applied) and became the most consistent after 7 equivalents of CPTMS reagent. When considering the IR of the optimizations (Figure 2.2), there are no significant differences in the bands between samples to identify the most suitable reaction conditions. To ensure the product and filtrate mass is only one by-product, the CPTMS reagent, the reaction filtrate was used for the mass quantification only contained CPTMS, and no residual solvents ^1H solution-state NMR was applied.

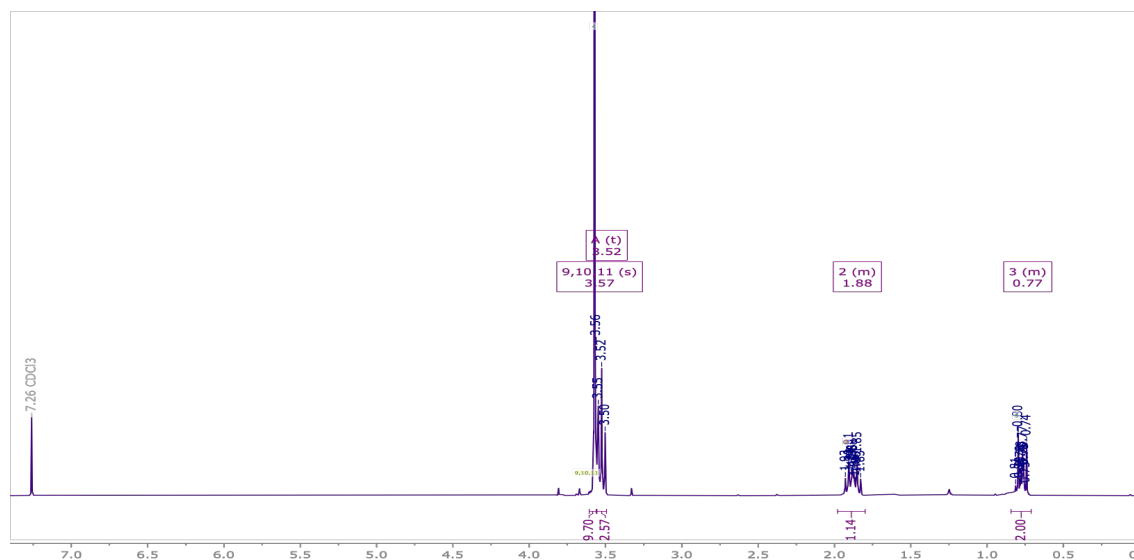


Figure AII.3 ^1H NMR spectrum of the CPTMS reaction filtrate in CDCl_3 .

The 3.57 ppm singlet indicates the $-OCH_3$ methyl peaks, the 3.52 ppm triplet represents the $-CH_2-Cl$ methylene protons, while the peaks at 1.88 ppm represent the $Si-CH_2-$ methylene protons, and 0.77 ppm is the $-CH_2-$ methylene peak in the middle of the propyl chain. This method for quantification to determine the mass of reagents is used for each synthetic step in this project.

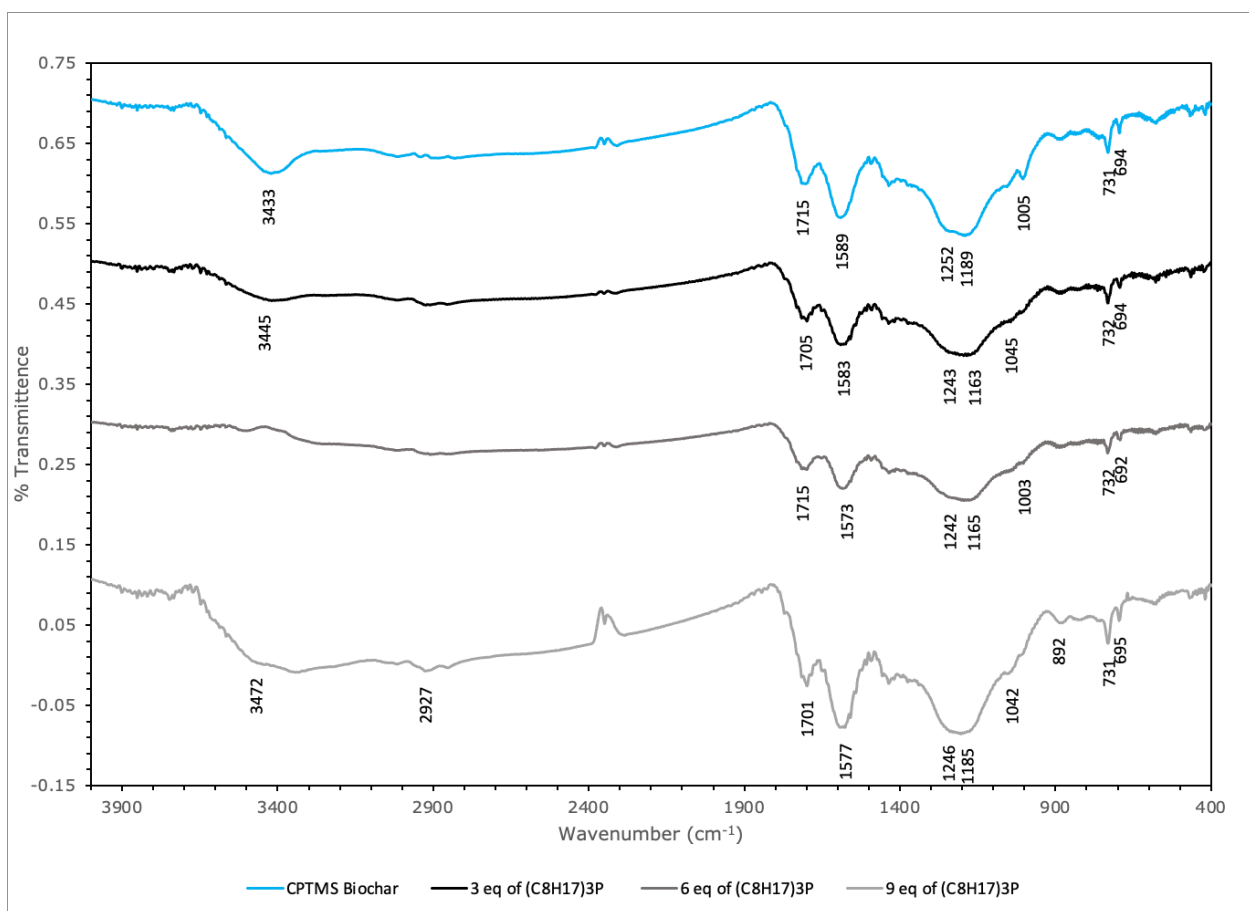


Figure AII.4 Stacked FT-IR spectra of 48 h phosphonium modification reaction on non-exfoliated biochar.

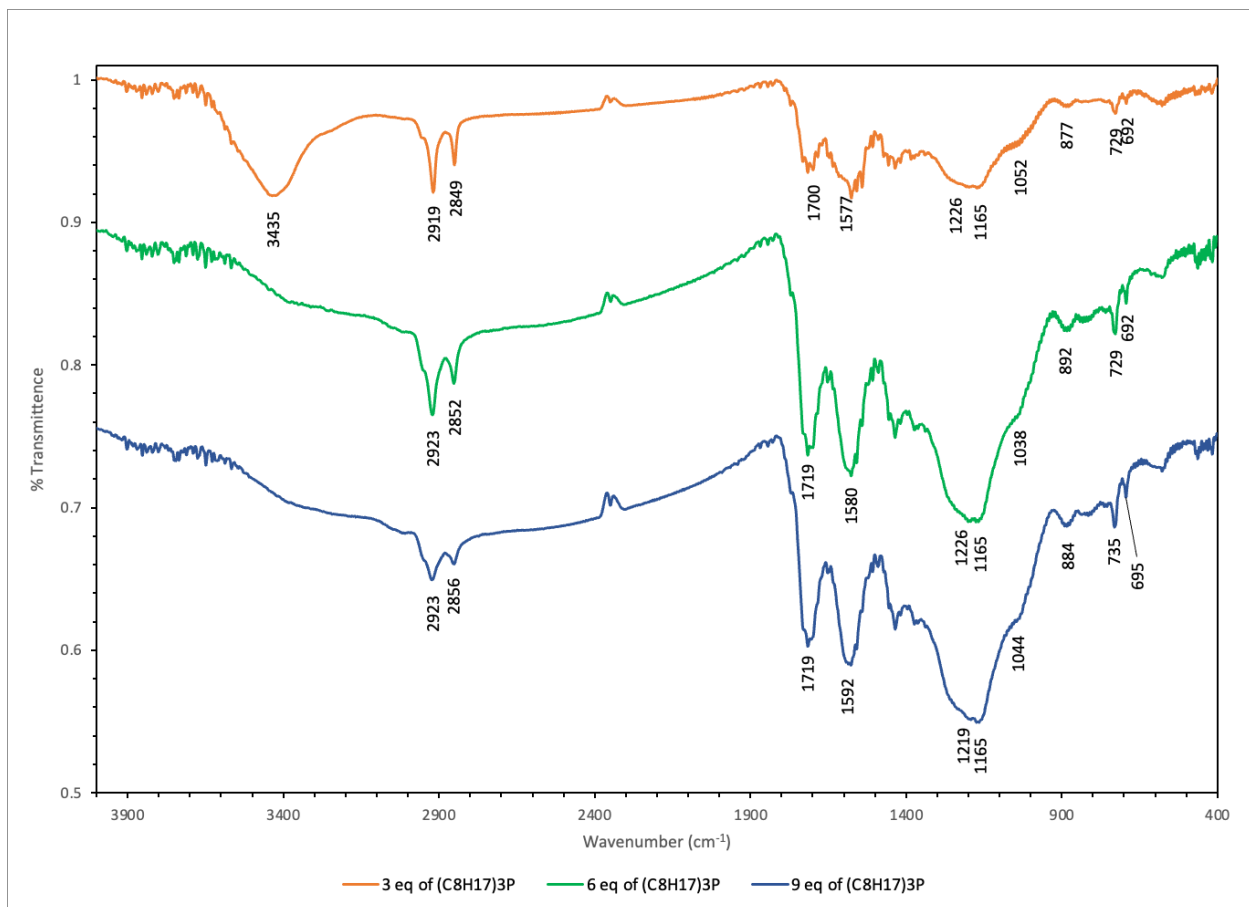


Figure AII.5 Stacked FT-IR spectra of 3, 6 and 9 eq of TOP (w/w) applied to CPTMS-biochar to synthesize (C₈H₁₇)₃P⁺Cl⁻ biochar over 96 h.

Table AII.2 The data summary of the 3, 6 and 9 eq of TOP optimization reactions for $(C_8H_{17})_3P^+Cl^-$ biochar.

Eq of trioctyl phosphine	Exfoliation	Amount of CPTMS Biochar	Mass of $(C_8H_{17})_3P^+Cl^-$ Biochar	Mass yield	Amount of trioctyl phosphine used	Mass of trioctyl phosphine recovered	Time
3	Yes ✓	49.2 mg	26.0 mg	53%	150 mg	240 mg	96 h
3	No ✗	49.2 mg	21.2 mg	43%	150 mg	390 mg	48 h
6	Yes ✓	48.9 mg	28.5 mg	58%	300 mg	430 mg	96 h
6	No ✗	49.1 mg	19.3 mg	39%	300 mg	510 mg	48 h
9	Yes ✓	50.3 mg	31.1 mg	62%	450 mg	720 mg	96 h
9	No ✗	52.4 mg	19.1 mg	36%	450 mg	730 mg	48 h

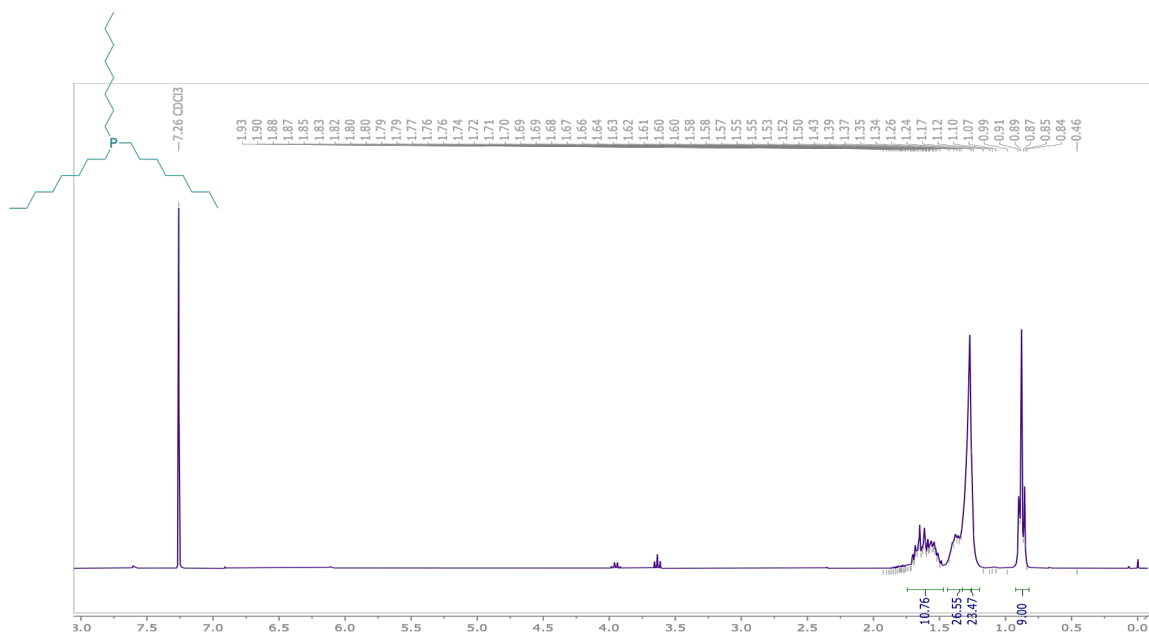


Figure AII.6 ^1H NMR spectrum of TOP by-product from filtrate quantification in CDCl_3 .

The mass of the recovered filtrate (table 2.2) was higher than the initial mass of the starting materials used in each reaction is further investigated. To guarantee that either TOP or TOPO was the only product in the filtrate, the filtrate was dried using a Schenk line for four days. When no weight change was observed between this time frame and in **Figure AII.6**, there were no residual solvent peaks in the NMR the product was sufficiently dried.

SI 1. All biochar characterization: ^1H NMR, ^{13}C NMR, IR, and ^{31}P data.

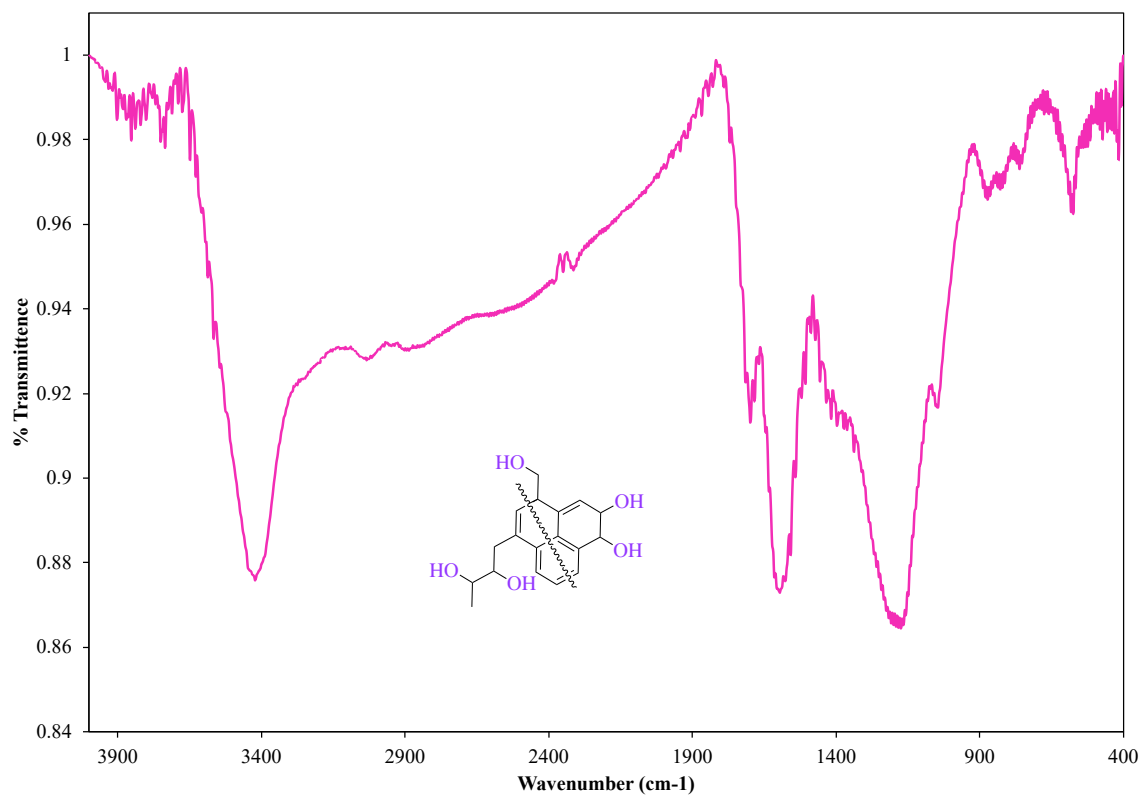


Figure SI 1.1 FT-IR spectra of hydroxylated biochar.

Table SI 1.1 Characterization summary of FT-IR spectroscopy assignments.

assignment	biochar	hydroxylated biochar
C=C stretching	1585 cm ⁻¹	1597 cm ⁻¹
C=C bending	873 cm ⁻¹	869 cm ⁻¹
C-O stretching	1265 cm ⁻¹	1200 cm ⁻¹
C-O stretching		1040 cm ⁻¹
-OH stretching	3408 cm ⁻¹	3419 cm ⁻¹
-OH bending	1692 cm ⁻¹	1699 cm ⁻¹

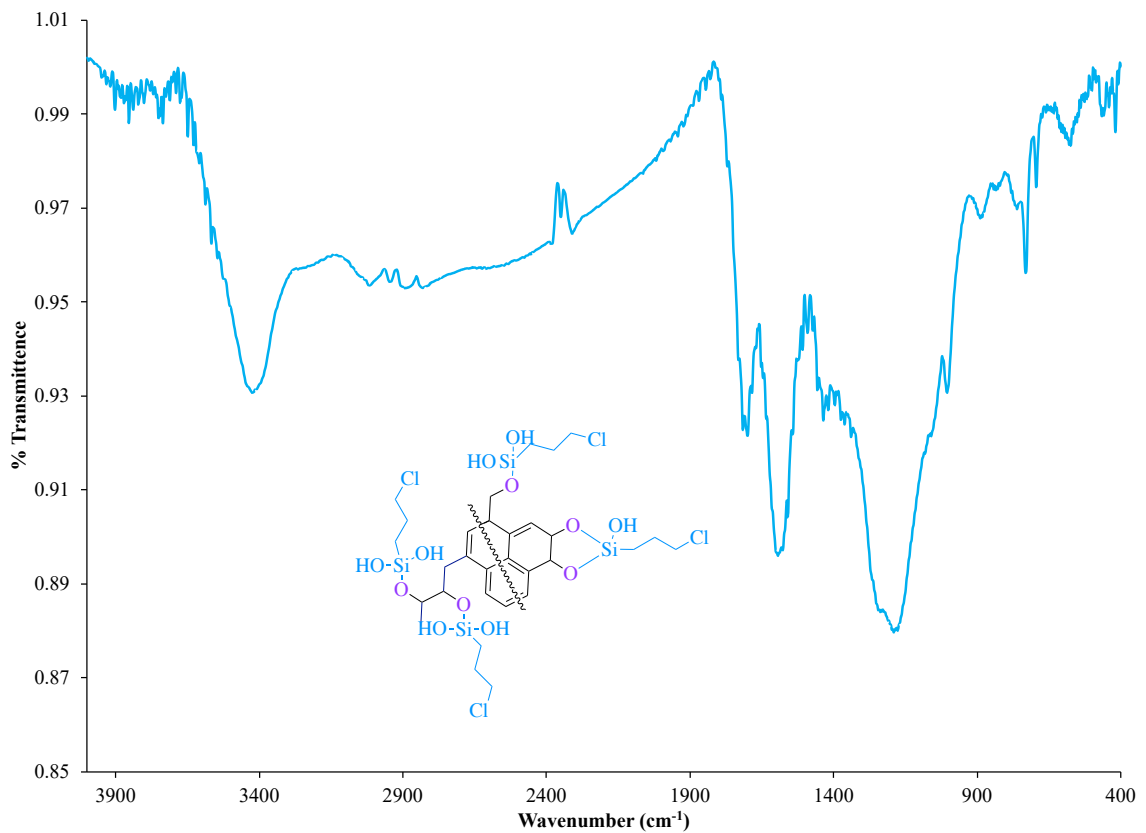


Figure SI 1.2 FT-IR spectra of CPTMS-biochar.

Table SI 1.2 Comparison of functional group characterization by FT-IR spectroscopy of CPTMS-biochar

assignment	hydroxylated biochar	CPTMS-biochar
C=C stretching	1597 cm ⁻¹	1597 cm ⁻¹
C=C bending	869 cm ⁻¹	829 cm ⁻¹
C-O stretching	1200 cm ⁻¹	1237 cm ⁻¹
C-O stretching	1040 cm ⁻¹	1018 cm ⁻¹
C-Si stretching		1165 cm ⁻¹
Si-O stretch		729 cm ⁻¹
-OH stretching	3419 cm ⁻¹	3401 cm ⁻¹
-OH bending	1699 cm ⁻¹	1700 cm ⁻¹
C-Cl stretch		692 cm ⁻¹
C-H stretch		2894 cm ⁻¹

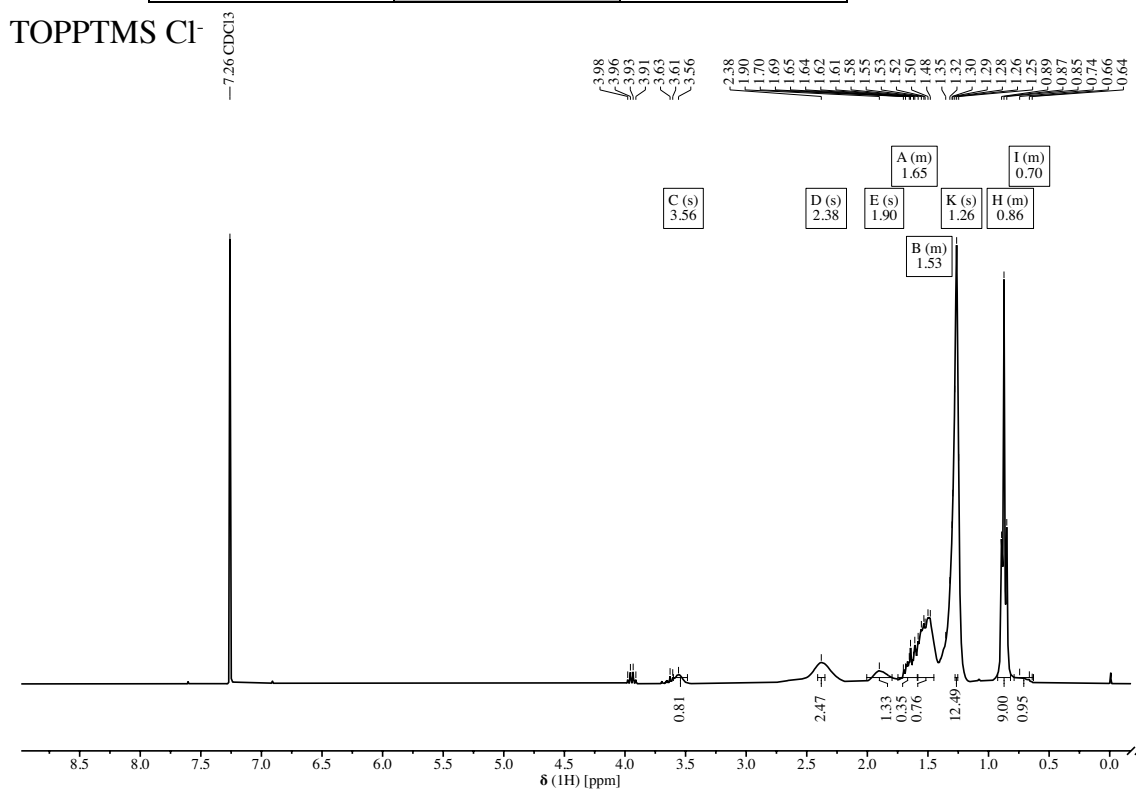


Figure SI. 1.3 ¹H NMR spectrum of TOPPTMS Cl⁻ in CDCl₃.

TOPPTMS Cl⁻

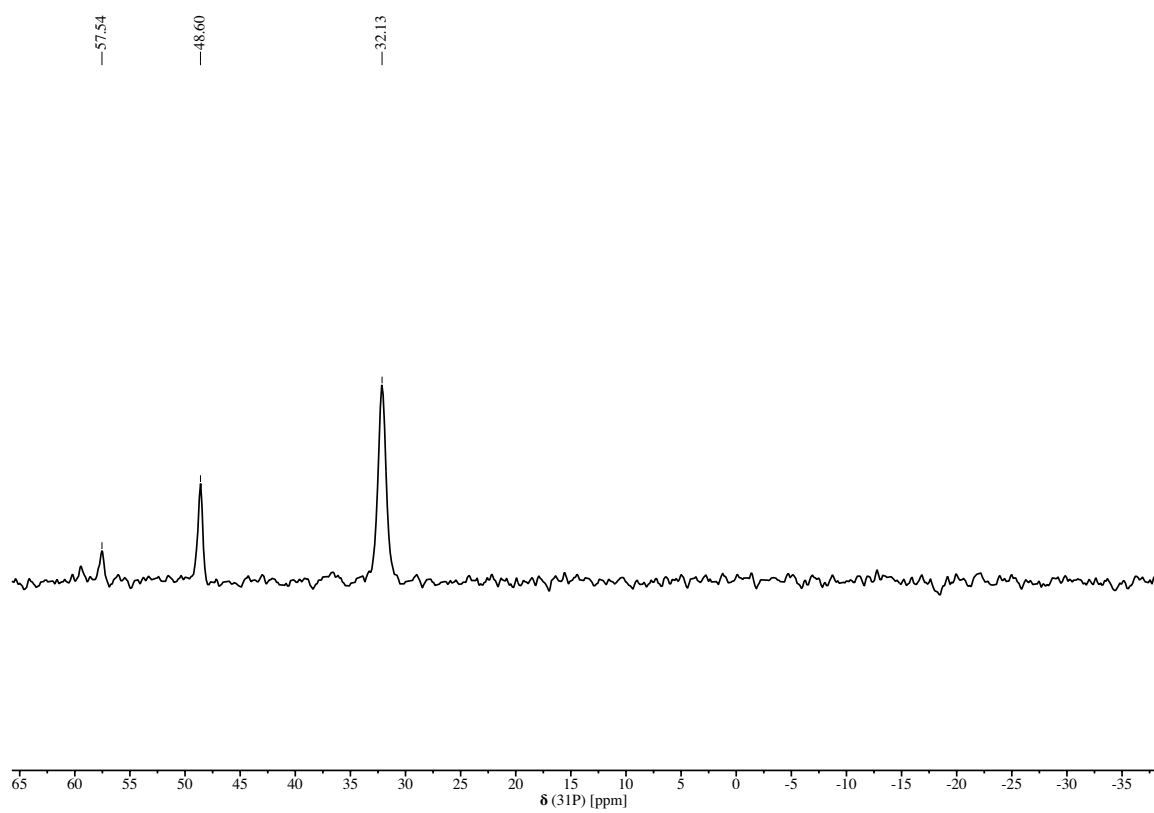


Figure SI. 1.4 ³¹P decoupled NMR spectrum of TOPPTMS Cl⁻ in CDCl₃.

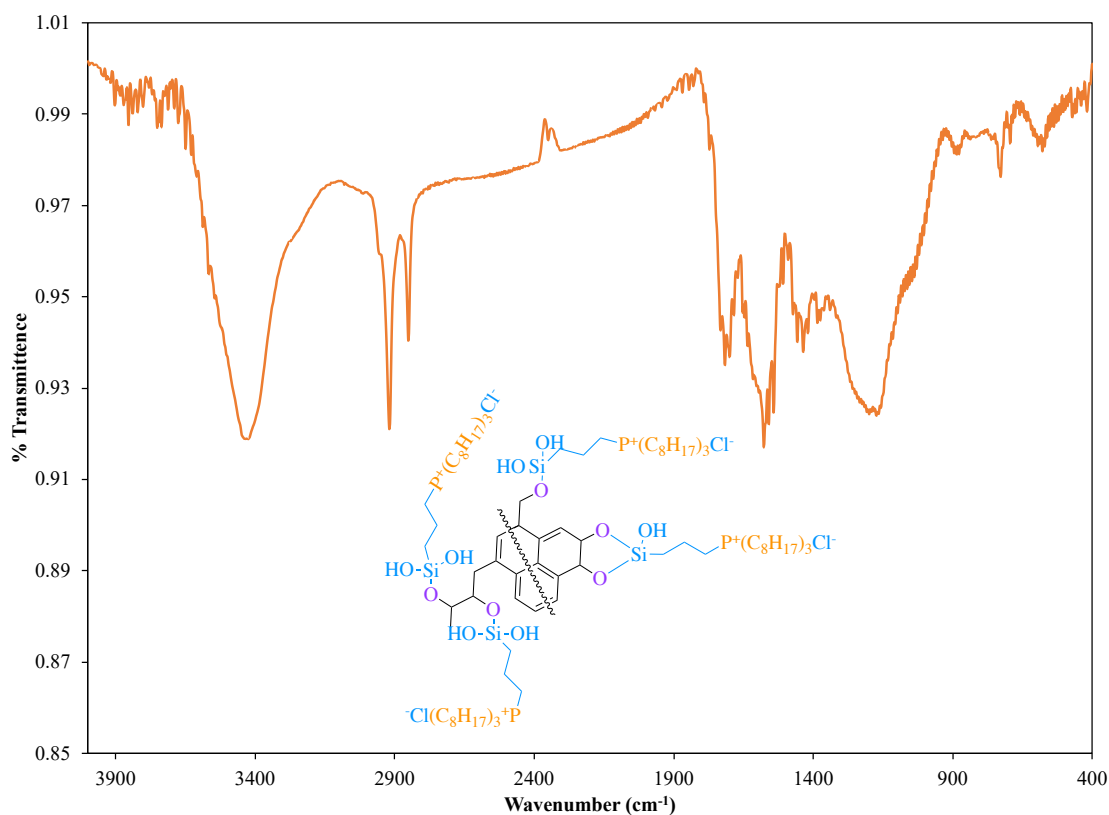


Figure SI 1.5 FT-IR spectra of $(C_8H_{17})_3P^+ Cl^-$ biochar.

Table SI 1.3 Comparison of functional group characterization by FT-IR spectroscopy of $(C_8H_{17})_3P^+ Cl^-$ biochar.

Assignment	CPTMS-biochar	$(C_8H_{17})_3P^+ Cl^-$ biochar
C=C stretching	1595 cm^{-1}	1577 cm^{-1}
C=C bending	829 cm^{-1}	877 cm^{-1}
C-O stretching	1237 cm^{-1}	1226 cm^{-1}
C-O stretching	1018 cm^{-1}	1052 cm^{-1}
C-Si stretching	1165 cm^{-1}	1165 cm^{-1}
Si-O stretch	729 cm^{-1}	729 cm^{-1}
-OH stretching	3401 cm^{-1}	3435 cm^{-1}
-OH bending	1700 cm^{-1}	1700 cm^{-1}

C-Cl stretch	692 cm ⁻¹	692 cm ⁻¹
C-H stretch	2894 cm ⁻¹	2849 cm ⁻¹
CH ₃		2919 cm ⁻¹

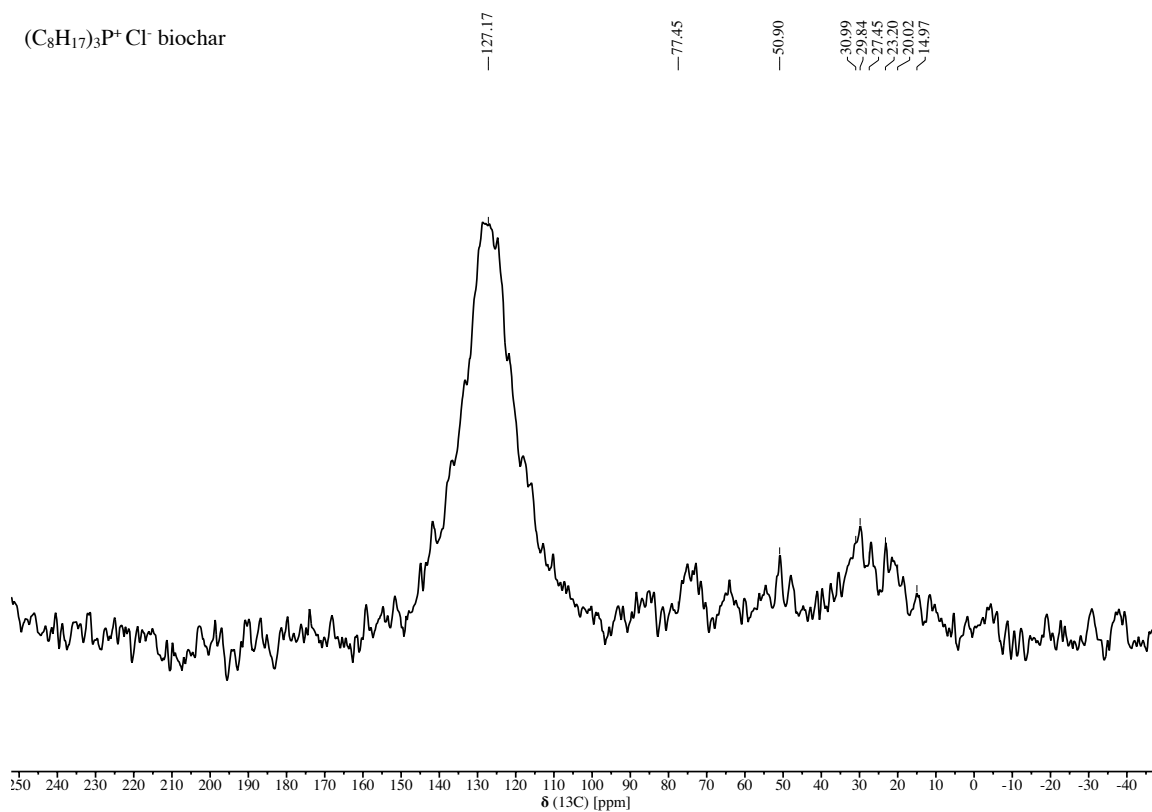


Figure SI 1.6 ¹³C {¹H} CPMAS NMR spectrum of (C₈H₁₇)₃P⁺Cl⁻ biochar.

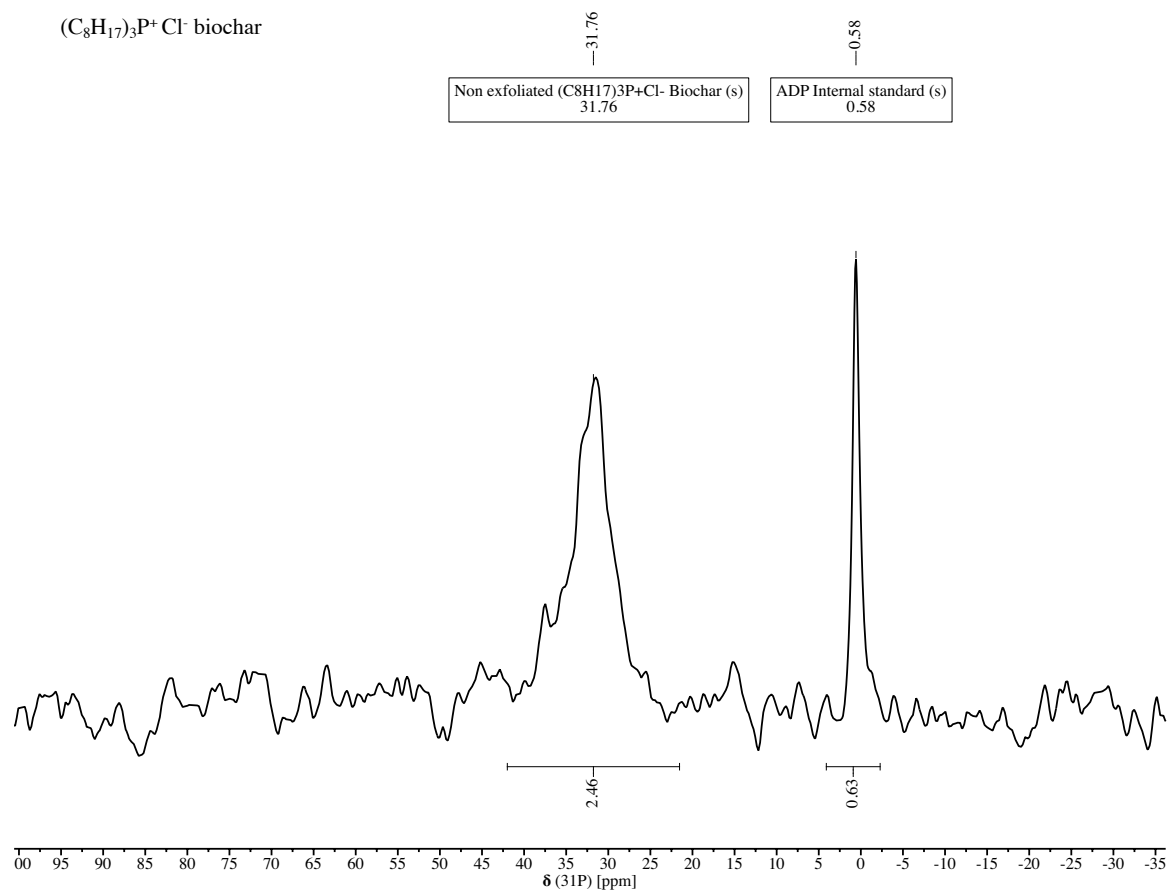


Figure SI 1.7 $^{31}\text{P}\{^1\text{H}\}$ CPMAS NMR spectrum of non-exfoliated indirect synthesis of (C₈H₁₇)₃P⁺Cl⁻ biochar using ADP as the internal standard.

SI 2. Surface contact angle measurement



Figure SI 2.1 Surface contact angle experimental setup



Figure SI 2.2 The contact surface angle measurements of exfoliated indirect synthesis of $(\text{C}_8\text{H}_{17})_3\text{P}^+\text{Cl}^-$ biochar.

Above photos represent each of the pictures taken for each of the different samples of $(\text{C}_8\text{H}_{17})_3\text{P}^+\text{Cl}^-$ biochar that was used to determine angle of hydrophobicity, text was added during sample analysis to stay organized.

SI 3. Quantification of Phosphorus on biochar

Chapter 2: Calculations of the quantification of phosphorus on the surface of biochar.

Non-exfoliated biochar is used for sample calculations.

Calculation of n_{TPP}

$n_{TPP} = 0.01919 \text{ g} / 262.29 \text{ g/mol} = 7.31 \text{ mmol} = 7.31 \text{ mmol}$ of phosphorus.

$$n_{TPP} = \frac{\text{mass of TPP}}{Mm \text{ of TPP}} = \frac{0.01919 \text{ g}}{262. \text{g/mol}} = 7.31 \text{ mmol per mol of TPP}$$

$$n_{P,BC} = n_{TPP} \cdot \frac{0.16}{1.00} = 7.31 \text{ mmol} \cdot 0.16 = 11 \text{ } \mu\text{mol of P in 26.77 mg sample.}$$

$$m_{PBC} = n_P \cdot Mm_{P,atomic \text{ mass}} = 1.10 \times 10^5 \text{ mol} \cdot 30.97 \text{ g/mol} = 0.341 \text{ mg of P}$$

$$m\%_{P,BC} = \frac{\text{mass of P in samples}}{\text{total mass of P biochar}} \cdot 100\% = \frac{0.341 \text{ mg}}{26.77 \text{ mg}} \cdot 100\% = 1.3\% \text{ P}$$

functionalization.

Sample 2: 7.5×10^{-5} mol (2.32 mg P) in 20 mg sample = 11.6 % P functionalization

Sample 3: 1.19×10^{-4} mol (3.69 mg P) in 20.5 mg sample 18.0 % P functionalization

SI 4. Capacitance and potential window calculations

Chapter 3 Capacitance calculations:

$$C(Fg^{-1}) = (I \int (1/V(t))dt)/m$$

Table SI. 4.1 Electrochemical data summary

Electrode	Cell	Mass on surface of electrode (mg)	Current (μA)	T_i (s)	Potential window (V)	Capacitance (C) (F/g)
A	I	0.65	150	20.62	+1.70 to - 0.87	3.52
B	I	0.68	0.6	20.02	+ 0.81 to - 0.43	0.08
C	II	6.5	132	20.06	+0.80 to - 0.86	1.22
D	II	6.5	4	20.00	+ 1.0 to - 0.37	0.05
E	I	0.63	150	20.00	+ 0.89 to - 1.0	11.0
F	I	0.46	150	20.8	+ 0.78 to + 0.19	29.3
G	I	0.34	150	20.5	+ 0.79 to - 1.0	10.2

SI 5. Data summaries of solvent extracts from hardwood biochar.

Table SI 5.1 The data summary of the whole fraction is based on the highest relative abundance of HC, O₁ and N₁ classes in hardwood biochar extracted by solvent extrography. Values shaded represent the protonated HC (blue), radical HC (blue), protonated O₁ species (green) and radical O₁ species (orange). No N₁ species are detected.

Formula	DBE	Abundance
C ₁₄ H ₁₄	8	8.4307
C ₁₆ H ₁₈	8	5.3952
C ₁₉ H ₁₂	14	4.2339
C ₂₄ H ₂₆	12	3.231
C ₁₇ H ₂₀	8	3.0454
C ₁₈ H ₁₀	14	2.9977
C ₁₅ H ₁₆	86	2.8862
C ₂₀ H ₁₄	14	2.3957
C ₂₂ H ₂₂	12	1.1031
C ₁₈ H ₁₂	13	10.0601
C ₁₉ H ₁₄	13	5.9855
C ₂₀ H ₁₆	13	2.349
C ₁₆ H ₈	13	0.7487
C ₁₇ H ₁₈ O	9	74.8734
C ₁₇ H ₂₀ O	8	50.2643
C ₁₄ H ₁₄ O	8	21.5608
C ₁₆ H ₁₈ O	8	13.0365
C ₁₅ H ₁₄ O	9	12.2155
C ₁₈ H ₂₀ O	9	9.2489

C ₂₄ H ₂₆ O	12	7.7122
C ₁₇ H ₂₀ O	8	38.6285
C ₁₄ H ₁₄ O	8	4.4526
C ₁₅ H ₁₆ O	8	2.5809
C ₁₆ H ₁₈ O	8	1.2335
C ₁₈ H ₂₂ O	8	0.9095
C ₁₃ H ₁₄ O	7	0.908

Table SI 5.2 The data summary of the acetone fraction of the most abundant HC, O₁ and N₁ classes in hardwood biochar was extracted by solvent extrography. Values shaded represent the protonated HC (blue), radical HC (blue), protonated N₁ species (pink), radical N₁ species (purple), protonated O₁ species (green), and radical O₁ species (orange).

Formula	DBE	Relative Abundance
C ₁₇ H ₁₄	11	86.4098
C ₁₉ H ₁₄	13	70.1522
C ₁₄ H ₁₀	10	53.4360
C ₁₆ H ₁₀	12	37.7557
C ₁₇ H ₁₀	13	32.1996
C ₁₅ H ₁₀	11	30.5984
C ₁₄ H ₁₂	9	27.0039
C ₁₄ H ₁₀	10	100.6311
C ₁₆ H ₁₀	12	54.1071
C ₁₈ H ₁₂	13	40.5808
C ₁₆ H ₁₂	11	32.6037
C ₁₅ H ₁₂	10	21.0562

Formula	DBE	Relative Abundance
C ₁₄ H ₈	11	16.5965
C ₁₈ H ₁₀	14	14.6591
C ₁₇ H ₁₃ N	12	2.5359
C ₁₅ H ₁₃ N	10	2.34
C ₁₆ H ₁₃ N	11	2.3378
C ₁₆ H ₁₁ N	12	2.25
C ₁₉ H ₁₅ N	13	1.8825
C ₁₇ H ₁₅ N	11	1.8134
C ₁₉ H ₁₇ N	12	1.5753
C ₁₈ H ₁₅ N	12	1.5493
C ₁₆ H ₁₁ N	12	1.5846
3C ₁₇ H ₁₃ N	12	1.1611
C ₁₈ H ₂₀ O	9	19.0038
C ₁₅ H ₁₂ O	10	15.9681
C ₁₆ H ₁₂ O	11	13.3871
C ₁₄ H ₁₀ O	10	11.2571
C ₁₇ H ₁₄ O	11	11.1391
C ₁₃ H ₈ O	10	10.4666
C ₁₅ H ₁₀ O	11	10.3004
C ₁₆ H ₁₄ O	10	9.8007
C ₁₇ H ₁₆ O	10	7.8614
C ₁₆ H ₁₀ O	12	7.7817

Formula	DBE	Relative Abundance
C ₁₄ H ₁₀ O	10	7.9831
C ₁₅ H ₁₂ O	10	7.0747
C ₁₆ H ₁₂ O	11	5.5694
C ₁₃ H ₁₀ O	9	5.5494
C ₁₆ H ₁₀ O	12	4.7165
C ₁₆ H ₁₄ O	10	4.3342
C ₁₇ H ₁₄ O	11	3.8073
C ₁₇ H ₁₂ O	12	3.5042
C ₁₄ H ₁₂ O	9	2.8486
C ₁₉ H ₁₄ O	13	2.3078

Table S I 5.3 The data summary of the heptane/toluene fraction of the most abundant HC, O₁ and N₁ classes in hardwood biochar extracted by solvent extrography. Values shaded represent the protonated HC (blue), radical HC (blue), protonated N₁ species (pink), radical N₁ species (purple), protonated O₁ species (green), and radical O₁ species (orange).

Formula	DBE	Abundance
C ₁₇ H ₁₄	11	9.7915
C ₁₈ H ₁₆	11	6.7619
C ₁₉ H ₁₆	12	6.5067
C ₁₈ H ₁₄	12	6.2309
C ₁₉ H ₂₄	8	4.1155
C ₁₇ H ₁₈	9	4.0995
C ₁₈ H ₁₈	10	3.5527

Formula	DBE	Abundance
C ₁₇ H ₁₆	10	3.5499
C ₂₀ H ₁₆	13	3.0992
C ₂₀ H ₁₈	12	2.8341
C ₃₁ H ₄₆	9	2.7084
C ₂₉ H ₄₂	9	2.6761
C ₃₁ H ₄₈	8	2.5779
C ₁₈ H ₁₂	12	2.5775
C ₃₀ H ₄₄	9	2.454
C ₃₂ H ₄₈	9	2.3833
C ₃₁ H ₄₄	10	2.3458
C ₃₂ H ₅₀	8	2.3308
C ₃₀ H ₄₇ N	8	100.5347
C ₂₁ H ₂₉ N	8	19.6422
C ₂₅ H ₃₅ N	9	17.1946
C ₂₄ H ₃₃ N	9	16.2824
C ₁₆ H ₁₇ N	9	0.1179
C ₁₇ H ₁₉ N	9	0.0885
C ₁₇ H ₁₈ O	9	9.3676
C ₁₆ H ₁₈ O	8	7.9146
C ₁₇ H ₁₆ O	10	6.3648
C ₁₇ H ₂₀ O	8	5.7542
C ₁₈ H ₂₀ O	9	4.1124
C ₁₆ H ₁₆ O	9	2.9953
C ₁₇ H ₁₈ O	9	1.6232

Formula	DBE	Abundance
C ₁₇ H ₁₆ O	10	0.9218
C ₁₇ H ₁₀ O	13	0.9129
C ₁₇ H ₁₄ O	11	0.8424
C ₁₈ H ₁₆ O	11	0.8104
C ₁₇ H ₁₂ O	12	0.7985

Table S I 5.4 The data summary of the Tol/THF/MeOH fractions of the most abundant HC, O₁ and N₁ classes in hardwood biochar extracted by solvent extrography. Values shaded represent the protonated HC (blue), radical HC (blue), protonated N₁ species (pink), radical N₁ species (purple), protonated O₁ species (green), and radical O₁ species (orange).

Formula	DBE	Abundance
C ₁₇ H ₁₈	9	15.1673
C ₁₇ H ₁₄	11	9.4377
C ₁₇ H ₁₆	10	8.1528
C ₁₉ H ₁₄	13	5.2876
C ₂₀ H ₂₂	10	3.6296
C ₂₁ H ₂₂	11	3.5408
C ₁₈ H ₂₀	9	3.4496
C ₁₇ H ₂₀	8	3.0725
C ₂₁ H ₂₀	12	3.0634
C ₂₀ H ₂₀	11	2.9079
C ₁₇ H ₂₀ O	8	40.7969
C ₁₇ H ₁₈ O	9	31.9022
C ₁₈ H ₁₈ O	10	12.8015
C ₁₈ H ₂₂ O	8	11.1306

Formula	DBE	Abundance
$C_{16}H_{18}O$	8	9.9809
$C_{17}H_{16}O$	10	8.9627

SI 6. Data summaries of solvent extracts from crab biochar.

Table SI 6.1 The data summary of the whole fraction based on the highest relative abundant HC, O₁ and N₁ classes in crab biochar extracted by solvent extrography. Values shaded represent the protonated HC (blue), radical HC (blue), protonated N₁ species (pink), radical N₁ species (purple), protonated O₁ species (green), and radical O₁ species (orange).

Formula	DBE	Abundance
C ₁₇ H ₁₄	11	102.0089
C ₁₄ H ₁₂	9	94.9107
C ₁₇ H ₁₈	9	64.4841
C ₁₉ H ₁₄	13	59.996
C ₁₇ H ₁₆	10	30.9926
C ₁₆ H ₁₄	10	28.4773
C ₁₇ H ₂₀	8	24.5038
C ₁₅ H ₁₄	9	24.0899
C ₁₈ H ₁₈	10	16.7431
C ₁₄ H ₁₀	10	15.041
C ₁₇ H ₁₈	9	44.4785
C ₁₄ H ₁₀	10	25.2893
C ₁₆ H ₁₂	11	14.3305
C ₁₈ H ₁₂	13	13.9813
C ₁₆ H ₁₀	12	12.2966
C ₁₇ H ₁₆	10	8.2149
C ₁₅ H ₁₄	9	8.1549
C ₁₉ H ₁₄	13	7.4066
C ₁₄ H ₁₂	9	5.956

Formula	DBE	Abundance
C ₁₇ H ₁₃ N	12	1.3216
C ₁₈ H ₁₅ N	12	0.7903
C ₁₆ H ₁₁ N	12	0.7815
C ₁₇ H ₂₀ O	8	85.3949
C ₁₇ H ₁₈ O	9	68.9018
C ₁₄ H ₁₄ O	8	45.2659
C ₁₈ H ₁₈ O	10	36.3004
C ₁₇ H ₁₆ O	10	25.2494
C ₁₈ H ₂₀ O	9	23.3915
C ₁₆ H ₁₈ O	8	20.7809
C ₁₅ H ₁₄ O	9	20.2059
C ₂₀ H ₂₂ O	10	18.9551
C ₁₇ H ₂₀ O	8	43.6988
C ₁₇ H ₁₈ O	9	11.8267
C ₁₄ H ₁₄ O	8	9.5712
C ₂₀ H ₂₂ O	10	5.9197
C ₁₅ H ₁₆ O	8	4.8209
C ₂₀ H ₂₄ O	9	4.5946
C ₁₇ H ₁₆ O	10	4.3861
C ₁₆ H ₁₄ O	10	3.3265
C ₁₆ H ₁₈ O	8	2.4084
C ₁₈ H ₂₀ O	9	2.2849

Table SI 6.2 The data summary of the acetone fraction of the most abundant HC, O₁ and N₁ classes in crab biochar extracted by solvent extrography. Values shaded represent the protonated HC (blue), radical HC (blue), protonated N₁ species (pink), radical N₁ species (purple), protonated O₁ species (green), and radical O₁ species (orange).

Formula	DBE	Abundance
C ₁₄ H ₁₂	9	59.1936
C ₁₇ H ₁₈	9	46.294
C ₁₇ H ₁₄	11	31.1256
C ₁₉ H ₁₄	13	17.2453
C ₁₇ H ₁₆	10	16.2988
C ₁₈ H ₁₈	10	10.4491
C ₂₀ H ₂₂	10	9.6018
C ₁₇ H ₂₀	8	8.6881
C ₁₅ H ₁₄	9	8.294
C ₂₁ H ₂₄	10	7.4974
C ₁₄ H ₁₀	10	9.3951
C ₁₆ H ₁₂	11	4.3624
C ₁₆ H ₁₀	12	3.6848
C ₁₇ H ₁₄	11	1.892
C ₁₆ H ₁₄	10	1.5524
C ₁₅ H ₁₂	10	1.4777
C ₁₇ H ₁₆	10	1.3407
C ₁₇ H ₁₂	12	1.1775
C ₁₅ H ₁₀	11	0.8586
C ₁₈ H ₁₈	10	0.7942

Formula	DBE	Abundance
C ₁₄ H ₁₂	9	59.1936
C ₁₃ H ₁₃ N	8	2.9788
C ₁₇ H ₁₅ N	11	2.1702
C ₁₇ H ₁₃ N	12	2.1021
C ₁₆ H ₁₃ N	11	2.1014
C ₁₄ H ₁₅ N	8	1.9932
C ₁₅ H ₁₇ N	8	1.2236
C ₁₇ H ₂₀ O	8	100.0427
C ₁₇ H ₁₈ O	9	60.488
C ₁₈ H ₁₈ O	10	25.593
C ₂₄ H ₂₆ O	12	17.7548
C ₁₇ H ₁₆ O	10	16.701
C ₂₀ H ₂₂ O	10	16.5279
C ₁₈ H ₂₀ O	9	15.1383
C ₂₀ H ₂₄ O	9	14.6529
C ₁₆ H ₁₈ O	8	9.9019
C ₂₁ H ₂₆ O	9	9.2185
C ₁₇ H ₂₀ O	8	6.0086
C ₁₇ H ₁₈ O	9	5.2217
C ₂₀ H ₂₄ O	9	1.6386

Table SI 6.3 The data summary of the heptane/toluene fraction of the most abundant HC, O₁ and N₁ classes in crab biochar extracted by solvent extrography. Values shaded represent the protonated HC (blue), radical HC (blue), protonated N₁ species (pink), radical N₁ species (purple), protonated O₁ species (green), and radical O₁ species (orange).

Formula	DBE	Abundance
C ₁₉ H ₁₄	13	57.7668
C ₁₇ H ₁₄	11	43.2257
C ₁₇ H ₁₈	9	21.4507
C ₁₇ H ₁₆	10	11.0806
C ₁₇ H ₂₀	8	10.3114
C ₁₈ H ₁₈	10	8.32
C ₁₈ H ₁₆	11	7.6031
C ₁₈ H ₁₄	12	7.3366
C ₁₈ H ₁₂	13	6.7752
C ₁₇ H ₁₈	9	19.3347
C ₁₈ H ₁₂	13	12.5574
C ₁₉ H ₁₄	13	7.7344
C ₃₀ H ₅₀	6	7.5333
C ₃₀ H ₄₈	7	6.0016
C ₃₀ H ₄₇ N	8	103.7248
C ₂₁ H ₂₉ N	8	19.6579
C ₂₅ H ₃₅ N	9	17.8742
C ₂₄ H ₃₃ N	9	15.496
C ₃₁ H ₄₉ N	8	13.9898
C ₂₆ H ₃₇ N	9	10.3237

Formula	DBE	Abundance
C ₃₀ H ₄₇ N	8	87.0181
C ₃₁ H ₄₉ N	8	13.0048
C ₁₇ H ₂₀ O	8	31.2722
C ₁₇ H ₁₈ O	9	30.2829
C ₁₆ H ₁₈ O	8	19.3104
C ₁₈ H ₁₈ O	10	17.9701
C ₁₇ H ₁₆ O	10	15.8751
C ₁₈ H ₂₀ O	9	10.621
C ₁₆ H ₁₆ O	9	7.9977
C ₂₀ H ₂₂ O	10	7.7787
C ₁₇ H ₁₄ O	11	7.0118
C ₁₉ H ₂₆ O	7	6.9434
C ₁₇ H ₂₀ O	8	21.0599
C ₁₇ H ₁₈ O	9	9.7379
C ₁₇ H ₁₆ O	10	4.7814
C ₂₀ H ₂₂ O	10	3.1157
C ₂₀ H ₂₄ O	9	2.7579
C ₁₆ H ₁₄ O	10	2.617
C ₁₆ H ₁₈ O	8	2.1703
C ₁₉ H ₁₈ O	11	1.8236
C ₂₉ H ₅₀ O	5	1.7799

Table SI 6.4 The data summary of the Tol/THF/MeOH fractions of the most abundant HC, O₁ and N₁ classes in crab biochar extracted by solvent extrography. Values shaded represent the protonated HC (blue), radical HC (blue), protonated N₁ species (pink), radical N₁ species (purple), protonated O₁ species (green), and radical O₁ species (orange).

Formula	DBE	Abundance
C ₁₇ H ₁₄	11	9.1356
C ₁₉ H ₁₄	13	4.2076
C ₁₈ H ₂₀	9	3.719
C ₁₇ H ₂₀	8	3.5668
C ₂₁ H ₂₀	12	3.3656
C ₁₇ H ₁₈	9	3.3113
C ₁₈ H ₁₆	11	3.3102
C ₁₈ H ₂₂	8	2.6197
C ₂₀ H ₂₀	11	2.2253
C ₁₆ H ₁₈	8	2.1859
C ₁₈ H ₂₂ O	8	10.4449
C ₂₁ H ₁₆ O	14	8.404
C ₁₇ H ₂₀ O	8	6.7356
C ₁₈ H ₁₈ O	10	5.9071
C ₁₈ H ₂₄ O	7	5.7582
C ₁₇ H ₁₈ O	9	5.3526
C ₂₀ H ₂₀ O	11	4.8497
C ₂₀ H ₂₂ O	10	4.638
C ₁₆ H ₁₈ O	8	4.5587

SI 7. Data summaries of solvent extracts from kelp biochar.

Table SI 7.1 The data summary of the whole fraction based on the highest relative abundance of HC, O₁ and N₁ classes in kelp biochar extracted by solvent extrography. Values shaded represent the protonated HC (blue), radical HC (blue), protonated N₁ species (pink), radical N₁ species (purple), protonated O₁ species (green), and radical O₁ species (orange).

Chemical Formula	DBE	Relative Abundance
C ₁₉ H ₁₄	13	32.2608
C ₁₈ H ₁₂	13	6.7024
C ₁₈ H ₁₄	12	5.9747
C ₁₉ H ₁₆	12	5.1005
C ₁₈ H ₁₆	11	5.1004
C ₂₀ H ₁₆	13	3.7794
C ₁₉ H ₁₈	11	3.4211
C ₂₀ H ₁₈	12	3.4211
C ₁₈ H ₁₈	10	3.675
C ₁₉ H ₂₀	14	3.1447
C ₁₈ H ₁₂	13	7.2897
C ₁₉ H ₁₄	13	4.49
C ₃₀ H ₅₀	6	3.5075
C ₁₈ H ₁₄	12	2.7273
C ₂₀ H ₁₈	12	2.7271
C ₁₉ H ₁₆	12	2.6692
C ₂₀ H ₁₆	13	2.1787
C ₂₁ H ₂₀	12	1.5832

Chemical Formula	DBE	Relative Abundance
C ₁₇ H ₁₈	9	1.4638
C ₁₉ H ₁₈	11	1.4476
C ₁₉ H ₁₇ N	12	2.8543
C ₁₇ H ₁₃ N	12	2.5827
C ₁₈ H ₁₉ N	10	2.5567
C ₁₈ H ₁₅ N	12	2.5096
C ₁₈ H ₂₁ N	9	2.3478
C ₁₇ H ₁₅ N	11	2.285
C ₂₀ H ₂₇ N	8	2.2794
C ₁₈ H ₁₇ N	11	2.2712
C ₂₀ H ₁₉ N	12	2.2606
C ₁₇ H ₁₇ N	10	2.0879
C ₁₉ H ₁₇ N	12	1.348
C ₁₈ H ₁₅ N	12	1.2337
C ₂₀ H ₁₉ N	12	1.0246
C ₁₇ H ₁₃ N	12	0.9264
C ₂₀ H ₁₇ N	13	0.8594
C ₁₈ H ₂₁ N	9	0.8361
C ₁₈ H ₁₉ N	10	0.777
C ₂₂ H ₂₁ N	13	0.7331
C ₁₉ H ₁₅ N	13	0.724
C ₁₆ H ₁₈ O	8	10.0761
C ₁₈ H ₁₆ O	11	9.3206
C ₁₇ H ₂₀ O	8	9.068

Chemical Formula	DBE	Relative Abundance
C ₁₇ H ₁₈ O	9	8.3344
C ₁₈ H ₁₈ O	10	8.0462
C ₁₇ H ₁₆ O	10	7.0125
C ₁₇ H ₁₄ O	11	5.7573
C ₁₉ H ₁₆ O	12	5.6987
C ₁₉ H ₁₈ O	11	5.2845
C ₁₇ H ₂₀ O	8	2.6529
C ₁₈ H ₁₆ O	11	2.1685
C ₁₈ H ₁₈ O	10	2.0186
C ₂₆ H ₂₄ O	15	1.8987
C ₁₇ H ₁₈ O	9	1.8331
C ₂₅ H ₂₂ O	15	1.786
C ₂₆ H ₂₂ O	16	1.7786
C ₁₉ H ₁₆ O	12	1.761
C ₁₉ H ₁₈ O	11	1.7483

Table SI 7.2 The data summary of the acetone fraction of the most abundant HC, O₁ and N₁ classes in kelp biochar was extracted by solvent extrography. Values shaded represent the protonated HC (blue), radical HC (blue), protonated N₁ species (pink), radical N₁ species (purple), protonated O₁ species (green), and radical O₁ species (Orange).

Chemical Formula	DBE	Relative Abundance
C ₁₇ H ₁₄	11	79.3431
C ₁₉ H ₁₄	13	52.4048
C ₁₇ H ₁₈	9	48.258
C ₁₇ H ₁₆	10	20.1312
C ₂₁ H ₁₈	13	17.6187

Chemical Formula	DBE	Relative Abundance
C ₁₆ H ₁₄	10	16.8902
C ₁₈ H ₁₆	11	15.9654
C ₁₈ H ₁₂	13	15.3275
C ₁₈ H ₁₄	12	14.3475
C ₂₀ H ₁₆	13	13.9358
C ₁₇ H ₁₂	12	12.4455
C ₁₈ H ₁₂	13	15.2144
C ₁₆ H ₁₀	12	13.0802
C ₁₆ H ₁₂	11	11.0301
C ₁₇ H ₁₈	9	9.0193
C ₂₀ H ₁₈	12	7.8859
C ₂₁ H ₂₀	12	7.7545
C ₁₉ H ₁₄	13	7.572
C ₁₈ H ₁₄	12	6.7726
C ₂₀ H ₁₆	13	6.6099
C ₂₃ H ₁₈	15	6.3225
C ₁₉ H ₁₇ N	12	46.685
C ₂₀ H ₁₉ N	12	45.1906
C ₂₁ H ₂₁ N	12	38.3812
C ₁₈ H ₂₁ N	9	34.3071
C ₁₉ H ₂₃ N	9	32.9155
C ₂₁ H ₁₉ N	13	31.0876
C ₂₂ H ₂₁ N	13	30.9591

Chemical Formula	DBE	Relative Abundance
C ₁₉ H ₂₁ N	10	30.4766
C ₁₉ H ₁₉ N	11	28.9291
C ₂₀ H ₁₇ N	13	2.5386
C ₁₇ H ₂₀ O	8	100.7995
C ₁₇ H ₁₈ O	9	54.7816
C ₂₀ H ₁₈ O	12	27.4767
C ₁₈ H ₁₈ O	10	26.5489
C ₂₁ H ₂₀ O	12	26.1731
C ₁₇ H ₁₆ O	10	26.0938
C ₁₇ H ₂₀ O	8	9.2723

Table SI 7.3 The data summary of the Hept/Tol fraction of the most abundant HC, O₁ and N₁ classes in kelp biochar was extracted by solvent extrography. Values shaded represent the protonated HC (blue), radical HC (blue), protonated N₁ species (pink), radical N₁ species (purple), protonated O₁ species (green), and radical O₁ species (orange).

Chemical Formula	DBE	Relative Abundance
C ₁₉ H ₁₄	13	103.4989
C ₁₇ H ₁₄	11	65.3818
C ₁₈ H ₁₂	13	15.2357
C ₁₇ H ₁₈	9	14.6527
C ₁₈ H ₁₄	12	14.6299
C ₁₈ H ₁₆	11	13.3092
C ₁₉ H ₁₆	12	11.5705
C ₁₇ H ₁₆	10	9.7553
C ₁₉ H ₁₂	14	9.2984

Chemical Formula	DBE	Relative Abundance
C ₁₆ H ₁₄	10	7.649
C ₁₇ H ₁₈	9	27.8929
C ₁₈ H ₁₂	13	21.6312
C ₃₀ H ₅₀	6	15.9097
C ₁₉ H ₁₄	13	12.8978
C ₃₀ H ₄₇ N	8	55.7096
C ₂₅ H ₃₅ N	9	12.7365
C ₂₁ H ₂₉ N	8	11.7221
C ₂₄ H ₃₃ N	9	11.6921
C ₃₀ H ₄₇ N	8	48.5353
C ₃₇ H ₅₃ N	12	7.0725
C ₃₁ H ₄₉ N	8	6.8621
C ₁₆ H ₁₈ O	8	44.5183
C ₁₇ H ₁₈ O	9	23.4939
C ₁₇ H ₂₀ O	8	22.5721
C ₁₈ H ₁₈ O	10	15.132
C ₁₆ H ₁₆ O	9	10.5677
C ₁₇ H ₂₀ O	8	32.3531
C ₁₇ H ₁₈ O	9	8.0268
C ₁₉ H ₁₈ O	11	4.429
C ₁₆ H ₁₈ O	8	4.2241
C ₂₁ H ₂₀ O	12	3.9261

Table SI 7.4 The data summary of the Tol/THF/MeOH fractions of the most abundant HC, O₁ and N₁ classes in kelp biochar extracted by solvent extrography. Values shaded represent the protonated HC (blue), radical HC (blue), protonated N₁ species (pink), radical N₁ species (purple), protonated O₁ species (green), and radical O₁ species (orange).

Chemical Formula	DBE	Relative Abundance
C ₁₇ H ₁₄	11	26.5042
C ₁₉ H ₁₄	13	14.1705
C ₂₁ H ₂₀	12	13.0558
C ₁₈ H ₁₆	11	10.9711
C ₂₂ H ₂₂	12	9.6728
C ₂₀ H ₂₀	11	7.7671
C ₁₆ H ₁₂	11	3.5456
C ₁₆ H ₁₀	12	3.4757
C ₁₇ H ₁₄	11	1.5342
C ₁₈ H ₂₂ O	8	34.9323
C ₁₈ H ₁₈ O	10	27.1267
C ₂₀ H ₂₀ O	11	19.259
C ₂₁ H ₁₈ O	13	16.684
C ₁₇ H ₂₀ O	8	16.2678
C ₁₈ H ₂₄ O	7	16.0514
C ₁₄ H ₁₂ O	9	13.9613
C ₁₉ H ₂₀ O	10	15.4731
C ₂₁ H ₂₀ O	12	1.0482
C ₁₈ H ₁₈ O	10	0.9712
C ₁₈ H ₁₆ O	11	0.9016

Chemical Formula	DBE	Relative Abundance
$C_{21}H_{16}O$	14	0.8674